TECHNISCHE UNIVERSITÄT MÜNCHEN
Lehrstuhl für Regelungstechnik

Model Order Reduction of Moving Nonlinear Electromagnetic Devices

Mohammad Nassar Albunni

Vollständiger Abdruck der von der Fakultät für Maschinenwesen
der Technischen Universität München zur Erlangung
des akademischen Grades eines

Doktor-Ingenieurs

genehmigten Dissertation.

Vorsitzender: Univ.-Prof. Dr.-Ing. Florian Holzapfel
Prüfer der Dissertation:

1. Univ.-Prof. Dr.-Ing. habil. Boris Lohmann
2. Univ.-Prof. Dr. techn. Romanus Dyczij-Edlinger,
   Universität des Saarlandes

Die Dissertation wurde am 01.07.2010 bei der Technischen Universität München eingereicht und durch die Fakultät für Maschinenwesen am 20.10.2010 angenommen.

ABSTRACT

This dissertation delivers a contribution to the field of order reduction of large-scale nonlinear models of electromagnetic devices. In particular, it enables applying model order reduction techniques to an important class of electromagnetic devices that contain *moving components* and materials with *nonlinear magnetic properties*. Such devices include among others rotating electrical machines, electromagnetic valves, electromagnetic solenoids, and electromechanical relays.

The presented methods exploits the *trajectory piecewise linear* (TPWL) approach in approximating the nonlinear dependency of materials properties on the applied magnetic field. Additionally, the model nonlinearity that is caused by the movement of the device components is handled using a novel approach that updates the electromagnetic (EM) field model permanently according to the new components positions.

The order of the large-scale electromagnetic field model is reduced by approximating the original electromagnetic field distribution by a linear combination of few *virtual field distributions* that are found using the *proper orthogonal decomposition* (POD) approach.

The challenge of selecting the number and the position of the linearization points in the TPWL model is tackled using a new approach that considers the change in the magnetic properties of the device materials among all the simulated state-vectors.

The new presented methods are extended to enable generating *parametric reduced order models* of moving nonlinear EM devices. Such models enable a fast and accurate prediction of the behavior of the EM device and its variations that result from changing the values of its design parameters. Additionally, several algorithms for generating an optimal reduction subspace of the parametric model are presented and compared.

Finally, an approach for overcoming the challenge of generating reduced order models of EM devices while considering the strong influence of their power electronics driving circuits is introduced and applied to the example of a rotating electrical machine coupled to a power electronics driving circuit.

The new methods presented in this work are validated by applying them on the examples of three industrial devices. An electrical transformer, an electromagnetic valve, and a rotating electrical machine.

DEDICATION

To my parents, my wife, and my daughter.

ACKNOWLEDGMENTS

My deepest gratitude to my advisor Prof. Boris Lohmann for his support, guidance, and encouragement throughout all the stages of my Ph.D. Studies.

I am very grateful to my second examiner Prof. Romanus Dyczij-Edlinger for his efforts in examining my work and for the important comments that helped me to improve this dissertation.

I would like to thank Dr. Volker Rischmueller for offering me the chance to work on this exciting research field, and Dr. Oliver Rain for the valuable discussions in the field of numerical modeling of electromagnetic devices.

Very special thanks to Dr. Thomas Fritzsche for the plenty of hours that we have spent discussing the challenges and the solutions for applying model order reduction approaches in industrial research fields.

My special gratefulness to Dr. Rudy Eid, for his friendship, support, and for all the fruitful discussions that we had throughout my graduate studies.

My deepest thanks to my parents and sisters for their love and inspiration, and to my wife for her love, encouragement, and patience.

Finally, my thanks to my little daughter Laila for sacrificing her playing time in order to enable me to finalize this work.

Mohammad Nassar Albunni Stuttgart, June 2010

TABLE OF CONTENTS

LIST OF FIGURES

LIST OF TABLES

Notations

ε	electric permittivity
κ	electric conductivity
μ	magnetic permeability
ν	magnetic reluctivity
$d\nu$	derivative of the magnetic reluctivity with respect to $\|\vec{B}\|$
ρ	free electric charge densities
$\sigma_i(\mathbf{A})$	i_{th} singular value of the matrix $\mathbf{A}$
$\vec{A}$	spatially continuous magnetic vector potential
$\vec{B}$	spatially continuous magnetic induction field
$\vec{D}$	spatially continuous displacement current
$\vec{E}$	spatially continuous electric field
$\vec{H}$	spatially continuous magnetic field
$\vec{P}$	spatially continuous electric polarization
$\vec{M}$	spatially continuous magnetization field
$\vec{f}_{mag}$	spatially continuous electromagnetic force
f_{mag}	the surface integral of electromagnetic force on the surface of an object
$\vec{g}$	spatially continuous free electric current densities
$\vec{g}_s$	spatially continuous impressed current densities
$\vec{v}$	velocity vector of an object
$\mathbb{R}$	set of real numbers
$\mathbb{R}^n$	the set of all vectors of dimension n with real entries
$\mathbb{R}^{n\times m}$	the set of all $n \times m$ matrices with real entries
$\mathbf{a}$	spatially discretized magnetic vector potential
$\mathbf{b}$	vector describing the distribution of current density in an excitation coil
$\mathbf{C}$	damping matrix
$\mathbf{f}(\mathbf{a})$	vector function representing the nonlinear stiffness term

	in the spatially discretized electromagnetic field model
$\mathbf{G}(\mathbf{x})$	position dependent boundary matrix
$\mathbf{H}(\mathbf{x})$	position dependent boundary matrix
$\mathbf{K}(\mathbf{a})$	field dependent stiffness matrix
$\mathbf{K}^{\mathbf{BEM}}(\mathbf{x})$	position dependent boundary matrix
$\mathbf{L}_i$	Jacobian matrix of the function $\mathbf{f}(\mathbf{a})$ evaluated at the expansion point $\mathbf{a}_i$
$\mathbf{p}$	vector design parameters of an EM device
$\mathbf{p}_{pm}$	vector describing the contribution of permanent magnets to the electromagnetic field excitation
$\mathbf{q}$	Neumann data of the exterior boundary problem
$\mathbf{r_s}$	contribution of the impressed current density
$\mathbf{r_{s\Gamma}}$	contribution of the external EM field sources
$\mathbf{R}(\mathbf{x})$	position dependent matrices for calculating EM force
$\mathbf{S}(\mathbf{x})$	position dependent matrices for calculating EM torque
$\mathbf{T}$	constant boundary matrix
$\mathbf{V}$,$\mathbf{W}$	projection matrices for the reduction in state space
$\mathbf{x}$	vector describing the position of the center of gravity of a device component

Abbreviations

BEM	boundary elements method
BEM-FEM	coupled boundary elements finite elements method
CPU	central processing unit
DAE	differential algebraic equations
EM	electromagnetic
FEM	finite elements method
LTI	linear time invariant
MIMO	multi input multi output system

MOR	model order reduction
ODE	ordinary differential equations
POD	proper orthogonal decomposition
POF	Pareto optimal front
PROM	parametric reduced order model
ROM	reduced order model
SISO	single input single output system
TBR	truncated balanced realization
TPWL	trajectory piecewise linear
TPWP	trajectory piecewise polynomial
vs.	versus

Chapter 1

INTRODUCTION

The design and development of electromechanical devices based on their computer simulation models have been gaining an increasing interest in the last two decades. This is due to the advantages of this trend in reducing the device development time, and in decreasing the number of expensive hardware prototypes in comparison to conventional design methods. However, the aforementioned advantages can be only exploited when the simulation models are able to predict of the behavior of the modeled devices accurately.

An important class of simulation models is based on applying the spatial discretization methods to the physical laws that govern the behavior of the modeled devices. Such models are commonly able to meet the requirements on the modeling accuracy. Such models include among others the models generated using the finite elements method FEM, boundary elements method BEM, finite difference method FDM, finite volume method, etc. The common factor among all previous methods is that the spatial discretization of the governing physical laws often produces a large system of linear or nonlinear equations. Therefore, performing a simulation using one of the aforementioned models can be very expensive in the sense of computational effort.

Nevertheless, the high accuracy of the aforementioned simulation models has motivated the developers to consider the design of sophisticated technical systems. Such systems might contain several interacting devices. Therefore, the simulation of those systems requires coupling several devices' models in a so called *system simulation*. However, the requirements for simulating a system of coupled high dimensional models can rapidly

go beyond the available time and computational resources.
Model order reduction techniques present a solution for the complexity-accuracy dilemma. This is due to their ability to generate compact simulation models - having low number of equations - starting from the original high complexity ones. The accuracy of the generated models can be guaranteed in some segments of the frequency domain or around several trajectories in the time domain.

1.1 Thesis Contribution

Electromagnetism is one of the fields where model order reduction techniques have been receiving a growing interest. Their ability to generate compact simulation models of electromagnetic devices starting from their spatially discretized linear models has been demonstrated in several works [14], [67], [68], [60], [22]. Less focus has been put on applying model order reduction techniques to the *nonlinear models* of electromagnetic devices. A major contribution in this field is the work in [51], in which the authors applied the trajectory piecewise linear models approach TPWL [54] to generate a compact approximation model of a magnetic device with nonlinear materials properties. However, a crucial issue that has not been addressed in most of the previous works is to consider the movement of the modeled device components in the generation of the reduced order models. This can be traced back to the significant changes that occur in the electromagnetic field model upon the movement of the modeled device components. In this work, we propose a new approach that enables considering *components movement* and the *nonlinear properties of magnetic materials* in the reduced order models of electromagnetic devices. The approach exploits model order reduction techniques to approximate the large scale nonlinear models of the electromagnetic field by reduced order ones having a much lower number of equations. The reduced order EM field models are weakly coupled to the mechanical equations in order to simulate the movement of the device components. The position information that are obtained from solving the mechanical equations are used to update the position dependent terms in the reduced order EM field model.
The contributions of this dissertation can be summarized as follows:

- A new approach for generating reduced order models for electromagnetic devices contain moving components and materials with nonlinear magnetic properties is introduced.

- An algorithm for selecting the number and the position of the linearization points in the trajectory piecewise linear TPWL model is presented. The proposed algorithm is based on observing the change in the materials properties during the simulation.

- An approach for generating parametric reduced order models of moving nonlinear electromagnetic devices is presented.

- An approach for coupling the reduced order models of moving nonlinear electromagnetic devices to external power electronics driving circuits is presented.

- An approach for exploiting the generated reduced order models of moving nonlinear electromagnetic devices in performing a multiobjective design optimization of the underlying device is introduced.

The presented results in this work open the way for applying model order reduction techniques to the compact modeling of an important class of electromagnetic devices. Rotating electrical machines, electromagnetic valves, and electromagnetic relays are few examples on the industrial devices that can be addressed using the new presented results.

1.2 Dissertation Overview

In chapter 2, a comprehensive overview on the numerical modeling of electromagnetic devices is presented. The weak electromechanical coupling approach that is exploited for modeling the components movement is reviewed. In addition, the nonlinear behavior of some magnetic materials is discussed and supported with examples. The chapter is continued by deriving the high order nonlinear model of electromagnetic field, and illustrating its common input and output signals.

The third chapter revisits order reduction methods for both linear and nonlinear dynamic systems. The trajectory piecewise linear TPWL approach [53] and the proper orthogonal decomposition POD approach are reviewed in more details, since they represent the base of the approaches and algorithms that are presented in this work. The advantages of using the two previous approaches in the model order reduction of of electromagnetic devices are listed.

In chapter 4, we address the issue of reducing the order of linear models of electromagnetic devices using Krylov subspace approaches. A special focus is given to the generation of reduced order models that are able to reproduce the input-output behavior of both the current driven and the voltage driven electromagnetic field models. The two latter models are required for simulating electromagnetic devices in which the excitation signal type is varied from voltage to current and vice versa during the device operation.

A novel approach for generating reduced order models of electromagnetic devices that contain moving components and materials with nonlinear magnetic properties is presented in chapter 5. A new algorithm for selecting the number and the position of the linearization points in the trajectory piecewise linear TPWL model is introduced. Additionally, the generated reduced order models are exploited in performing a multi-objective design optimization of an industrial electromagnetic device.

In chapter 6, a method for generating *parametric reduced order models* of moving nonlinear electromagnetic devices is presented. Moreover, three different algorithms for generating the reduction subspace of the parametric models are presented, and their performance is compared by applying them to a numerical example.

The seventh chapter addresses the challenge of considering the strong influence of the driving power electronics circuits on the behavior of the modeled devices. An approach for generating fast and compact reduced order models of electromagnetic devices considering the coupling to the power electronics driving circuits is presented. The aforementioned approach is applied to generate a reduced order model of a rotating electrical machine coupled to a three phase rectifier.

Finally, the dissertation is concluded with a summary of the results and an outlook on the possible future works.

Chapter 2

NUMERICAL MODELING OF ELECTROMAGNETIC DEVICES

2.1 Modeling of Electromechanical Systems

The dynamic analysis of electromechanical systems including motion requires the solution of the coupled electromagnetic-mechanical equations. However, in a large class of industrial applications, the state variables of the mechanical equations are much slower than those of the electromagnetic field equations. Thus, if the simulation time step is chosen to be small enough, then the two systems of equations can be solved alternatingly in the so called *weak electromechanical coupling* approach [30, 33, 34] which is graphically illustrated in Fig. (2.1) .

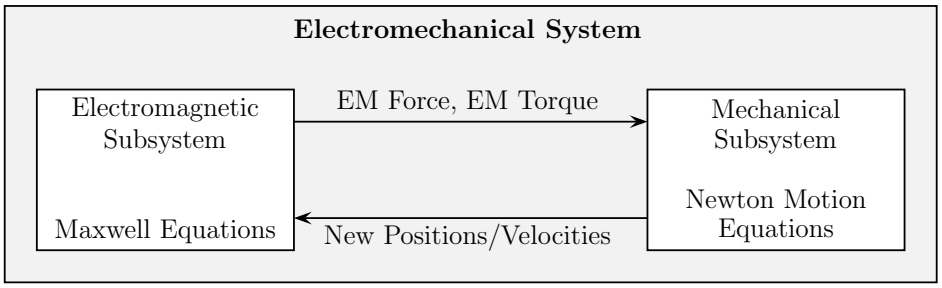

Figure 2.1: Decoupling the electromechanical system model into two interacting electromagnetic and mechanical subsystems.

The main steps of the weak electromagnetic coupling scheme are briefly reviewed in the following three paragraphs.

2.1.1 Solving the electromagnetic field equations

All modeling approaches of electromagnetic fields can be traced back to the Maxwell's equations, which are written in their differential form as:

$$\mathrm{rot}\vec{H} = \vec{g} + \frac{\partial \vec{D}}{\partial t} \tag{2.1}$$

$$\mathrm{rot}\vec{E} = -\frac{\partial \vec{B}}{\partial t} \tag{2.2}$$

$$\mathrm{div}\vec{B} = 0 \tag{2.3}$$

$$\mathrm{div}\vec{D} = \rho \tag{2.4}$$

where $\vec{B}$ is the magnetic induction field, $\vec{H}$ is the magnetic field, $\vec{E}$ is the electric field, $\vec{D}$ is the displacement current, $\vec{g}$ is the free electric current densities, and ρ is the free electric charge densities.
The four Maxwell equations are commonly used together with the following relations in the modeled materials:

$$\vec{D} = \varepsilon_0 \vec{E} + \vec{P} \tag{2.5}$$

$$\vec{B} = \mu_0 \left(\vec{H} + \vec{M} \right) \tag{2.6}$$

$$\vec{g} = \vec{g}_s + \kappa \left(\vec{E} + \vec{v} \times \vec{B} \right) \tag{2.7}$$

where $\vec{P}$ is the electric polarization, $\vec{M}$ is the magnetization, $\vec{g}_s$ is the impressed current densities, κ is the specific electric conductivity, ε is the permittivity, and $\vec{v}$ is the velocity vector of the moving bodies within the magnetic field $\vec{B}$.
In the class of electromagnetic devices that are considered in this work, most of the device energy is carried by the magnetic field. Therefore, a common simplification of Maxwell's equations in this case is the magneto(quasi)static formulation, in which the displacement current, $\vec{D}$ and its time derivative $\frac{\partial \vec{D}}{\partial t}$ are neglected. This can be formally realized by setting $\varepsilon_0 \to 0$, $\vec{P} = 0$ in the equation (2.5), and setting the density of free space charges $\rho = 0$.
The derivation of a spatially discretized model of electromagnetic field based on the

equations (2.1)-(2.7) can be found in several references [12, 20, 33, 55]. In this paragraph, the detailed derivation will be skipped since it is out of the scope of this work. However, it can be briefly said that in low frequency limits, the spatial discretization of the transient formulations of electromagnetic field using one of the finite discretization methods (e.g. the finite elements FE, finite difference FD, or the coupled finite element boundary elements BEM-FEM) commonly produces a large scale systems of nonlinear ordinary differential equations or differential algebraic equations [15]. By applying one of the time integration schemes, the values of the EM field variables can be found and the corresponding magnetic forces and torques can be calculated.

2.1.2 Solving the mechanical equations

Based on the calculated values of magnetic forces and torques, the mechanical equations can be solved in order to update the device components positions. If the movement of rigid bodies is considered, the movement of an object can be described as a translation of its center of gravity with respect to a reference coordinate frame, and a rotation of its own coordinate frame with respect to the reference frame. Therefore, a maximum number of six equations per moving object are required for describing its movement in 3D space.
The translational movement can be modeled using Newton's motion equations:

$$\mathbf{M}\ddot{\mathbf{x}} + \mathbf{D}\dot{\mathbf{x}} + \mathbf{K}_m\mathbf{x} = \mathbf{f}_{\text{mag}} \tag{2.8}$$

where $\mathbf{M}, \mathbf{D}, \mathbf{K}_m$ are respectively the mass, damping, and the stiffness matrices of the mechanical equations, and $\mathbf{x}$ is the position vector of the device components.
Similarly, the rotational movement of the device components can be modeled using Euler's equations, in which the input signals are the electromagnetic torques that have been calculated from the solution of the EM field equations.

2.1.3 Updating the electromagnetic field equations according to the new components positions

When one or more of the device components move, the electromagnetic field model has to be adapted according to the new relative positions of the device components. Several strategies can be exploited to perform this adaptation. In the remeshing approach [36], a new discretization mesh with a possibly new number of nodes has to be generated whenever the device components change their positions. Whereas in the sliding mesh approach [13], which is particularly popular for handling rotational movement, the unknown variables that are located on the interfaces between the moving objects are permutated upon components rotation. Finally, in the coupled boundary elements finite elements method BEM-FEM, a group of boundary matrices have to be recalculated whenever the device components change their positions. After updating the electromagnetic field equations, a new simulation cycle can be started according to the aforementioned three steps.

It is worth mentioning that solving the equations of the large-scale nonlinear model of EM field is the most time and computer resources consuming step in the weak electromagnetic coupling scheme. Therefore, a significant speed up in the simulation time can be achieved when approximating the large-scale electromagnetic field model by a compact one having much lower number of equations.

Motivated by this fact, this research work exploits model order reduction techniques in building low order electromagnetic models based on their original large-scale spatially discretized ones. The coupled BEM-FEM is chosen to generate the full order models of EM field. This is due to its advantages in keeping both the number and the ordering of the electromagnetic field variables constant during the components movement, as it will be shown later on in this chapter.

However, before moving to the modeling details, it is helpful to present a brief overview on the definition of linear and nonlinear electromagnetic systems.

2.2 Linear Electromagnetic Systems

In this work, an electromagnetic system is referred as linear when the relation between the magnetic field strength $\vec{H}$ and the magnetic flux density $\vec{B}$ is linear in all the materials that are contained in the modeled device:

$$\vec{H} = \nu \vec{B} \tag{2.9}$$

This linearity condition imposes that the value of the magnetic reluctivity ν is material-wise constant and do not depend on the value of the applied magnetic field, as it is shown in Fig. 2.2.(a).

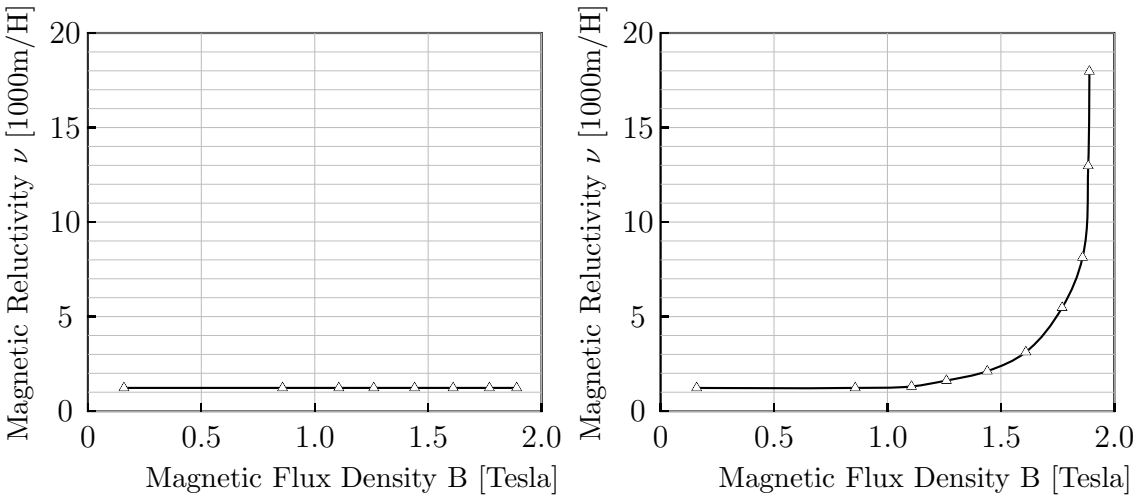

(a) The magnetic reluctivity of a chosen linear magnetic material

(b) The magnetic reluctivity of a chosen nonlinear magnetic materials

Figure 2.2: A figure illustrating the magnetic reluctivity of chosen linear and nonlinear nonlinear magnetic materials

2.3 Nonlinear Electromagnetic Systems

In a large class of materials that are used for manufacturing electromagnetic devices, the magnetic reluctivity ν is not material-wise constant, instead its values in the same

material is dependant on the amplitude of the applied magnetic filed at the evaluation points. Consequently, the relation between the magnetic field strength vector $\vec{H}$ and the magnetic flux density vector $\vec{B}$ becomes nonlinear:

$$\vec{H} = \nu\big(\|\vec{B}\|\big)\vec{B} \tag{2.10}$$

The dependency of the magnetic reluctivity ν on the applied magnetic field is commonly extracted from measurements, an example of such a dependency is shown in Fig.2.2.(b). In this chapter and throughout the whole work, we denote electromagnetic devices that contain materials with nonlinear magnetic properties as nonlinear electromagnetic systems.

2.4 The Electromagnetic Field Model Using the BEM-FEM Method

When applying the BEM-FEM method to the spatial discretization of Maxwell's equations in 3D space, the model parts containing electrically conducting materials or magnetic materials are discretized using finite elements. Whereas, air regions inside the device geometry or surrounding it are not discretized with finite elements, and the behavior of electromagnetic field in those regions is modeled using boundary integral equations.

Theoretically, the spatial discretization can be carried out using a nodal-elements-based approach [35], [56] or an edge-elements-based one [52]. The latter approach is based on treating the variables of the EM field as differential forms [12], which has proven to produce the right solution of Maxwell problems [16]. However, the detailed comparison between the two approaches is out of the scope of this work.

The modeling scheme reviewed here starts from the potential based magneto(quasi)static formulation of Maxwell equations, which assumes that the magnetic induction field is equal to the rotation of the magnetic vector potential field:

$$\vec{B} = \operatorname{rot}\vec{A} \tag{2.11}$$

The advantage of this assumption is that it guarantees fulfilling Maxwell's equation (2.3). Now, the remaining Maxwell's equations can be reformulated considering the simplification assumptions in paragraph 2.1.1 as:

$$\mathrm{rot}\,\nu\,\mathrm{rot}\vec{A} = \vec{g} \tag{2.12}$$

where:

$\vec{A}$ = magnetic vector potential
ν = magnetic reluctivity $\nu = \nu(\vec{A})$

In the previous paragraph, we have seen that the magnetic reluctivity ν in a large class of materials is dependant on the magnetic induction field $\vec{B}$. Therefore, the reluctivity ν becomes directly dependant on the magnetic vector potential $\vec{A}$ according to the equation (2.11). This dependency describes the magnetic saturation effects in materials, and it forces a nonlinearity in the final spatially discretized model equations:

$$\begin{bmatrix} \mathbf{C} & 0 \\ 0 & 0 \end{bmatrix} \frac{d}{dt} \begin{bmatrix} \mathbf{a}(t) \\ \mathbf{q}(t) \end{bmatrix} + \begin{bmatrix} \mathbf{K}(\mathbf{a}) & -\mathbf{T} \\ \mathbf{H}(\mathbf{x}) & \mathbf{G}(\mathbf{x}) \end{bmatrix} \begin{bmatrix} \mathbf{a}(t) \\ \mathbf{q}(t) \end{bmatrix} = \begin{bmatrix} \mathbf{r}(t) \\ \mathbf{r}_\gamma(t) \end{bmatrix} \tag{2.13}$$

where:

$\mathbf{a}$	= degrees of freedom of the magnetic vector potential
$\mathbf{q}$	= Neumann data of the exterior boundary problem
$\mathbf{C}$	= damping matrix (describes Eddy current losses).
$\mathbf{K}(\mathbf{a})$	= field dependent stiffness matrix
$\mathbf{T}$	= constant boundary matrix
$\mathbf{H}(\mathbf{x}), \mathbf{G}(\mathbf{x})$	= position dependent boundary matrices
$\mathbf{r}$	= contribution of the impressed current density
$\mathbf{r}_\gamma$	= contribution of the external sources of magnetic vector potential
$\mathbf{x}$	= the position vector of the device components

For the sake of clarity in the derivations in the coming paragraphs, the following nota-

tions will be made:

$$\hat{\mathbf{C}} = \begin{bmatrix} \mathbf{C} & 0 \\ 0 & 0 \end{bmatrix}, \hat{\mathbf{K}}(\mathbf{a}, \mathbf{x}) = \begin{bmatrix} \mathbf{K}(\mathbf{a}) & -\mathbf{T} \\ \mathbf{H}(\mathbf{x}) & \mathbf{G}(\mathbf{x}) \end{bmatrix}, \hat{\mathbf{a}}(t) = \begin{bmatrix} \mathbf{a}(t) \\ \mathbf{q}(t) \end{bmatrix}, \hat{\mathbf{r}}(t) = \begin{bmatrix} \mathbf{r}(t) \\ \mathbf{r}_\gamma(t) \end{bmatrix} \quad (2.14)$$

Consequently, the equation (2.13) can be written as:

$$\hat{\mathbf{C}} \frac{d}{dt} \hat{\mathbf{a}}(t) + \hat{\mathbf{K}}(\mathbf{a}, \mathbf{x}) \hat{\mathbf{a}}(t) = \hat{\mathbf{r}}(t) \quad (2.15)$$

2.5 Time Discretization Scheme

In general, the modeling of electromagnetic devices including Eddy currents often produces systems of *stiff* differential equations [25], which are known to have large difference in the dynamics of their fastest and and slowest state-variables. The time integration of stiff differential equation using explicit approaches requires selecting a very small simulation time steps, which increases the computational costs of the simulation. Therefore, it is recommendable to use implicit approaches for the time integration of stiff differential equations.

In the BEM-FEM modeling approach [33, 55], the implicit Backward-Euler method is used for the time integration of the equations system (2.15) as follows:

$$\hat{\mathbf{a}}_{t+\Delta t} = \hat{\mathbf{a}}_t + \Delta t \left. \frac{d\hat{\mathbf{a}}}{dt} \right|_{t+\Delta t} \quad (2.16)$$

$$\hat{\mathbf{C}} \hat{\mathbf{a}}_{t+\Delta t} = \hat{\mathbf{C}}\, \hat{\mathbf{a}}_t + \Delta t\, \hat{\mathbf{C}} \left. \frac{d\hat{\mathbf{a}}}{dt} \right|_{t+\Delta t}$$

$$\hat{\mathbf{C}} \hat{\mathbf{a}}_{t+\Delta t} = \hat{\mathbf{C}} \hat{\mathbf{a}}_t + \Delta t \Big[- \hat{\mathbf{K}} \left(\mathbf{a}_{t+\Delta t}, \mathbf{x}_{t+\Delta t} \right) \hat{\mathbf{a}}_{t+\Delta t} + \hat{\mathbf{r}}_{t+\Delta t} \Big]$$

$$\hat{\mathbf{a}}_{t+\Delta t} = \Big[\hat{\mathbf{C}} + \Delta t\, \hat{\mathbf{K}} \left(\mathbf{a}_{t+\Delta t}, \mathbf{x}_{t+\Delta t} \right) \Big]^{-1} \Big(\hat{\mathbf{C}} \hat{\mathbf{a}}_t + \Delta t\, \hat{\mathbf{r}}_{t+\Delta t} \Big) \quad (2.17)$$

It is clear that the nonlinear equations system (2.17) can not be solved directly due to the term $\hat{\mathbf{K}} \left(\mathbf{a}_{t+\Delta t}, \mathbf{x}_{t+\Delta t} \right)$ which depends on both the unknown solution vector $\hat{\mathbf{a}}_{t+\Delta t}$ and the unknown position vector $\mathbf{x}_{t+\Delta t}$. However, in the weak electromechanical coupling approach, the electromagnetic field equations are solved for a small enough simulation time step assuming that the device components did not move. Hence, the matrices $\mathbf{G}$

and $\mathbf{H}$ in (2.14)-(2.17) are determined based on the position vector $\mathbf{x}_t$, and are assumed to be known when solving the nonlinear equation (2.17). Therefore, the dependency of the matrix $\hat{\mathbf{K}}(\mathbf{a}, \mathbf{x})$ on the position vector $\mathbf{x}$ will be skipped from the notation in the next paragraph.

2.6 Solving the Nonlinear Equation System

One of the most efficient methods for solving large scale system of nonlinear equations is the Newton-Raphson method [50]. This method uses iteratively the gradient information of a function to find its minimum. In [33, 55], the Newton-Raphson method is exploited for solving the nonlinear equations system (2.17) by minimizing the residuals vector between its left and right hand side as follows:

$$\mathbf{e}\left(\hat{\mathbf{a}}_{t+\Delta t}\right) = \left[\hat{\mathbf{C}} + \Delta t\ \hat{\mathbf{K}}\left(\hat{\mathbf{a}}_{t+\Delta t}\right)\right] \hat{\mathbf{a}}_{t+\Delta t} - \left(\hat{\mathbf{C}}\hat{\mathbf{a}}_t + \Delta t\ \hat{\mathbf{r}}_{t+\Delta t}\right) \tag{2.18}$$

The optimization algorithm starts with an initial guess of the solution vector $\hat{\mathbf{a}}_{t+\Delta t}$, a common approach is to take the value of the previous time step. Then, it exploits iteratively the derivative of the error function (2.18) with respect to the solution vector $\mathbf{a}_{t+\Delta t}$ to find its minimum. The aforementioned derivative can be calculated using the product rule as:

$$\frac{d\mathbf{e}\left(\hat{\mathbf{a}}_{t+\Delta t}\right)}{d\hat{\mathbf{a}}_{t+\Delta t}} = \Delta t\ \frac{d}{d\hat{\mathbf{a}}}\hat{\mathbf{K}}(\hat{\mathbf{a}})\bigg|_{\hat{\mathbf{a}}_{t+\Delta t}} \hat{\mathbf{a}}_{t+\Delta t} + \left[\hat{\mathbf{C}} + \Delta t\ \hat{\mathbf{K}}\left(\hat{\mathbf{a}}_{t+\Delta t}\right)\right] \tag{2.19}$$

The first term in (2.19) can be calculated based on (2.14) as:

$$\frac{d}{d\hat{\mathbf{a}}}\hat{\mathbf{K}}(\hat{\mathbf{a}})\bigg|_{\hat{\mathbf{a}}_{t+\Delta t}} \hat{\mathbf{a}}_{t+\Delta t} = \begin{bmatrix} \mathbf{J}\left(\mathbf{a}_{t+\Delta t}\right) & 0 \\ 0 & 0 \end{bmatrix} \tag{2.20}$$

The matrix $\mathbf{J}(\mathbf{a})$ will be denoted in this work as the Jacobian matrix. Its value at a given solution vector $\mathbf{a}_i$ can be evaluated by:

$$\mathbf{J}(\mathbf{a}_i) = \frac{d}{d\mathbf{a}}\mathbf{K}(\mathbf{a})\bigg|_{\mathbf{a}_i} \mathbf{a}_i \tag{2.21}$$

Now, in each Newton-Raphson iteration, the solution vector $\hat{\mathbf{a}}_{t+\Delta t}$ is updated using the derivative information (2.19) as follows:

$$\hat{\mathbf{a}}_{t+\Delta t}^{new} = \hat{\mathbf{a}}_{t+\Delta t} - \eta \left[\frac{d\mathbf{e}\left(\hat{\mathbf{a}}_{t+\Delta t}\right)}{d\hat{\mathbf{a}}_{t+\Delta t}} \right]^{-1} \mathbf{e}\left(\hat{\mathbf{a}}_{t+\Delta t}\right) \tag{2.22}$$

where η is a relaxation parameter that is automatically adapted during the Newton-Raphson iterations in order to speed up the convergence. The iterative search is continued until the residuals vector $\mathbf{e}\left(\hat{\mathbf{a}}_{t+\Delta t}\right)$ becomes small enough so that the solution vector $\hat{\mathbf{a}}_{t+\Delta t}$ can be considered, within the user defined tolerance, as the solution of the backward Euler integration (2.17).

2.7 Calculating the nonlinear stiffness matrix $\mathbf{K}(\mathbf{a})$ and the Jacobian matrix $\mathbf{J}(\mathbf{a})$

Due to the importance of the nonlinear stiffness matrix $\mathbf{K}(\mathbf{a})$ and the Jacobian matrix $\mathbf{J}(\mathbf{a})$ for the model order reduction approaches that will be presented in this work, the procedure for their generation will be briefly summarized in the following steps:

1. The magnetic vector potential field $\vec{A}$ is generated based on the current state-vector $\mathbf{a}(t)$ and the spatial discretization form functions.

2. The magnetic flux density field $\vec{B}$ is calculated by applying the rotation operand to the magnetic vector potential field $\vec{B} = \mathrm{rot}\vec{A}$.

3. The magnetic reluctivity ν and its derivative $\dfrac{d\nu}{d\|B\|}$ are calculated at several points – called the Gaussian points – in each of the finite elements in the model. The calculation is done based on the magnitude of the magnetic flux density vector $\|\vec{B}\|$ at the corresponding evaluation point and on the measured reluctivity curve of the considered magnetic material (e.g. Fig. 2.2.(b)).

4. The calculated values of the magnetic reluctivity ν at all the evaluated Gaussian points are used together with the spatial discretization form functions in building

the nonlinear stiffness matrix $\mathbf{K}(\mathbf{a})$ at the state vector $\mathbf{a}$.

5. The calculated derivative $\frac{d\nu}{d\|B\|}$ at all the evaluated Gaussian points are used together with the spatial discretization form functions in building the derivative matrix $\mathbf{J}(\mathbf{a}) = \frac{d}{d\mathbf{a}}\mathbf{K}(\mathbf{a})\Big|_{\mathbf{a}}\mathbf{a}$.

The values of the magnetic reluctivity ν at all the Gaussian points can assembled in a vector $\boldsymbol{\nu} \in \mathbb{R}^{e_1}$, where e_1 is equal to the number e of finite discretization elements in the model multiplied by the number of Gaussian point pro element. In similar way, the derivative of the magnetic reluctivity $\frac{d\nu}{d\|B\|}$ at all the evaluated Gaussian points can be assembled in a vector $\boldsymbol{d\nu} \in \mathbb{R}^{e_1}$.
Now, knowing that discretization form functions that are used for the spatial discretization of the equation (2.12) remain constant during the simulation, then it can be easily concluded that the main difference among the matrices $\mathbf{K}(\mathbf{a})$ at different state-vectors can be traced back to the difference in their corresponding magnetic reluctivity vectors $\boldsymbol{\nu}$. Similarly, the difference among the $\mathbf{J}(\mathbf{a})$ matrices at different state-vectors can be related to the difference in their corresponding derivative vectors of the magnetic reluctivity $\boldsymbol{d\nu}$.

2.8 Excitation Signals

Electromagnetic fields can be generated for example by applying voltage or current signals to the terminals of electrical excitation coils in the considered EM devices. Alternatively, in certain class of electrical machines, the rotational movement of permanent magnets produces a time varying electromagnetic field.
Such excitation signals are modeled in the right hand side of the EM field model (2.13), in such a way that the vector $\mathbf{r}(t)$ models the contributions of all sources of current densities that are located in the regions discretized by the finite elements, whereas, the $\mathbf{r}_\gamma(t)$ models the contributions of the current density sources that are located outside the FEM regions (i.e. the regions that are not included in the spatial discretization).
In this work, we will consider without the loss of generality, that all sources of current

densities are modeled using finite elements and therefore are included in the vector $\mathbf{r}(t)$. Hence, the vector $\mathbf{r}\gamma(t)$ is considered to be equal to zero in all the derivations and examples that will be presented in this work.
In the following paragraphs, the modeling of the main types of excitation signals of electromagnetic devices is briefly reviewed.

2.8.1 Excitation using current driven coils

If we assume that the modeled EM device contains m different excitation coils that are connected to m different current sources $i_1(t), \ldots, i_m(t)$, then the excitation vector $\mathbf{r}(t)$ in the model (2.13) can be written as:

$$\mathbf{r}(t) = \overbrace{\begin{bmatrix} \mathbf{b}_1 & \ldots & \mathbf{b}_m \end{bmatrix}}^{\mathbf{B}} \begin{bmatrix} i_1(t) \\ \vdots \\ i_m(t) \end{bmatrix} \tag{2.23}$$

where each of the vectors $\mathbf{b}_i \in \mathbb{R}^n$ describes the distribution of current density in the ith excitation coil.

2.8.2 Excitation using voltage driven coils

If all the excitation coils of the modeled EM device are connected to voltage sources, then the value of the current $i_k(t)$ flowing in the kth excitation coil can be calculated based as [55]:

$$u_k(t) = \mathbf{b}_k^T \dot{\mathbf{a}}(t) + R_k i_k(t) \tag{2.24}$$

where R_k is the Ohmic resistance of the kth excitation coil, $u_k(t)$ is the voltage signal applied to its terminals, and the term $\mathbf{b}_k^T \dot{\mathbf{a}}(t)$ describes the eddy current losses in the kth excitation coil [55].
By calculating the excitation currents values from (2.24) and substituting them in (2.23)

we get:

$$\mathbf{r}(t) = -\mathbf{B}\tilde{\mathbf{B}}^T\dot{\mathbf{a}} + \tilde{\mathbf{B}} \begin{bmatrix} u_1(t) \\ \vdots \\ u_m(t) \end{bmatrix} \tag{2.25}$$

where $\tilde{\mathbf{B}} = \left[\frac{\mathbf{b}_1}{R_1}, \quad \dots \quad , \frac{\mathbf{b}_m}{R_m}\right]$. The term $-\mathbf{B}\tilde{\mathbf{B}}^T\dot{\mathbf{a}}$ can be moved to the left hand side of the model (2.13) which results in a modified damping matrix $\tilde{\mathbf{C}} = \left[\mathbf{C} + \mathbf{B}\tilde{\mathbf{B}}^T\right]$.

2.8.3 Excitation using permanent magnets

If we assume that the permanent magnets have a constant remanence value during the simulation, then the excitation vector $\mathbf{r}(t)$ becomes time independent and can be written as:

$$\mathbf{r}(t) = \mathbf{p}_{pm} \tag{2.26}$$

However, the movement of permanent magnets, which will be considered later in this work, causes the generation of time varying electromagnetic field.
It is worth mentioning that in many industrial applications, the modeled electromagnetic devices can have a combination of all the three aforementioned excitation types.

2.9 Calculating Electromagnetic Forces and Torques

In order to model the movement of the components of an EM device, the electromagnetic forces and torques that are acting on those components have to be calculated. A known method for calculating electromagnetic forces is to integrate Maxwell stress tensor [30], [35] over the surface s_k of an object k as follows:

$$\vec{f}_{\text{mag},k} = \int_{s_k} \left(\vec{f}_n + \vec{f}_t\right) ds \tag{2.27}$$

$$\vec{f}_n = \frac{1}{2}\left(\frac{B_n^2}{\mu_0} - \mu_0 H_t^2\right)\vec{n}, \qquad \vec{f}_t = B_n\vec{H}_t \tag{2.28}$$

where:

$\vec{n}$ = unit vector in the normal direction
μ_0 = magnetic permeability in vacuum

The tangential vector $\vec{H}_t$ and the normal induction B_n can be calculated from the solution vectors $\mathbf{a}$ of the electromagnetic field model (2.13). The spatially discretized form of the equations (2.27)-(2.28) can be formulated as:

$$f_{\mathrm{mag},k} = \begin{bmatrix} \mathbf{a}^T & \mathbf{q}^T \end{bmatrix} \overbrace{\begin{bmatrix} \tilde{\mathbf{R}}_{11} & \tilde{\mathbf{R}}_{12} \\ \tilde{\mathbf{R}}_{21} & \tilde{\mathbf{R}}_{22} \end{bmatrix}}^{\tilde{\mathbf{R}}^{(k)}} \begin{bmatrix} \mathbf{a} \\ \mathbf{q} \end{bmatrix} \tag{2.29}$$

where the index k denotes the k^{th} device object for which the EM force is calculated. The matrix $\tilde{\mathbf{R}}^{(k)}$ is constant and does depend on the components positions.
An alternative formulation of $f_{\mathrm{mag},k}$ can be found by solving the algebraic equations in (2.13) for $\mathbf{q}(t)$ considering that $\mathbf{r}_\gamma(t) = 0$ as has been discussed in the previous paragraph:

$$\mathbf{q}(t) = \mathbf{G}^{-1}(\mathbf{x})\mathbf{H}(\mathbf{x})\mathbf{a}(t) \tag{2.30}$$

Now the value $\mathbf{q}(t)$ cab be substituted in (2.29), after a simple rearrangement of the terms, it can be easily seen that the electromagnetic force can be written as:

$$f_{\mathrm{mag},k} = \mathbf{a}^T\mathbf{R}(\mathbf{x})\mathbf{a} \tag{2.31}$$

The matrix $\mathbf{R}$ depends now on the position $\mathbf{x}$ of the device components due to the dependency of the $\mathbf{G}$ and $\mathbf{H}$ matrices that are used in the solution (2.30) of $\mathbf{q}(t)$ on the position vector $\mathbf{x}$.
The magnetic torques can be derived in a very similar way, and the resulting spatially

discretized form can be written as:

$$\tau_{\mathrm{mag},k} = \begin{bmatrix} \mathbf{a}^T & \mathbf{q}^T \end{bmatrix} \overbrace{\begin{bmatrix} \tilde{\mathbf{S}}_{11} & \tilde{\mathbf{S}}_{12} \\ \tilde{\mathbf{S}}_{21} & \tilde{\mathbf{S}}_{22} \end{bmatrix}}^{\tilde{\mathbf{S}}^{(k)}} \begin{bmatrix} \mathbf{a} \\ \mathbf{q} \end{bmatrix} \tag{2.32}$$

and can be reformulated after eliminating the variables $\mathbf{q}(t)$ as:

$$\tau_{\mathrm{mag},k} = \mathbf{a}^T \mathbf{S}(\mathbf{x}) \mathbf{a} \tag{2.33}$$

Chapter 3

MODEL ORDER REDUCTION

In this chapter, a brief overview on the main approaches of model order reduction of both linear and nonlinear dynamic systems is presented. The trajectory piecewise linear TPWL approach together with the proper orthogonal decomposition POD approach are reviewed in more details since they represent the basis for the new methods and approaches that are presented in this work.

3.1 Model Order Reduction of Linear Systems

In the last two decades, several methods for reducing the order of linear time invariant (LTI) systems have been developed and applied in various application fields. In this brief overview, the main approaches in this field are revisited. For more detailed information, the reader is referred to [6].
For the sake of simplicity, we will consider the case of a high order LTI system (3.1) having a single input and a single output. However, the generalization to the case of multi-input multi-output systems is straight forward.

$$\begin{cases} \mathbf{E}\dot{\mathbf{x}} = \mathbf{A}\mathbf{x} + \mathbf{b}u, \\ y = \mathbf{c}^T\mathbf{x} \end{cases} \tag{3.1}$$

The matrix $\mathbf{A} \in \mathbb{R}^{n\times n}$ in (3.1) is called the system matrix, and is known as well in other application fields as the stiffness matrix, $\mathbf{E} \in \mathbb{R}^{n\times n}$ is the damping matrix, $\mathbf{b} \in \mathbb{R}^n$ is the input vector, u is the system input signal, $\mathbf{c} \in \mathbb{R}^n$ is the system output vector , $\mathbf{y}$ is the system outputs signal, and finally $\mathbf{x} \in \mathbb{R}^n$ is the state variables vector.

Before we start discussing order reduction methods, we review the concept of the Petrov Galerkin projection, since it is the fundament of many order reduction methods.

3.1.1 The Petrov Galerkin projection

Given a high dimensional state-vector of a dynamic system $\mathbf{x}(t) \in \mathbb{R}^n$, the main idea of the Galerkin Petrov projection is to find a new representation of $\mathbf{x}(t)$ using a much lower number of variables than the ones contained in $\mathbf{x}(t)$. This can be done by expressing $\mathbf{x}(t)$ as a linear combination of $q \ll n$ vectors that are assembled in the so called projection matrix $V \in \mathbb{R}^{n \times q}$. The new representation can be formally written as $\mathbf{x}(t) = \mathbf{V}\mathbf{x}_r(t)$ where $\mathbf{x}_r(t) \in \mathbb{R}^q$ is *reduced order* state vector .
In general, the aforementioned approximation is not exact, and is often accompanied with an approximation error that varies depending on the optimality of the choice of the vectors of the matrix $\mathbf{V}$.
Replacing the state vector in the LTI system (3.1) by its low order approximation gives:

$$\begin{cases} \mathbf{E}\mathbf{V}\dot{\mathbf{x}}_r = \mathbf{A}\mathbf{V}\mathbf{x}_r + \mathbf{b}u + \epsilon(t), \\ y = \mathbf{c}^T\mathbf{V}\mathbf{x}_r, \end{cases} \tag{3.2}$$

where $\epsilon(t)$ is the error vector that results from the low rank approximation of $\mathbf{x}(t)$. It is clear that the system (3.2) is over determined as it has a number of equation n that is larger than the number of unknown variables in $\mathbf{x}_r(t)$. Therefore, in order to find a unique solution to (3.2), the latter system has to be projected on a second subspace whose basis vectors are orthogonal to the residuals vector $\epsilon(t)$ in order to force the projection of $\epsilon(t)$ onto the second subspace to zero.
If we assume that the basis vectors of the second subspace are assembled in the projection matrix $\mathbf{W} \in \mathbb{R}^{n \times q}$, then the system (3.2) after projecting it on the subspace spanned by the columns of $\mathbf{W}$ can be written as:

$$\begin{cases} \mathbf{W}^T\mathbf{E}\mathbf{V}\dot{\mathbf{x}}_r = \mathbf{W}^T\mathbf{A}\mathbf{V}\mathbf{x}_r + \mathbf{W}^T\mathbf{b}u \\ y = \mathbf{c}^T\mathbf{V}\mathbf{x}_r \end{cases} \tag{3.3}$$

where $\mathbf{E}_r = \mathbf{W}^T\mathbf{E}\mathbf{V}, \mathbf{A}_r = \mathbf{W}^T\mathbf{A}\mathbf{V}, \mathbf{b}_r = \mathbf{W}^T\mathbf{b}, \mathbf{c}_r = \mathbf{c}^T\mathbf{V}$, are respectively the matrices and vectors of the reduced order model (3.3).

Most of the order reduction approaches follow the same projection procedure. However, they use different approaches for generating the projection matrices $\mathbf{W}$,$\mathbf{V}$.
It is worth mentioning that in the cases where the two projection matrices are equal $\mathbf{W} = \mathbf{V}$ then the aforementioned projection procedure is called the Galerkin projection.

3.1.2 Truncated balanced realization TBR

This method is based on sorting the state-variables of the dynamic system (3.1) according to their contribution to the system's input-output behavior, and truncating the state-variables which do not have a significant contribution. Two *energy gramian* matrices are used to quantify the contribution of the state variables. The first one is called the *controllability gramian*, it describes the amount of energy needed to be injected in the considered inputs in order to drive each of the state-variables to a required value and is defined by the following integral:

$$\mathbf{P} = \int_0^\infty e^{\mathbf{A}\tau}\mathbf{b}\mathbf{b}^T e^{\mathbf{A}^T\tau} d\tau \tag{3.4}$$

The second matrix is called the observability gramian, it describes the contribution of each of the state-variables to the energy of the considered outputs, and is given by:

$$\mathbf{Q} = \int_0^\infty e^{\mathbf{A}^T\tau}\mathbf{c}^T\mathbf{c}e^{\mathbf{A}\tau} d\tau \tag{3.5}$$

The two previous integrals can be calculated by solving the following two Lyapunov equations which have the dimensions of the original model:

$$\begin{aligned} \mathbf{A}\mathbf{P} + \mathbf{P}\mathbf{A}^T + \mathbf{b}\mathbf{b}^T &= 0 \\ \mathbf{A}^T\mathbf{Q} + \mathbf{Q}\mathbf{A} + \mathbf{c}\mathbf{c}^T &= 0 \end{aligned} \tag{3.6}$$

In order to balance both of the energy contributions that are described in the controllability and the observability gramians, a state *balancing transformation* matrix $\mathbf{T}$ [44, 45] is found and applied to the system (3.1) in order to make the controllability and observability gramians diagonal, equal, and having the *Hankel singular values* (HSV) on their diameter. Finally, the truncation of the states variables that correspond to the smallest

Hankel singular values in the transformed system results in the reduced order model. The aforementioned procedure can be carried out by generating two suitable projection matrices $\mathbf{W}$ and $\mathbf{V}$ [39], and reducing the order of the system (3.1) by projecting it on the subspaces spanned by the columns of the projecting matrices.
The main advantage of the TBR approach is that it preserves the stability [6] in the reduced order model, in addition to the existence of a global apriori error bound between the original and reduced systems [26]. However, its main disadvantage is the high computational cost that is required for solving the two Lyapunov equations. Therefore, several research efforts have been concentrated on finding a computationally cheap approximation to their solution [29, 47].

3.1.3 Krylov-subspace based approaches

In Laplace domain, the transfer function of the LTI system (3.1) is given by:

$$H(s) = \frac{y(s)}{u(s)} = \mathbf{c}^T(s\mathbf{E} - \mathbf{A})^{-1}\mathbf{b}, \tag{3.7}$$

and can be expanded using the Neumann expansion series as:

$$H(s) = \mathbf{c}^T \sum_{i=0}^{\infty} \left(\mathbf{A}^{-1}\mathbf{E}s\right)^i \mathbf{A}^{-1}\mathbf{b} = \sum_{i=0}^{\infty} m_i s^i \tag{3.8}$$

with m_i being the ith *moment* [6, 28] of the transfer function $H(s)$ calculated at an expansion point $s_0 = 0$:

$$m_i = \mathbf{c}^T \left(\mathbf{A}^{-1}\mathbf{E}\right)^i \mathbf{A}^{-1}\mathbf{b}, \qquad i = 0, 1, \cdots. \tag{3.9}$$

The moments, by definition, are the negative coefficients of the Taylor series expansion of the transfer function about the point $s_0 = 0$, and can be calculated for any other expansion point $s_0 \neq 0$ by:

$$m_i^{s_0} = \mathbf{c}^T \left((\mathbf{A} - s_0\mathbf{E})^{-1}\mathbf{E}\right)^i (\mathbf{A} - s_0\mathbf{E})^{-1}\mathbf{b}, \qquad i = 0, 1, \cdots. \tag{3.10}$$

The aim of order reduction by Krylov-subspace methods is to find a reduced order model of order $q \ll n$, whose moments match some of the moments of the original one [23]. This family of methods is also known as moment matching.
A numerically robust and efficient way to calculate this reduced order model is based on applying a projection to the original model,

$$\begin{cases} \mathbf{W}^T\mathbf{E}\mathbf{V}\dot{\mathbf{x}}_r(t) = \mathbf{W}^T\mathbf{A}\mathbf{V}\mathbf{x}_r(t) + \mathbf{W}^T\mathbf{b}u(t), \\ y(t) = \mathbf{c}^T\mathbf{V}\mathbf{x}_r(t), \end{cases} \tag{3.11}$$

by means of the projection matrices, $\mathbf{V}$ and $\mathbf{W}$ with $\mathbf{W}^T\mathbf{V} = \mathbf{I}$.
For the generation of the projection matrices, the Krylov subspace, defined in e.g. [6] is used,

$$\mathcal{K}_q(\mathbf{A}_1, \mathbf{b}_1) = span\{\mathbf{b}_1, \mathbf{A}_1\mathbf{b}_1, \cdots, \mathbf{A}_1^{q-1}\mathbf{b}_1\}$$

where $\mathbf{A}_1 \in \mathbb{R}^{n\times n}$ is a matrix, and $\mathbf{b}_1 \in \mathbb{R}^n$ is called the starting vector.
It can be shown that if the projection matrices are chosen such that,

$$\begin{aligned} colspan(\mathbf{V}) &\subset \mathcal{K}_q\left((\mathbf{A} - s_0\mathbf{E})^{-1}\mathbf{E}, (\mathbf{A} - s_0\mathbf{E})^{-1}\mathbf{b}\right), \\ colspan(\mathbf{W}) &\subset \mathcal{K}_q\left((\mathbf{A} - s_0\mathbf{E})^{-T}\mathbf{E}^T, (\mathbf{A} - s_0\mathbf{E})^{-T}\mathbf{c}^T\right), \end{aligned}$$

then $2q$ moments around s_0 match and the method is known as the two-sided Krylov. Whereas, if only one Krylov subspace is used for the projection by choosing $\mathbf{W} = \mathbf{V}$, then only q moments match between the full order model and the reduced order model, and the method is know as the one-sided Krylov.
For the numerical computation of the matrices $\mathbf{V}$ and $\mathbf{W}$, the known Lanczos or Arnoldi or one of their modified versions are employed. For more details, see e.g. [6, 58] and the references therein.

3.1.4 Proper orthogonal decomposition POD

In the last two paragraphs, we have seen that both of the balanced truncation and the Krylov-subspace based approaches exploit the information contained in the matrices of the LTI system (3.1) in generating the reduction subspace. In contrast to that, the proper orthogonal decomposition POD approach uses the information contained in

multiple observations of the state-vector $\mathbf{x}(t)$ of a dynamic system in building the low dimensional reduction subspace.
If a number of p observations of the state-variables vector $\mathbf{x}(t) \in \mathbb{R}^n$ of a dynamic system are assembled in a so called snapshots matrix:

$$\mathbf{X} = \big[\mathbf{x}_1, \ldots, \mathbf{x}_p\big] \qquad \mathbf{X} \in \mathbb{R}^{n \times p}$$

then the POD approach enables approximating the high dimensional observations in $\mathbf{X}$ by a linear combination of a low number of orthogonal vectors

$$\hat{\mathbf{X}} = \mathbf{V}\mathbf{X}_r \quad \text{such that} \quad \hat{\mathbf{X}} \approx \mathbf{X}$$

where

$$\left.\begin{array}{lll} \mathbf{V} & = [\mathbf{v}_1, \ldots, \mathbf{v}_q] & \mathbf{V} \in \mathbb{R}^{n \times q} \\ \mathbf{X}_r & = [\mathbf{x}_{r1}, \ldots, \mathbf{x}_{rp}] & \mathbf{X_r} \in \mathbb{R}^{q \times p} \end{array}\right\} q < \operatorname{rank}(\mathrm{X})\,.$$

In general, the POD approach can be used to find a low rank approximation of any type of high dimensional observations. Therefore, its usage has been very popular in various application fields, such as signal processing [4, 66], data compression, process identification, speech data classification [37]. Moreover, its ability to formulate the behavior of dynamic systems as a function of a low number of orthogonal vectors [8] has made it popular method for reducing the order of both linear and nonlinear dynamic systems, such as heat transfer model [7, 46], fluid dynamics models [11, 21], aerodynamics models [5].
There are several popular approaches to construct the orthogonal vectors of the matrix $\mathbf{V}$ based on the information contained in the snapshots matrix, such as the principal components analysis PCA, the Karhunen-Loeve decomposition KLD, and the singular values decomposition SVD. However, the authors in [40] have proved the equivalence of the three methods.
In the SVD-based approach, the optimal low rank approximation of $\mathbf{X}$ is formulated as a matrix approximation problem. The approximation accuracy can be expressed in

minimizing a certain norm of the error matrix:

$$\mathbf{E} = \mathbf{X} - \mathbf{V}\mathbf{X_r}$$

This minimization problem can be exactly solved by finding the singular values decomposition $\mathbf{X} = \mathbf{U}\mathbf{\Sigma}\mathbf{W^T}$ and letting the projection matrix $\mathbf{V}$ to be equal to the matrix $\mathbf{U}$, and considering $\mathbf{X_r} = \mathbf{\Sigma}\mathbf{W^T}$ as the reduced order snapshots matrix. However in order to get a low rank approximation of $\mathbf{X}$, only the first q columns of the matrix $\mathbf{U}$ are included in the projection matrix $\mathbf{V}$. This in turns guarantees minimizing both the 2-induced and the Frobenius norms of the error matrix:

$$\min \|\mathbf{E}\|_F = \min \|\mathbf{X} - \mathbf{V}\mathbf{X_r}\|_F = \left(\sum_{i=q+1}^{\text{rank X}} \sigma_i^2(\mathbf{X}) \right)^{1/2} \tag{3.12}$$

assuming that $\sigma_q > \sigma_{q+1}$

It can be clearly seen in (3.12) that the approximation optimality can be improved by taking more columns of $\mathbf{U}$ in the matrix $\mathbf{V}$. Therefore, a trade off between the required approximation accuracy and the dimensionality of the reduced order approximation has to be found. This trade off can be determined by giving the required level of accuracy (e.g. maximum allowed error norm in (3.12)) and finding the required number of basis vectors to achieve it.

It is worth mentioning that in the case where the number of snapshots is smaller than the dimensions of the observed systems, the optimal basis vectors can be found in a cheaper way by performing an eigenvalues decomposition of the autocorrelation matrix $\Psi = \mathbf{X^T}\mathbf{X}$, and using the resulting eigenvectors to construct the optimal basis vectors of $\mathbf{V}$ as shown in [6].

It should be stressed that the optimality of the POD approximation is only guaranteed for the vectors that are contained in the snapshots matrix $\mathbf{X}$. Therefore, in order to achieve a good approximation of the behavior of a dynamic system, the system has to be simulated using suitable excitation signals $\mathbf{u}(t)$ in order to generate enough observations $[\mathbf{x}_1, \ldots, \mathbf{x}_p]$ that represent the dominant behavior of the dynamic system in the considered segments of the state space.

3.2 Model Order Reduction of Nonlinear Systems

In contrast to the field of order reduction of linear time invariant systems where several order reduction methods have been developed and exploited in a wide range of application domains, the field of order reduction of nonlinear dynamic systems has been far less investigated. This can be traced back on one hand to the difficulty of finding an accurate and computationally efficient approximation of the nonlinearities in the original system, and on the other hand due to the problem of finding an optimal reduction subspaces of nonlinear dynamic systems which is still a challenging issue.
In the following paragraphs, we present a simplified categorization of some of the well known methods in this field according to their approach in representing the nonlinearity in the reduced order model.
For more information on model order reduction approaches of nonlinear dynamic systems, the readers are referred to the two comprehensive surveys [43, 48] and the references therein.

3.2.1 Back projection based methods

Given a nonlinear dynamic system of the form:

$$\begin{cases} \dfrac{d}{dt}\mathbf{g}\left(\mathbf{x}\right) = \mathbf{f}\left(\mathbf{x}\right) + \mathbf{b}\left(\mathbf{x}\right) u \\ y = \mathbf{c}^T \mathbf{x} \end{cases} \tag{3.13}$$

in which $\mathbf{x} \in \mathbb{R}^n$ is the state variables vector, $\mathbf{g} : \mathbb{R}^n \rightarrow \mathbb{R}^n$, and $\mathbf{f} : \mathbb{R}^n \rightarrow \mathbb{R}^n$,$\mathbf{b} : \mathbb{R}^n \rightarrow \mathbb{R}^n$ are nonlinear functions depending on the state vector, u is a time dependant input signal, $\mathbf{c} \in \mathbb{R}^n$ is the system output vector, and finally y is the system output signal.
In the back projection method [7, 31, 32] , the nonlinear functions of the high order nonlinear system (3.13) are included directly in the reduced order model, with the main difference that the state variables vector $\mathbf{x}$ is approximated in the reduced order model by a linear combination $\mathbf{x} \approx \mathbf{V}\mathbf{x}_r$ of the columns of the projection matrix $\mathbf{V} \in \mathbb{R}^{n \times q}$ as

follows:

$$\begin{cases} \dfrac{d}{dt}\mathbf{V}^T\mathbf{g}\left(\mathbf{V}\mathbf{x}_r\right) = \mathbf{V}^T\mathbf{f}\left(\mathbf{V}\mathbf{x}_r\right) + \mathbf{V}^T\mathbf{b}\left(\mathbf{V}\mathbf{x}_r\right)u \\ \hat{y} = \mathbf{c}^T\mathbf{V}\mathbf{x}_r \end{cases} \tag{3.14}$$

Preserving the nonlinear function of the original model (3.13) in the reduced order model (3.14) imposes projecting the reduce order state vector $\mathbf{x}_r$ back on the original large dimensional state space $\mathbf{x} \approx \mathbf{V}\mathbf{x}_r$ in each simulation time step in order to evaluate the nonlinear functions. Therefore, we refer to this class of methods by the back projection based methods.

The projection matrix $\mathbf{V}$ can be generated using any of order reduction methods of LTI systems applied to a linearization of the nonlinear system [42], or by applying the proper orthogonal decomposition [11, 61], or by exploiting the extension of the balancing methods to nonlinear dynamic system [59].

The direct inclusion of the original nonlinear functions in reduced order model (3.14) has the advantage of eliminating the approximation error that usually results from approximating the nonlinear functions, which is the case in most of the other approaches. However, this approach suffers from the following disadvantages:

- The computational costs of simulating the reduced order nonlinear model (3.14) is not necessarily lower than simulating the original high order nonlinear system (3.13), since solving the equations of the model (3.14) imposes projecting several vectors on the original high order state-space and projecting them back on the reduction subspace in each simulation time step. The simulation cost becomes even higher when using implicit approaches for the time integration of the system (3.14) as has been demonstrated in [54].

- In the cases where the nonlinear functions are not given in the form of analytic functions, and instead, their evaluation in each simulation step requires calling other simulation tools such as finite elements tools, then including the reduced order model (3.14) in system level simulation tools becomes very cumbersome.

3.2.2 Polynomial approximation - Volterra series

Given a nonlinear dynamic system of the form:

$$\begin{cases} \dfrac{d}{dt}\mathbf{x} = \mathbf{f}(\mathbf{x}) + \mathbf{g}(\mathbf{x})\, u \\ y = \mathbf{c}^T\mathbf{x} \end{cases} \tag{3.15}$$

in this class of methods, the nonlinear functions in (3.15) are approximated using high dimensional polynomial expansions, such as Taylors series or power series of the form:

$$\begin{aligned} \mathbf{f}(\mathbf{x}) &= \mathbf{f}(\mathbf{x}_0) + \mathbf{A}_1 (\mathbf{x}-\mathbf{x}_0)^{(1)} + \mathbf{A}_2 (\mathbf{x}-\mathbf{x}_0)^{(2)} + \mathbf{A}_3 (\mathbf{x}-\mathbf{x}_0)^{(3)} + \cdots \\ \mathbf{g}(\mathbf{x}) &= \mathbf{g}(\mathbf{x}_0) + \mathbf{G}_1 (\mathbf{x}-\mathbf{x}_0)^{(1)} + \mathbf{G}_2 (\mathbf{x}-\mathbf{x}_0)^{(2)} + \mathbf{G}_3 (\mathbf{x}-\mathbf{x}_0)^{(3)} + \cdots \end{aligned} \tag{3.16}$$

where:

$$\begin{aligned} (\mathbf{x}-\mathbf{x}_0)^{(1)} &= (\mathbf{x}-\mathbf{x}_0) \in \mathbb{R}^n \\ (\mathbf{x}-\mathbf{x}_0)^{(2)} &= (\mathbf{x}-\mathbf{x}_0) \otimes (\mathbf{x}-\mathbf{x}_0) \in \mathbb{R}^{n^2} \\ (\mathbf{x}-\mathbf{x}_0)^{(k)} &= (\mathbf{x}-\mathbf{x}_0) \otimes (\mathbf{x}-\mathbf{x}_0) \cdots \otimes (\mathbf{x}-\mathbf{x}_0) \in \mathbb{R}^{n^k} \end{aligned} \tag{3.17}$$

with $\otimes$ being the Kronecker product operator, $\mathbf{x}_0 \in \mathbb{R}^n$ is the expansion point in the state-space of the model (3.15), and $\mathbf{A}_k \in \mathbb{R}^{n\times n^k}$, $\mathbf{G}_k \in \mathbb{R}^{n\times n^k}$ are tensors of k^{th} order. In practice, and in order to keep the dimensionality of the approximation (3.16) within the limits of the available memory storage and computational power, only the first few terms in the expansion (3.16) are considered in the approximation of the original nonlinear functions . However, lessening the number of the considered terms in the approximation often reduces the size of its validity region. This in turn restricts the use of this approach to approximate dynamic systems with weak nonlinearity.

An additional difficulty that accompanies using this approach is the lack of computationally efficient order reduction approaches that consider the higher order terms in (3.16) in the reduction procedure. The authors in [9, 49] have proposed a Krylov subspace based model order reduction approach that considers the higher order terms of the expansion series (3.16) by transforming the system (3.15) to a bilinear system using the Carleman bilinearization [57], then reducing its order using Krylov subspace techniques. Additionally, the same authors have presented a theoretical proof for the matching of

the so called *multimoments* of the kernels of the Volterra-Wiener series [57] between the full order bilinear system and the reduced order one. However, the dimensions of the resulting bilinear system may rapidly goes beyond the available memory storage capacity and computational power.

3.2.3 Trajectory based methods

This class of methods is based on approximating the nonlinear functions in a nonlinear system of the form:

$$\begin{cases} \dfrac{d}{dt}\mathbf{g}\left(\mathbf{x}\right) = \mathbf{f}\left(\mathbf{x}\right) + \mathbf{b}u \\ y = \mathbf{c}^T\mathbf{x} \end{cases} \tag{3.18}$$

by a weighted sum of their polynomial expansions (3.16) at multiple expansion points $\{\mathbf{x}_1, \mathbf{x}_2, \cdots \mathbf{x}_{s_1}\}$ in the state-space.
Two approaches can be categorized under this class of methods, the trajectory piecewise linear TPWL approach [54] and the trajectory piecewise polynomial TPWP approach [19]. The TPWL approach uses only the first two terms from the expansion series (3.16) in the approximation of the nonlinear functions, whereas the TPWP utilizes additionally the higher order terms in the expansion series.

3.2.4 Selection criteria of a model order reduction method for moving nonlinear electromagnetic devices

In this work, the TPWL approach has been selected as a base for developing a new approach for the automatic generation of accurate reduced order simulation models of moving nonlinear electromagnetic devices. The selection is made in favor of the TPWL approach due to:

1. Its ability to approximate nonlinear dynamic systems with strong nonlinear behavior by performing several linearization at multiple points in the state-space of the considered model.

2. Its advantage in preventing the exponential increase in the dimensions of the approximation of the nonlinear functions, which is a major disadvantage of both the Volterra series and the trajectory piecewise polynomial approaches.

3. The existence of several well established order reduction approaches that can be applied to reduce the order of the linearized models.

4. The reduced order model that are generated using the TPWL approach can be easily imported in any system level simulation tool that is capable of solving ordinary differential equations.

3.3 Trajectory Piecewise Linear Model TPWL

The generation of a reduced order model of a nonlinear dynamic system (3.18) using the TPWL approach [53, 54] can be carried out according to the following scheme which is graphically illustrated in Fig. 3.1:

1. Calculate the transient response of the high order nonlinear model (3.18) to one or more selected excitation signals. The path of the state-variable vector $\mathbf{x}(t)$ in the state-space is called a trajectory, and the trajectories that are generated in this step are called *training trajectories*.

2. Apply a certain algorithm for selecting a group of linearization points $\{\mathbf{x}_1, \mathbf{x}_2 \cdots, \mathbf{x}_{s_1}\}$ from all the calculated points on the training trajectories.

3. Linearize the nonlinear functions in (3.18) at the selected linearization points.

4. Reduce the order of all the linearized models from the order n to the order $q << n$ by applying one of the well known order reduction approaches of linear time invariant dynamic systems.

5. Define suitable weighting functions, and approximate the original model (3.18) by a weighted sum of all the reduced order linearized models.

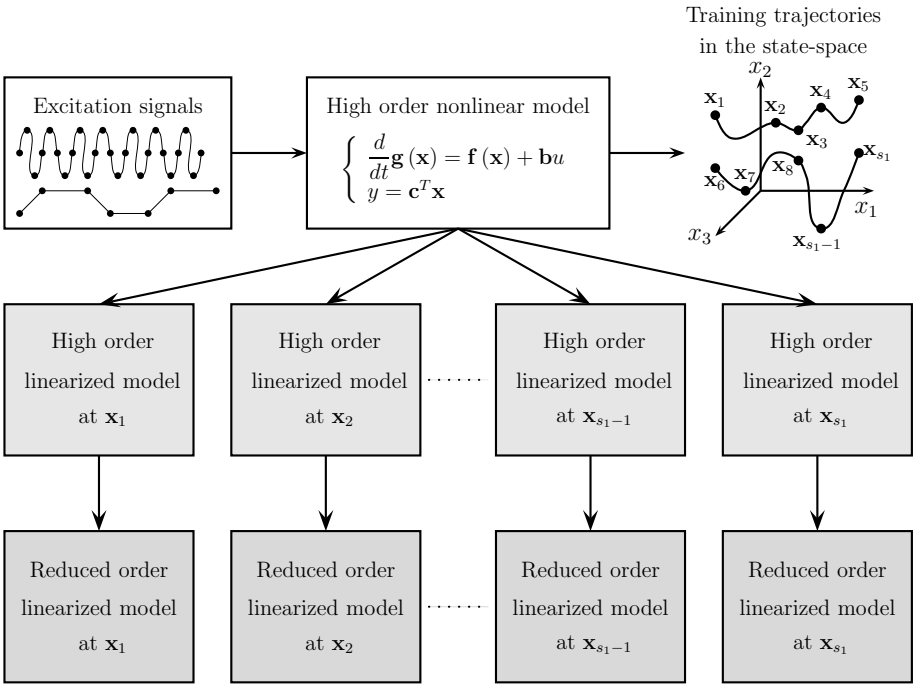

Figure 3.1: A schematic diagram illustrating the procedure of generating a reduced order model of a nonlinear dynamic system using the TPWL approach.

In the next paragraphs, the aforementioned generation steps of a reduced order TPWL model are detailed.

3.3.1 Selecting the training trajectories

Theoretically, in order to achieve a global approximation of the nonlinear functions in the high order nonlinear system (3.18), the training trajectories should visit all the regions in the state-space where the nonlinearities show different behavior. In practice, it is inefficient to do so due to the unaffordable computational costs of performing a large number of simulations using a high order nonlinear model.
In fact, in a large class of industrial systems, a few number of distinguished excitation signals are commonly used for driving a certain electromagnetic device. This limitation in the excitation signals can be mainly traced back to the limitations in the capabilities of the corresponding electrical driving circuits. Such excitation signals together with some of their variations are very good choice for generating the training trajectories,

since this enables approximating the most interesting behavior of the nonlinear system. We stress at this points that the reduced order models that are generated using TPWL can interpolate well among the training trajectories, however, they are typically not capable of extrapolating the behavior of the original model (3.18) at the regions are far away from all the training trajectories.

3.3.2 Selecting the linearization points

In this step of the TPWL generation scheme, a subset of *linearization points* $\{\mathbf{x}_i \in \mathbb{R}^n \quad i = 1, \ldots, s_1\}$ are chosen from the group of all simulation points on the training trajectories. The selection of the number and the location of the linearization points has a major influence on the approximation accuracy of the generated TPWL model. The simplest selection approach is to select all the points on the training trajectories in the group of linearization points. However, doing so increases the computational costs of generating the TPWL models and might increase as well the simulation costs of the generated reduced order TPWL model. The authors in [53] have proposed a selection algorithm that expands the group of linearization points successively during the generation of the training trajectories using the high order model (3.18) as follows:

1. given an initial state vector $\mathbf{x}_0$, a positive number $\delta > 0$, and a user defined number of linearization point $s_1 > 1$;

2. Add the initial state-vector $\mathbf{x}_0$ to the group of linearization points, and set i = 1;

3. Simulate the high order nonlinear system (3.18), during the simulation, if the current state-vector $\mathbf{x}(t)$ is far enough from all the previous linearization points

$$\min_{1 \leq j \leq i} \left(\frac{\|\mathbf{x}(t) - \mathbf{x}_j\|}{\|\mathbf{x}_j\|} \right) \tag{3.19}$$

   then add the current point to the group of linearization points $\mathbf{x}_{i+1} = \mathbf{x}(t)$, and set $i := i + 1$;

4. If $i < s$ return to step 3.

An obvious disadvantage of this algorithm is that it does not exploit any information regarding the nonlinearities of the underlying system. Therefore, even if the underlying system is purely linear, then this algorithm will produce a group of linearization points. The same authors proposed an error estimator based selection algorithm which exploits the Hessian matrix (i.e. the second order derivative of the nonlinear function with respect to the state variables vector). However, the Hessian matrix in a system of order n is in general a tensor of the third order having the dimensions $(n \times n \times n)$, which makes its calculation prohibitively expensive for large scale systems.
A third algorithm for the selection of the linearization points is proposed in [63], and it proceeds as follows:

1. Linearize the nonlinear model (3.18) at all the calculated points on the training trajectories. Each linearized model at a linearization point $\mathbf{x}_i$ is of the form (3.21).

2. Reduce the order of all the linearized models using a suitable reduction method.

3. Remove the similar reduced order linearized models, where two linearized models at two distinguished linearization points $\mathbf{x}_i, \mathbf{x}_j$ are considered to be similar if for a user defined positive numbers $\epsilon, \delta_1, \delta_2$ the following three conditions hold:

$$\frac{\|\mathbf{G}_{ri} - \mathbf{G}_{rj}\|}{\|\mathbf{G}_{ri}\|} < \epsilon, \qquad \frac{\|\mathbf{A}_{ri} - \mathbf{A}_{rj}\|}{\|\mathbf{A}_{ri}\|} < \delta_1, \qquad \frac{\|\mathbf{x}_{ri} - \mathbf{x}_{rj}\|}{\|\mathbf{x}_{ri}\|} < \delta_2, \tag{3.20}$$

where the $\|.\|$ indicates the standard Frobenius vector/matrix norm, and the subscript r refers to the reduced order matrices and vectors.
The major advantage of the aforementioned approach is its incorporation of information regarding the nonlinear behavior of the system (3.18) at different simulation points, this is done by comparing the reduced order Jacobian matrices $\mathbf{A}_{ri}$, $\mathbf{G}_{ri}$ at all the simulation points. However, this approach suggests reducing the order of all the linearized models before selecting the linearization points. This is disadvantageous, since significant information in the full order Jacobian matrices Jacobian matrices $\mathbf{A}_r$, $\mathbf{G}_r$ get lost after the reduction. Moreover, the high computational costs accompanied with linearizing the nonlinear system at all simulation steps, reducing their order, and comparing them

according to the criteria (3.20) is an additional disadvantage of this approach.

3.3.3 Linearizing the nonlinear functions

A nonlinear dynamic system (3.18) of order n can be linearized by expanding its nonlinear functions at a certain point $\mathbf{x}_i \in \mathbb{R}^n$ using a polynomial series expansion (3.16), and taking only the first two terms from the expansion series in the function approximation. This results in a dynamic system of the form:

$$\frac{d}{dt}\left(\mathbf{g}(\mathbf{x}_i) + \mathbf{G}_i\left(\mathbf{x} - \mathbf{x}_i\right)\right) = \mathbf{f}(\mathbf{x}_i) + \mathbf{A}_i\left(\mathbf{x} - \mathbf{x}_i\right) + \mathbf{b}u \tag{3.21}$$

where the matrices $\mathbf{G}_i \in \mathbb{R}^{n\times n}, \mathbf{A}_i \in \mathbb{R}^{n\times n}$ are the Jacobian matrices of the nonlinear functions $\mathbf{g}(\mathbf{x}), \mathbf{f}(\mathbf{x})$ respectively:

$$\mathbf{G}_i = \left.\frac{d\mathbf{g}(\mathbf{x})}{d\mathbf{x}}\right|_{\mathbf{x}_i} \qquad \mathbf{A}_i = \left.\frac{d\mathbf{f}(\mathbf{x})}{d\mathbf{x}}\right|_{\mathbf{x}_i} \tag{3.22}$$

In many numerical simulation tools, the Jacobian matrices are calculated during the simulation in order to enable solving the nonlinear model equations using fast search algorithms such as Newton-Raphson. However, extracting those matrices, especially from commercial modeling tools, is not a trivial task.
After performing the linearization at all the s_1 selected linearization points, the high order nonlinear model (3.18) can be approximated by a weighted sum of all the linearized model:

$$\sum_{i=1}^{s_1} \alpha_i\left(\mathbf{x}\right)\mathbf{G}_i\frac{d}{dt}\mathbf{x} = \sum_{i=1}^{s_1} \alpha_i\left(\mathbf{x}\right)\left[\mathbf{f}(\mathbf{x}_i) + \mathbf{A}_i\left(\mathbf{x} - \mathbf{x}_i\right)\right] + \mathbf{b}u \tag{3.23}$$

where the $\alpha_1, \ldots, \alpha_{s_1}$ are the weighting coefficients which determine the contribution of each of the linearized models to the overall model in every simulation step.

3.3.4 Reducing the order of the linearized Models

It can be seen that trajectory piecewise linear approximation model (3.23) still has the same high order as the original nonlinear model (3.18). The order reduction of the

TPWL model (3.23) might seem from the first glance to be straight forward. However, the situation is a bit more complicated, since the required order reduction approach should be able to generate a reduction subspace that produces an optimal low order approximation of all the linearized models in the TPWL model (3.23).
Two Krylov-subspace based algorithms for reducing the order of the TPWL model have been proposed in [53]. The first algorithm suggests generating a Krylov-reduction subspace at the first linearized model in (3.23) and using it for reducing the order of all other linearized models. However, the matching of moments is only guaranteed for the first linearized model. Therefore, if the other linearized models in the TPWL model have significantly different dynamic behavior than the first linearized model, then the approximation accuracy of the reduced order TPWL will not be satisfactory.
The second algorithm considers generating Krylov subspaces for each of the linearized models as follows:

1. set $V_{agg} = [\,], i = 1$

2. Build the following Krylov subspaces for the i_{th} linearized model:

$$\begin{aligned} &colspan(\mathbf{V}_1) \subset \mathcal{K}_q\left(\mathbf{A}_i^{-1}\mathbf{G}_i, \mathbf{A}^{-1}\mathbf{b}\right), \\ &colspan(\mathbf{V}_2) \subset \mathcal{K}_q\left(\mathbf{A}_i^{-1}\mathbf{G}_i, \mathbf{A}^{-1}\left(\mathbf{f}\left(\mathbf{x}_i\right) - \mathbf{A}_i\mathbf{x}_i\right)\right) \end{aligned} \tag{3.24}$$

   using the Arnoldi algorithm. The first Krylov subspace is necessary in order to guarantee the matching of q moments of the transfer function connecting the model input u to the system output y, whereas the second Krylov subspace is necessary to guarantee the matching of moments of the transfer function connecting the constant vector $\mathbf{f}_i$ to the system output y.

3. Set $\mathbf{V}_{agg} = [\mathbf{V}_{agg}, \mathbf{V}_1, \mathbf{V}_2, \mathbf{x}_i]$;

4. If $i < s_1$ then set $i = i + 1$ and return to 2.

5. Remove the redundant information from the columns of $\mathbf{V}_{agg}$ by orthogonalizing its vectors using singular values decomposition and keeping only the orthogonal vectors that are accompanied with the largest singular values.

The resulting redundancy free matrix $\mathbf{V}_{agg}$ is expected to approximate the Krylov reduction subspaces of all the linearized models, therefore, it is used for reducing the order of all the linearized models in the TPWL model (3.23).
Alternatively, in [27], the simulated state-vectors of the high order nonlinear model (3.18) are exploited by the proper orthogonal decomposition POD approach in generating a projection matrix $\mathbf{V} \in \mathbb{R}^{n\times q}$, which is used for reducing the order of all linearized models in the TPWL model (3.23).
Finally, in [64], the square-root truncated balanced realization TBR [39] is applied to only to one linearized model to generate two projection matrices $\mathbf{V} \in \mathbb{R}^{n\times q}$, $\mathbf{W} \in \mathbb{R}^{n\times q}$. The two latter matrices were used in the next step for reducing the order of all linearized models in the TPWL model (3.23).
All the aforementioned methods produce two projection matrices $\mathbf{V} \in \mathbb{R}^{n\times q}$ and $\mathbf{W} \in \mathbb{R}^{n\times q}$ or one projection matrix $\mathbf{V} \in \mathbb{R}^{n\times q}$ i.e. $\mathbf{W} = \mathbf{V}$. And the final reduced order TPWL model can be generated by applying the Petrov Galerkin projection – that has been reviewed in the subsection 3.1.1 – to project the high order TPWL model onto the subspaces spanned by the columns of the two projection matrices:

$$\sum_{i=1}^{s_1} \alpha_i(\mathbf{x})\, \mathbf{W}^T\mathbf{G}_i\mathbf{V}\frac{d}{dt}\mathbf{x}_r = \sum_{i=1}^{s_1} \alpha_i(\mathbf{x}) \left[\mathbf{W}^T\mathbf{A}_i\mathbf{V}\mathbf{x}_r + \mathbf{W}^T\mathbf{f}(\mathbf{x}_i) - \mathbf{W}^T\mathbf{A}_i\mathbf{x}_i\right] + \mathbf{W}^T\mathbf{b}u. \tag{3.25}$$

Now, by considering that:

$$\mathbf{G}_{ri} = \mathbf{W}^T\mathbf{G}_i\mathbf{V}, \quad \mathbf{A}_{ri} = \mathbf{W}^T\mathbf{A}_i\mathbf{V}, \quad \mathbf{f}_{ri} = \mathbf{W}^T\left(\mathbf{f}(\mathbf{x}_i) - \mathbf{A}_i\mathbf{x}_i\right), \quad \mathbf{b}_r = \mathbf{W}^T\mathbf{b}$$

the final reduced order TPWL model ca be written as:

$$\sum_{i=1}^{s_1} \alpha_i(\mathbf{x})\, \mathbf{G}_{ri}\frac{d}{dt}\mathbf{x}_r = \sum_{i=1}^{s_1} \alpha_i(\mathbf{x}) \left[\mathbf{A}_{ri}\mathbf{x}_r + \mathbf{f}_{ri}\right] + \mathbf{b}_r u \tag{3.26}$$

3.3.5 The choice of weighting functions

When simulating the response of the TPWL model (3.26) to a certain excitation signal $u(t)$, the values of the weighting coefficients $\{\alpha_1, \ldots, \alpha_{s_1}\}$ have to be calculated at each simulation time step in order to determine the contributions of each of the linearized models in (3.26) to the overall approximation. The calculation of the weighting coefficients is done based on the distance between the current state vector $\mathbf{x}(t)$ and all the linearization points $\{\mathbf{x}_1, \ldots, \mathbf{x}_{s_1}\}$ as it is graphically illustrated in Fig. 3.2:

$$(\alpha_1, \ldots, \alpha_{s_1}) = \boldsymbol{\alpha}\big(\mathbf{x}(t), \{\mathbf{x}_1, \ldots \mathbf{x}_{s_1}\}\big) \tag{3.27}$$

The weighting function $\boldsymbol{\alpha}$ should be constructed in such a way that the i^{th} linearized model in (3.26) gets a higher weighting value α_i when the state variables vector $\mathbf{x}(t)$ approaches the linearization point $\mathbf{x}_i$. Later on, the values of all the

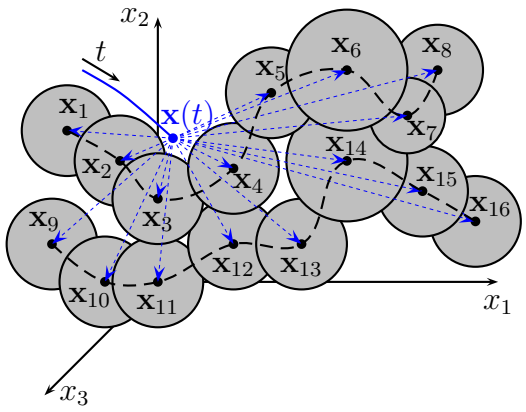

Figure 3.2: Linearizing a nonlinear dynamic system at several linearization points $\{\mathbf{x}_i \in \mathbb{R}^n \quad i = 1, \ldots, 16\}$ along two simulation trajectories. The shaded balls symbolically represent the validity region of each of the linearized models, and the dashed blue lines represent the distance vectors between the current simulation point $\mathbf{x}(t)$ and all the linearization points

weighting coefficients have to be normalized in such a way that their sum is always equal

to one:

$$\sum_{i=1}^{s_1} \alpha_i = 1 \tag{3.28}$$

In this work, similar to [54], the Gaussian functions are used as weighting functions. The detailed weighting scheme can be summarized in the following steps:

1. Calculate the Euclidian distances between the current state variables vector $\mathbf{x}(t)$ and all the linearization points: $d_i = \|\mathbf{x}(t) - \mathbf{x}_i\|_2$ for $i = 1, \ldots, s_1$.

2. Find the smallest distance value $d_{min} = \min(d_1, \ldots, d_{s_1})$, and use it to normalize all the calculated distance values: $\tilde{d}_i = d_i/(d_{min} + \epsilon)$ for $i = 1, \ldots, s_1$, where ϵ is a very small number added in order to avoid the division by zero if $d_{min} = 0$.

3. Calculate the values of the weighting coefficients $\tilde{w}_i = e^{-d_i^2/2\xi^2}$ for $i = 1, \ldots, s_1$, where ξ is the user defined standard deviation constant of the Gaussian function.

4. Normalize the weighting coefficients $w_i = \dfrac{\tilde{w}_i}{\sum_{i=1}^{s_1} \tilde{w}_i}$ for $i = 1, \ldots, s_1$ in order to fulfill the condition (3.28).

The value of the standard deviation constant ξ determines the decaying rate of a weighting coefficients when the state vector $\mathbf{x}(t)$ moves away from their corresponding linearization points, its effect on the TPWL approximation will be illustrated in the following example.

3.3.6 Illustrating example

In order to illustrate the basic idea of the TPWL approach in approximating a nonlinear function by a weighted sum of linearized functions, and in order to demonstrate the influence of both selecting the linearization points and setting the parameters values in the weighting function on the approximation accuracy, we consider the example of a

simple nonlinear function depending on one unknown variable:

$$f(x) = \tanh(0.05x) + 0.0002x + 1 \tag{3.29}$$

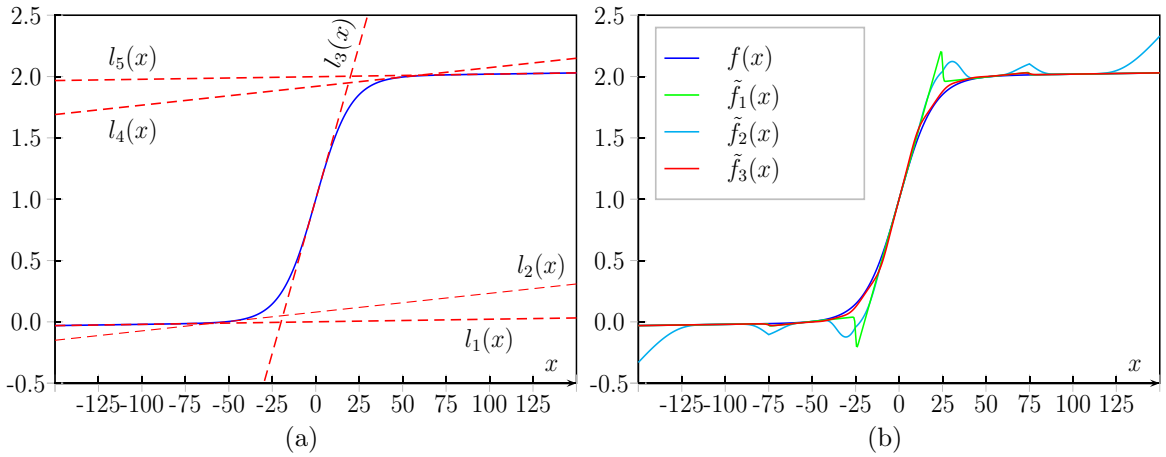

Figure 3.3: Approximating a nonlinear function by different weighted sums of linearized functions

The linearized function of (3.29) at a certain linearization point x_i can be calculated as:

$$\begin{aligned} l(x) &= f(x_i) + \left.\frac{df}{dx}\right|_{x_0} (x - x_i) \\ &= (0.0502 - 0.05\tanh^2(x_i))x - (0.0502 - 0.05\tanh^2(x_i))x_i + y(x_i) \\ &= k_i x + g_i \end{aligned} \tag{3.30}$$

The function $f(x)$ is linearized at five linearization points in the range $x \in [-150, 150]$, namely at the points $x_i = [-100, -50, 0, 50, 100]$. The linearized functions together with the function itself are graphically illustrated in Fig. 3.3.(a).
The function $f(x)$ can be approximated as a weighted sum of the five linearized models:

$$\tilde{f}(x) = \sum_{i=1}^{5} w_i(x)\,[k_i x + g_i] \tag{3.31}$$

in which the weighting coefficients are calculated according to the weighting scheme that has been discussed in the previous paragraph.
Two TPWL approximation functions $\tilde{f}_1(x)$ and $\tilde{f}_2(x)$ of the form (3.31) are generated at the same five linearization points. In the first TPWL model $\tilde{f}_1(x)$ the standard deviation value in the weighting function is set to $\xi = 0.1$, whereas in the approximation function $\tilde{f}_2(x)$ the standard deviation value is set to $\xi = 0.6$.

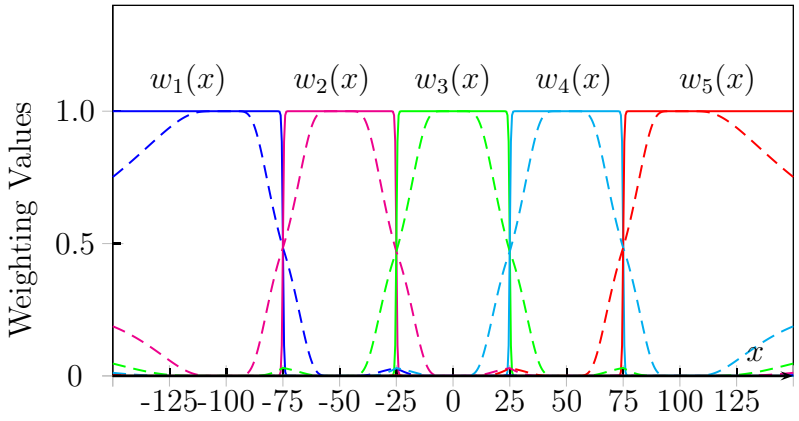

Figure 3.4: The weighting coefficients $\{w_1(x), \ldots, w_5(x)\}$ of the linearized models in the TPWL model, dashed lines corresponds to $\xi = 0.6$, solid lines corresponds to $\xi = 0.1$

The influence of the standard deviation parameter ξ on the form of the weighting coefficients of the linearized models in (3.31) is shown in 3.4. It can be seen that the value $\xi = 0.6$ forces a slow decay of the weighting coefficients when the variable x moves away from their corresponding linearization points. The slow decay causes an increasing overlap among the linearized models. This means that some linearized models will still contribute to the piecewise linear approximation even though the variables x is not located in the neighborhood of their corresponding linearization points. This behavior can be observed for example in the region $x \in [-125, -150]$ where the weighting function $w_4(x)$ of the linearized model $l_4(x)$ still has a relatively large value, which causes a deterioration of the approximation accuracy of $\tilde{f}_2(x)$ in this region as it can be seen in Fig. 3.3.(b).
In contrast, in the case of $\xi = 0.1$, the weighting coefficients decays much faster when

the variable x moves away from their corresponding linearization points. Therefore, the weighting coefficients of the linearized functions $l_1(x), l_2(x), l_3(x), l_4(x)$ have almost zero values in the region $x \in [-125, -150]$, and only the weighting coefficient $w_5(x)$ is active and has a value equal to 1, since its corresponding linearization point $x_5 = -100$ is the nearest to x values in the considered range.

It should be stressed at this point that it is hard to make a general statement on the optimal choice of the parameters of the weighting functions, since a certain tuning of those parameters can achieve good interpolation behavior for some nonlinear functions, and bad for others. However, in all the considered applications in this work, the small values of ξ has always achieved better approximation results.

Finally, in order to demonstrate the importance of selecting the number and the positions of linearization points on the accuracy of the TPWL model, tow further linearization points at $x_i = -25$, $x_i = 25$ are added to the TPWL model (3.31), and the value $\xi = 0.1$ is selected in the weighting function. It can be clearly seen in Fig. 3.3.(b) that the resulting TPWL model $\tilde{f}_3(x)$ produces the best approximation of the original nonlinear function (3.29).

Chapter 4

MODEL ORDER REDUCTION OF LINEAR EM DEVICES

4.1 Overview

In this chapter, we address the issue of generating fast and accurate reduced order models of linear electromagnetic systems that are modeled using the coupled boundary element-finite elements method (BEM-FEM). A special focus is given to electromagnetic devices in which the excitation signal type is changed from current to voltage and vice versa during their operation. The input-output behavior of such devices changes significantly when switching the applied excitation signal type from voltage to current or vice versa. This change in the behavior represents a challenge for applying the Krylov based model order reduction techniques, since the generated reduced EM field models should be able to reproduce the original input-output behavior of both the high order current driven and the high order voltage driven models. Moreover, they should enable a simple procedure for switching the excitation signal type during the simulation run.
In the following paragraphs, we derive both the voltage driven and the current driven models of linear electromagnetic devices. Then, we prove that the input Krylov subspaces of both the voltage driven model and the current driven model are equivalent for any arbitrary number of model inputs. This equivalence allows reducing the order of both models by projecting them onto the same input Krylov subspace. Additionally, it significantly simplifies the procedure of switching the excitation signal type during the device simulation using the reduced order models. The proof presented in this chapter has been in published in our work [1].

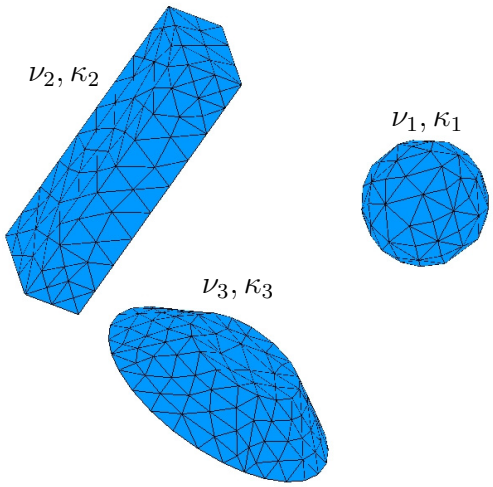

Figure 4.1: A symbolic representation of a spatially discretized electromagnetic device with three segments

It is worth mentioning that the movement of the modeled device components is not considered in this chapter since it causes a nonlinearity in the device model. The latter nonlinearity in addition to the nonlinearity due to the material properties will be considered in details in the following chapter.

4.2 The High Order Linear EM Field Model

If we assume that all modeled device components have fixed positions and do not move under the effect of electromagnetic or mechanical forces, then the matrices $\mathbf{G}$ and $\mathbf{H}$ in the model (2.13) become constant. Additionally, if we assume that the device model can be subdivided to ℓ different regions, each region contains a different *linear* magnetic material which is characterized by a magnetic reluctivity ν_i and an electrical conductivity κ_i as it is shown for example in Fig. 4.1, then the spatially discretized electromagnetic

field model (2.13) can be written as:

$$\begin{bmatrix} \mathbf{C} & 0 \\ 0 & 0 \end{bmatrix} \frac{d}{dt} \begin{bmatrix} \mathbf{a}(t) \\ \mathbf{q}(t) \end{bmatrix} + \begin{bmatrix} \mathbf{K} & -\mathbf{T} \\ \mathbf{H} & \mathbf{G} \end{bmatrix} \begin{bmatrix} \mathbf{a}(t) \\ \mathbf{q}(t) \end{bmatrix} = \begin{bmatrix} \mathbf{r}(t) \\ \mathbf{r}_\gamma(t) \end{bmatrix} \tag{4.1}$$

where the damping matrix $\mathbf{C}$ and the stiffness matrix $\mathbf{K}$ can be calculated respectively as a sum of the individual matrices in the different subregions:

$$\begin{aligned} \mathbf{C} &= \sum_{i=1}^{\ell} \kappa_1 \mathbf{C}_1 + \cdots + \kappa_m \mathbf{C}_m \\ \mathbf{K} &= \sum_{i=1}^{\ell} \nu_1 \mathbf{K}_1 + \cdots + \nu_m \mathbf{K}_m \end{aligned} \tag{4.2}$$

Several outputs can be calculated as functions of state variables of the large scale linear system (4.2). However, in this section we restrict ourselves to the outputs that can be calculated as a linear combination of the state variables:

$$y(t) = \mathbf{l}^T \mathbf{a}(t) \tag{4.3}$$

where $\mathbf{l}$ is the system output vector, and the algebraic variables $\mathbf{q}(t)$ in general do not contribute directly to the typical linear output functions of electromagnetic systems.

4.3 Handling the Singularity

The spatially discretized electromagnetic field model (4.2) is a large scale system of differential algebraic equations (DAE). In control theory, dynamic systems that are modeled using DAEs are called singular systems:

$$\begin{cases} \mathbf{E}\dot{\mathbf{x}}(t) = \mathbf{A}\mathbf{x}(t) + \mathbf{b}u(t) \quad \text{such that} \quad \det(\mathbf{E}) = 0. \\ y(t) = \mathbf{l}^T \mathbf{x} \end{cases} \tag{4.4}$$

Singular systems represent a real challenge for applying model order reduction approaches, and they have to be transformed, in general, to some special canonical forms

before reducing their order. A popular transformation that has been exploited in several works [10, 41, 62] is the *Weierstrass transformation* [24, 38], which aims at separating a singular dynamic system (4.4) with a regular matrix pencil ($\det(\lambda\mathbf{C} - \mathbf{A}) \neq 0$) to a fast subsystem and a slow subsystem:

$$\begin{cases} \dot{\mathbf{x}}_1(t) = \mathbf{J}\mathbf{x}_1(t) + \mathbf{b}_1 u(t) \\ \mathbf{N}\dot{\mathbf{x}}_2(t) = \mathbf{x}_2(t) + \mathbf{b}_2 u(t) \\ y(t) = \mathbf{l}_1^T \mathbf{x}_1 + \mathbf{l}_2^T \mathbf{x}_2 \end{cases} \tag{4.5}$$

where the matrix $\mathbf{N}$ is nilpotent (i.e $\mathbf{N}^\nu = 0$, $\nu >= 1$ is the nilpotency index). Consequently, the system transfer function can be written as:

$$G(s) = \mathbf{l}_1^T (s\mathbf{I} - \mathbf{J})^{-1}\mathbf{b}_1 + \mathbf{l}_2^T (s\mathbf{N} - \mathbf{I})^{-1}\mathbf{b}_2 = G_1(s) + G_2(s) \tag{4.6}$$

The authors in [10, 41, 62] have suggested reducing the order of the slow subsystem $G_1(s)$ using some of the well known order reduction techniques. Moreover, they have stressed on keeping the order of the fast subsystem $G_2(s)$ unchanged, in order to guarantee producing a good approximation of the original system. However, the aforementioned approaches suffer from several disadvantages that limit its application to solve the problem of reducing the order of linear models of electromagnetic device (4.2). Those disadvantages can be summarized in three points:

- The high computational costs and the ill-conditioning of the computational problem of finding the Weierstrass transformation matrices.
- Reducing the order of the slow subsystem $G_1(s)$ only may not produce a, sufficiently, low dimensional approximation of the original system, since the order of the fast subsystem $G_2(s)$,which is not reduced, may still to be high.
- The state variables of the transformed system loose their direct physical interpretation.

Therefore, and considering the above mentioned limitations of applying the *Weierstrass transformation* based approach to electromagnetic system, we propose to handle the

singularity of the system (4.2) by eliminating the algebraic equations. This can be done by solving the algebraic equations for $\mathbf{q}(t)$:

$$\mathbf{q}(t) = -\mathbf{G}^{-1}\mathbf{H}\mathbf{a}(t) + \mathbf{G}^{-1}\mathbf{r}_\gamma(t) \tag{4.7}$$

and substituting its value in (4.2):

$$\mathbf{C}\dot{\mathbf{a}}(t) + \left[\mathbf{K} + \mathbf{K}^{\mathrm{BEM}}\right]\mathbf{a}(t) = \mathbf{r}(t) + \mathbf{T}\mathbf{G}^{-1}\mathbf{r}_\gamma(t) \tag{4.8}$$

where:

$$\mathbf{K}^{\mathrm{BEM}} = \mathbf{T}\mathbf{G}^{-1}\mathbf{H} \tag{4.9}$$

The matrix $\mathbf{K}^{\mathrm{BEM}}$ is called the boundary matrix, its value remains constant when modeling electromagnetic devices with non-moving components. The input signal $\mathbf{r}_\gamma(t)$ corresponds to the contribution of sources of current density that are located in vacuum and not included in the spatial discretization. However, through out the whole work, all sources of current density are included in the vector $\mathbf{r}(t)$. Therefore, the input vector is equal to $\mathbf{r}_\gamma(t) = 0$ in all the considerer systems.

4.4 Krylov Subspace Based Order Reduction

The order of the model (4.8) is already reduced in comparison to the order of the model (4.2) due to the elimination of the algebraic variable $\mathbf{q}(t)$. However, the system (4.8) is still a high dimensional model. Therefore, in this section, we investigate applying the Krylov based model order reduction techniques to achieve a significant reduction in the order of the model (4.8).

At this point, we assume –without loss of generality– that the sources of EM field excitation are electrical coils with homogenous current densities throughout their cross sections. Then, depending on the type of the applied excitation signals (voltage, current), two variant formulations for the models (4.8) can be derived.

4.4.1 Current driven model

Under the assumption that the modeled EM device contains m different excitation coils connected to m different current sources $i_1(t), \ldots, i_m(t)$, the linear model (4.8) can be written as:

$$\mathbf{C}^c\dot{\mathbf{a}}(t) + \left[\mathbf{K} + \mathbf{K}^{BEM}\right]\mathbf{a}(t) = \begin{bmatrix}\mathbf{b}_1 & \ldots & \mathbf{b}_m\end{bmatrix}\begin{bmatrix} i_1(t) \\ \vdots \\ i_m(t)\end{bmatrix}, \tag{4.10}$$

where each of the vectors $\mathbf{b}_i \in \mathbb{R}^n$ describes the distribution of the current density in the i-th excitation coil. The transfer function matrix describing the input-output behavior from each of the m inputs to any linear output of the form $y(t) = \mathbf{l}^T\mathbf{a}$, can be written as:

$$\mathbf{G}^c(s) = \mathbf{l}^T\left(s\mathbf{C}^c - \mathbf{A}\right)^{-1}\mathbf{B}. \tag{4.11}$$

with $\mathbf{B} = [\mathbf{b}_1 \ \ldots \ \mathbf{b}_m]$, and $\mathbf{A} = \left(\mathbf{K} + \mathbf{K}^{BEM}\right)$.

4.4.2 Order reduction of the current-driven model

By expanding the transfer function (4.11) as a Laurent series about a given point s_0, its moments can be calculated. Setting $\mathbf{A}^c_{s_0} = (\mathbf{A} - s_0\mathbf{C}^c)$, the expanded transfer function can be rewritten as:

$$\begin{aligned}\mathbf{G}^c(s) = \mathbf{l}^T\left(\mathbf{A}^c_{s_0}\right)^{-1}\mathbf{B} \ &+ \ \mathbf{l}^T\left(\mathbf{A}^c_{s_0}\right)^{-1}\mathbf{C}^c\left(\mathbf{A}^c_{s_0}\right)^{-1}\mathbf{B}(s-s_0) \\ &+ \ \mathbf{l}^T\left(\left(\mathbf{A}^c_{s_0}\right)^{-1}\mathbf{C}^c\right)^2\left(\mathbf{A}^c_{s_0}\right)^{-1}\mathbf{B}(s-s_0)^2 + \ldots \\ &+ \ \mathbf{l}^T\left(\left(\mathbf{A}^c_{s_0}\right)^{-1}\mathbf{C}^c\right)^{q-1}\left(\mathbf{A}^c_{s_0}\right)^{-1}\mathbf{B}(s-s_0)^{q-1} \ + \ \ldots\end{aligned} \tag{4.12}$$

leading to the general expression of the moments of the system (4.10),

$$\mathbf{m}^c_i = \mathbf{l}^T\left((\mathbf{A}^c_{s_0})^{-1}\mathbf{C}^c\right)^i(\mathbf{A}^c_{s_0})^{-1}\mathbf{B} \qquad i = 0, 1, \cdots. \tag{4.13}$$

Now, based on the previous section and equation (4.13), the system (4.10) can be reduced from order n to order $q << n$ using a one-sided Krylov subspace method where the columns of the projection matrix $\mathbf{V}$ span the following subspace:

$$\begin{aligned}&\mathcal{K}^c_{q_1}\left(\left(\mathbf{A}^c_{s_0}\right)^{-1}\mathbf{C}^c, \left(\mathbf{A}^c_{s_0}\right)^{-1}\mathbf{B}\right) = \\ &span\left\{\left(\mathbf{A}^c_{s_0}\right)^{-1}\mathbf{B}, \left((\mathbf{A}^c_{s_0})^{-1}\mathbf{C}^c\right)(\mathbf{A}^c_{s_0})^{-1}\mathbf{B}, \ldots, \left((\mathbf{A}^c_{s_0})^{-1}\mathbf{C}^c\right)^{q-1}(\mathbf{A}^c_{s_0})^{-1}\mathbf{B}\right\}\end{aligned} \tag{4.14}$$

This choice guarantees the matching of the first $\frac{q}{m}$ moments of the transfer functions of the original and reduced models. Accordingly, the resulting current-driven reduced-order model can be calculated by replacing the original state vector $\mathbf{a}$ in (4.10) by its approximated value $\mathbf{a} \approx \mathbf{W}_c\mathbf{a}^c_r$ as follows:

$$\mathbf{W}^T_c\mathbf{C}^c\mathbf{W}_c\dot{\mathbf{a}}^c_r(t) + \mathbf{W}^T_c\left[\mathbf{K} + \mathbf{K}^{BEM}\right]\mathbf{W}_c\mathbf{a}^c_r(t) = \mathbf{W}^T_c\mathbf{B}\begin{bmatrix} i_1(t) \\ \vdots \\ i_m(t)\end{bmatrix}, \tag{4.15}$$

with $colspan(\mathbf{W}_c) \subset \mathcal{K}^c_{q_1}$.

4.4.3 Voltage driven model

Now, if all the excitation coils of the modeled EM device are connected to voltage sources, the value of the current $i_k(t)$ flowing in the k-th excitation coil can be calculated from [55]:

$$i_k(t) = \mathbf{b}^T_k\dot{\mathbf{a}}(t) - \frac{u_k(t)}{R_k}, \tag{4.16}$$

where R_k is the Ohmic resistance of the k-th excitation coil, and $u_k(t)$ is the voltage signal applied to its terminals. By substituting the excitation currents values from (2.24) in (4.10) and assuming that $\tilde{\mathbf{B}} = \left[\frac{\mathbf{b}_1}{R_1}, \quad \ldots \quad, \frac{\mathbf{b}_m}{R_m}\right]$, the formulation of the voltage driven

EM field model is found to be:

$$\left[\mathbf{C}+\mathbf{B}\tilde{\mathbf{B}}^T\right]\dot{\mathbf{a}}(t)+\left[\mathbf{K}+\mathbf{K}^{BEM}\right]\mathbf{a}(t)=\tilde{\mathbf{B}}\begin{bmatrix}u_1(t)\\ \vdots \\ u_m(t)\end{bmatrix}., \tag{4.17}$$

with its transfer function

$$\mathbf{G}^v(s)=\mathbf{l}^T\left(s\mathbf{C}^v-\mathbf{A}\right)^{-1}\tilde{\mathbf{B}}, \tag{4.18}$$

where $\mathbf{C}^v=\left(\mathbf{C}^c+\mathbf{B}\tilde{\mathbf{B}}^T\right)$.

4.4.4 Order reduction of the voltage driven model

Similar to the current-driven model case, and by setting $\mathbf{A}^v_{s_0}=\left(\mathbf{A}-s_0\mathbf{C}^c-s_0\mathbf{B}\tilde{\mathbf{B}}^T\right)$ the transfer function of the voltage-driven model expanded about s_0 can be shown to be:

$$\begin{aligned}\mathbf{G}^v(s)=&\,\mathbf{l}^T\left(\mathbf{A}^v_{s_0}\right)^{-1}\tilde{\mathbf{B}}\;+\;\mathbf{l}^T\left(\mathbf{A}^v_{s_0}\right)^{-1}\mathbf{C}^v\left(\mathbf{A}^v_{s_0}\right)^{-1}\tilde{\mathbf{B}}(s-s_0)\\&+\;\mathbf{l}^T\left(\left(\mathbf{A}^v_{s_0}\right)^{-1}\mathbf{C}^v\right)^2\left(\mathbf{A}^v_{s_0}\right)^{-1}\mathbf{B}(s-s_0)^2+\ldots\\&+\;\mathbf{l}^T\left(\left(\mathbf{A}^c_{s_0}\right)^{-1}\mathbf{C}^v\right)^{q-1}\left(\mathbf{A}^v_{s_0}\right)^{-1}\tilde{\mathbf{B}}(s-s_0)^{q-1}\;+\;\ldots\end{aligned} \tag{4.19}$$

Accordingly, the moments of this system can be calculated as:

$$\mathbf{m}^v_i=\mathbf{l}^T\left((\mathbf{A}^v_{s_0})^{-1}\mathbf{C}^v\right)^i(\mathbf{A}^v_{s_0})^{-1}\tilde{\mathbf{B}}\qquad i=0,1,\cdots. \tag{4.20}$$

Hence, the voltage-driven model (4.17) can be reduced by projection in a similar way to the current-driven model using the following Krylov subspace:

$$\begin{aligned}&\mathcal{K}^v_{q_1}(\left(\mathbf{A}^v_{s_0}\right)^{-1}\mathbf{C}^v,\left(\mathbf{A}^v_{s_0}\right)^{-1}\tilde{\mathbf{B}})=\\&span\left\{\left(\mathbf{A}^v_{s_0}\right)^{-1}\tilde{\mathbf{B}},\left((\mathbf{A}^v_{s_0})^{-1}\mathbf{C}^v\right)(\mathbf{A}^v_{s_0})^{-1}\tilde{\mathbf{B}},\ldots,\left((\mathbf{A}^v_{s_0})^{-1}\mathbf{C}^v\right)^{q_1-1}(\mathbf{A}^v_{s_0})^{-1}\tilde{\mathbf{B}}\right\}\end{aligned} \tag{4.21}$$

This choice guarantees the matching of the first $\frac{q}{m}$ moments of the transfer functions of the original and reduced models. Accordingly, the resulting current-driven reduced-

order model can be calculated by replacing the original state vector $\mathbf{a}$ in (4.17) by its approximated value $\mathbf{a} \approx \mathbf{W}_v \mathbf{a}_r^v$ as follows:

$$\mathbf{W}_v^T \left[\mathbf{C} + \mathbf{B}\tilde{\mathbf{B}}^T\right] \mathbf{W}_v \dot{\mathbf{a}}_r^v(t) + \mathbf{W}_v^T \left[\mathbf{K} + \mathbf{K}^{BEM}\right] \mathbf{W}_v \mathbf{a}_r^v(t) = \mathbf{W}_v^T \tilde{\mathbf{B}} \begin{bmatrix} u_1(t) \\ \vdots \\ u_m(t) \end{bmatrix}, \quad (4.22)$$

with $colspan(\mathbf{W}_v) \subset \mathcal{K}_{q_1}^v$.

4.4.5 The equivalence of the input Krylov subspaces

As they involve different matrices and vectors, the input Krylov subspaces (4.14), (4.21) involved in the reduction of the current and voltage-driven models seem to be different. However, by closely examining the connections between the involved matrices and vectors, it can be shown that these two subspaces are equal when calculated at the same expansion point s_0.

Theorem 1: The input Krylov subspaces of the current-driven model $\mathcal{K}_{q_1}^c$ and that of the voltage-driven model $\mathcal{K}_{q_1}^v$ are equal.

Proof: Let $\mathbf{M}_i$ and $\mathbf{N}_i$ be the basic blocks of the Krylov subspace $\mathcal{K}_{q_1}^c$ and $\mathcal{K}_{q_1}^v$ respectively. It is shown that the two subspaces span the same space by proving that the i-th basic block of the second one can be written as a linear combination of the first i blocks of the first one.

Recall the *Woodbury formula* [65] employed generally to reformulate the inverse of the sum of two matrices,

$$(\mathbf{M} + \mathbf{PQ})^{-1} = \mathbf{M}^{-1} - \mathbf{M}^{-1}\mathbf{P}\left(\mathbf{I} + \mathbf{QM}^{-1}\mathbf{P}\right)^{-1}\mathbf{QM}^{-1}, \quad (4.23)$$

where $\mathbf{M} \in \mathbb{R}^{n\times n}$ is an arbitrary invertible matrix and $\mathbf{P} \in \mathbb{R}^{n\times m}$, $\mathbf{Q} \in \mathbb{R}^{m\times n}$ are arbitrary matrices. Applying this formula to inverse the matrix $\mathbf{A}^v_{s_0}$ in (4.21) results in:

$$\begin{aligned}\left(\mathbf{A}^v_{s_0}\right)^{-1} &= \left(\mathbf{A}^c_{s_0} - s_0\mathbf{B}\tilde{\mathbf{B}}^T\right)^{-1} \\ &= \left(\mathbf{A}^c_{s_0}\right)^{-1} - s_0\left(\mathbf{A}^c_{s_0}\right)^{-1}\mathbf{B}\left(\mathbf{I} + s_0\tilde{\mathbf{B}}^T\left(\mathbf{A}^c_{s_0}\right)^{-1}\mathbf{B}\right)^{-1}\tilde{\mathbf{B}}^T\left(\mathbf{A}^c_{s_0}\right)^{-1} \\ &= \left(\mathbf{A}^c_{s_0}\right)^{-1} - s_0\left(\mathbf{A}^c_{s_0}\right)^{-1}\mathbf{B}\mathbf{D}_{s_0}\tilde{\mathbf{B}}^T\left(\mathbf{A}^c_{s_0}\right)^{-1},\end{aligned} \tag{4.24}$$

where $\mathbf{D}_{s_0} = \left(\mathbf{I} + s_0\tilde{\mathbf{B}}^T\left(\mathbf{A}^c_{s_0}\right)^{-1}\mathbf{B}\right)^{-1} \in \mathbb{R}^{m\times m}$.
The starting vectors block of the input Krylov subspace (4.14) of the current driven model is given by:

$$\mathbf{M}_1 = \left(\mathbf{A}^c_{s_0}\right)^{-1}\mathbf{B}. \tag{4.25}$$

The starting vectors block for the subspace (4.21) of the voltage driven model is given by:

$$\begin{aligned}\mathbf{N}_1 = \left(\mathbf{A}^c_{s_0} - s_0\mathbf{B}\tilde{\mathbf{B}}^T\right)^{-1}\tilde{\mathbf{B}} &= \left(\mathbf{A}^c_{s_0}\right)^{-1}\tilde{\mathbf{B}} - s_0\left(\mathbf{A}^c_{s_0}\right)^{-1}\mathbf{B}\mathbf{D}_{s_0}\tilde{\mathbf{B}}^T\left(\mathbf{A}^c_{s_0}\right)^{-1}\tilde{\mathbf{B}} \\ &= \left(\mathbf{A}^c_{s_0}\right)^{-1}\mathbf{B}\mathbf{\Phi}_1 = \mathbf{M}_1\mathbf{\Phi}_1.\end{aligned} \tag{4.26}$$

where $\mathbf{\Phi}_1 = \left(diag\left(\left[\frac{1}{R_1},\ldots,\frac{1}{R_m}\right]\right) - s_0\mathbf{D}_{s_0}\tilde{\mathbf{B}}^T\left(\mathbf{A}^c_{s_0}\right)^{-1}\tilde{\mathbf{B}}\right) \in \mathbb{R}^{m\times m}$.

The second vectors block of the input Krylov subspace (4.21) is given by:

$$\begin{aligned}\mathbf{N}_2 &= \left(\left(\mathbf{A}^c_{s_0}\right)^{-1} - s_0\mathbf{B}\tilde{\mathbf{B}}^T\right)^{-1}\left(\mathbf{C}^c + \mathbf{B}\tilde{\mathbf{B}}^T\right)\left(\mathbf{A}^c_{s_0} - s_0\mathbf{B}\tilde{\mathbf{B}}^T\right)^{-1}\tilde{\mathbf{B}} \\ &= \left(\left(\mathbf{A}^c_{s_0}\right)^{-1} - s_0\left(\mathbf{A}^c_{s_0}\right)^{-1}\mathbf{B}\mathbf{D}_{s_0}\tilde{\mathbf{B}}^T\left(\mathbf{A}^c_{s_0}\right)^{-1}\right)\left(\mathbf{C}^c + \mathbf{B}\tilde{\mathbf{B}}^T\right)\left(\mathbf{A}^c_{s_0}\right)^{-1}\mathbf{B}\mathbf{\Phi}_1 \\ &= \left(\mathbf{A}^c_{s_0}\right)^{-1}\mathbf{C}^c\left(\mathbf{A}^c_{s_0}\right)^{-1}\mathbf{B}\mathbf{\Phi}_1 - \left(\mathbf{A}^c_{s_0}\right)^{-1}\mathbf{B}\mathbf{D}_{s_0}\tilde{\mathbf{B}}^T\tilde{\mathbf{A}}^{-1}_{s_0}\mathbf{C}^c\left(\mathbf{A}^c_{s_0}\right)^{-1}\mathbf{B}\mathbf{\Phi}_1 s_0 \\ &\quad + \left(\mathbf{A}^c_{s_0}\right)^{-1}\mathbf{B}\tilde{\mathbf{B}}^T\left(\mathbf{A}^c_{s_0}\right)^{-1}\mathbf{B}\mathbf{\Phi}_1 \\ &\quad - \left(\mathbf{A}^c_{s_0}\right)^{-1}\mathbf{B}\mathbf{D}_{s_0}\tilde{\mathbf{B}}^T\left(\mathbf{A}^c_{s_0}\right)^{-1}\mathbf{B}\tilde{\mathbf{B}}^T\left(\mathbf{A}^c_{s_0}\right)^{-1}\mathbf{B}\mathbf{\Phi}_1 s_0 \\ &= \left(\mathbf{A}^c_{s_0}\right)^{-1}\mathbf{C}^c\left(\mathbf{A}^c_{s_0}\right)^{-1}\mathbf{B}\mathbf{\Phi}_1 + \left(\mathbf{A}^c_{s_0}\right)^{-1}\mathbf{B}\mathbf{\Phi}_2 \\ &= \mathbf{M}_2\mathbf{\Phi}_1 + \mathbf{M}_1\mathbf{\Phi}_2\end{aligned} \tag{4.27}$$

with $\mathbf{\Phi}_2 = \Big(-\mathbf{D}_{s_0}\tilde{\mathbf{B}}^T \left(\mathbf{A}^c_{s_0}\right)^{-1} \mathbf{C}^c \left(\mathbf{A}^c_{s_0}\right)^{-1} \mathbf{B}\mathbf{\Phi}_1 s_0$
$+\tilde{\mathbf{B}}^T \left(\mathbf{A}^c_{s_0}\right)^{-1} \mathbf{B}\mathbf{\Phi}_1 - \mathbf{D}_{s_0}\tilde{\mathbf{B}}^T \left(\mathbf{A}^c_{s_0}\right)^{-1} \mathbf{B}\tilde{\mathbf{B}}^T \left(\mathbf{A}^c_{s_0}\right)^{-1} \mathbf{B}\mathbf{\Phi}_1 s_0\Big) \in \mathbb{R}^{m\times m}$.

Now consider that $\mathbf{N}_{q-1} = \mathbf{M}_{q-1}\mathbf{\Phi}_1 + \cdots + \mathbf{M}_1\mathbf{\Phi}_{q-1}$, for $\mathbf{N}_q$ we have:

$$\begin{aligned}
\mathbf{N}_q &= \left(\left(\tilde{\mathbf{A}}_{s_0} - s_0\mathbf{B}\tilde{\mathbf{B}}^T\right)^{-1}\left(\mathbf{C}^c + \mathbf{B}\tilde{\mathbf{B}}^T\right)\right)\mathbf{N}_{q-1} \\
&= \left(\left(\mathbf{A}^c_{s_0}\right)^{-1} - s_0\left(\mathbf{A}^c_{s_0}\right)^{-1}\mathbf{B}\mathbf{D}_{s_0}\tilde{\mathbf{B}}^T\left(\mathbf{A}^c_{s_0}\right)^{-1}\right)\left(\mathbf{C}^c + \mathbf{B}\tilde{\mathbf{B}}^T\right)\left(\mathbf{M}_{q-1}\mathbf{\Phi}_1 + \cdots + \mathbf{M}_1\mathbf{\Phi}_{q-1}\right) \\
&= \left(\mathbf{A}^c_{s_0}\right)^{-1}\mathbf{C}^c\mathbf{V}_{q-1}\mathbf{\Phi}_1 + \cdots + \left(\mathbf{A}^c_{s_0}\right)^{-1}\mathbf{C}^c\mathbf{M}_1\mathbf{\Phi}_{q-1} \\
&\quad + \left(\mathbf{A}^c_{s_0}\right)^{-1}\mathbf{B}\tilde{\mathbf{B}}\left(\mathbf{M}_{q-1}\mathbf{\Phi}_1 + \cdots + \mathbf{M}_1\mathbf{\Phi}_{q-1}\right) \\
&\quad - \left(\mathbf{A}^c_{s_0}\right)^{-1}\mathbf{B}\mathbf{D}_{s_0}\tilde{\mathbf{B}}^T\left(\mathbf{A}^c_{s_0}\right)^{-1}\left(\mathbf{C} + \mathbf{B}\tilde{\mathbf{B}}^T\right)\left(\mathbf{M}_{q-1}\mathbf{\Phi}_1 + \cdots + \mathbf{M}_1\mathbf{\Phi}_{q-1}\right)s_0 \\
&= \mathbf{M}_q\mathbf{\Phi}_1 + \mathbf{M}_{q-1}\mathbf{\Phi}_2 + \cdots + \mathbf{M}_1\mathbf{\Phi}_q.
\end{aligned} \tag{4.28}$$

This part of the proof is completed by induction. ■

Remark 1: The presented proof considers the most general case of MIMO systems with an expansion point $s_0 \neq 0$. The subspaces of Theorem 1 are also equal for the SISO case and/or $s_0 = 0$.

Consequently, the order of the voltage driven model and the current driven model can be reduced using the same input Krylov subspace, e.g. (4.14), while still guaranteeing the matching of the first $\frac{q}{m}$ moments between each of the original models and their corresponding reduced ones.

In order to illustrate the advantages of the presented proof, we assume that the response of a linear electromagnetic to a given voltage signal is simulated using the voltage driven reduced order model (4.22). During the simulation time interval $t_0 \rightarrow t_s$ the value of the state vector evolves from its initial value to a new value $\mathbf{a}^v_r(t_0) \rightarrow \mathbf{a}^v_r(t_s)$. At the time point t_s we assume that the excitation signal is switched from voltage to current. Therefore, the simulation has to be continued using the current driven reduced order model (4.15). However, in order to calculate the initial conditions $\mathbf{a}^c_r(t_s)$ for the sim-

ulation using (4.15) the current state of device model $\mathbf{a}_r^v(t_s)$ has to be projected onto the subspace of the current driven model. This can be done by projecting $\mathbf{a}_r^v(t_s)$ back onto the full order space $\mathbf{a}(t_s) \approx \mathbf{a}_r^v(t_s)$ and then projecting the result onto the subspace of the current driven model $\mathbf{a}_r^c(t_s) \approx \mathbf{W}_c^T\mathbf{W}_v\mathbf{a}_r^v(t_s)$. It is clear that the transformation between the subspace is accompanied with an approximation error as the back projection on the full order subspace does not reproduce the exact high order state vector. Moreover, the transformation matrices $\mathbf{W}_c^T\mathbf{W}_v$ and $\mathbf{W}_v^T\mathbf{W}_c$ have to be saved and loaded during the simulation. In contrast, the presented proof enables projecting both models (4.10),(4.17) onto the same subspace, this means that the state vectors $\mathbf{a}_r^c(t_s) = \mathbf{a}_r^v(t_s)$.

4.4.6 Numerical example

In this section, the results presented in this work are employed to perform a fast simulation of the behavior of electromagnetic field in the electrical transformer shown in Fig. 4.2. The transformer circuit contains beside the transformer itself a voltage source, and a current limiter. The resistors R_1 and R_2 represent respectively the Ohmic resistances of the primary and secondary transformer coils. The terminals of the secondary coil in this example are not connected to a load, i.e $i_2(t) = 0$. This results in an electromagnetic system having only one excitation coil, and consequently one input, i.e. $m = 1$.

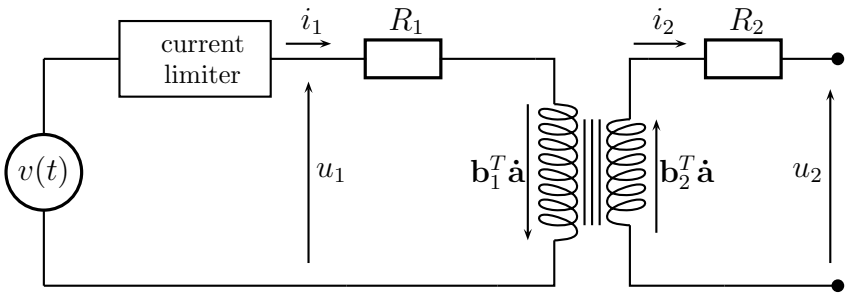

Figure 4.2: Electrical circuit containing an electrical transformer, a current limiter, and a voltage source $v(t)$.

The current limiter is only activated when the absolute value of the primary current $i_1(t)$ reaches the maximum allowed value i_{max}. During its activation, it adjusts the terminal

voltage $u_1(t)$ of the primary coil in order to avoid that the primary current exceeds i_{max}, as follows:

$$\begin{cases} i_1 = +i_{max}, & \text{if } i_1 > i_{max}; \\ i_1 = -i_{max}, & \text{if } i_1 < -i_{max}. \end{cases} \tag{4.29}$$

The simplest and most common way to model the influence of the current limiter on the behavior of the transformer circuit is to consider it, in its activation intervals, as a constant current sources, i.e. $i_1 = \pm i_{max}$. Therefore, the excitation signal has to be switched from a voltage signal to a current signal in the time intervals during which the current limiter is activated. Now, in the time intervals during which the current limiter is not activated, it passes the voltage signal generated by the voltage source directly to the primary coil, i.e. $u_1(t) = v(t)$.

A spatially discretized model of the electromagnetic field in the electrical transformer is generated using the coupled BEM-FEM method. The generated model is a high dimensional system of differential algebraic equations DAEs (4.2) of order $n = 3186$. The singularity of the system is handled by eliminating the algebraic part. This in turn transforms the DAEs system (4.2) to a system of ordinary differential equations (4.8) of order $n = 2614$. All the magnetic materials that are included in the transformer model are assumed to have linear magnetic properties. An input Krylov subspace (4.14) of the current driven model (4.10) is generated using the Arnoldi algorithm at the expansion point $s_0 = 0$. Both the current-driven model (4.10) and the voltage driven one (4.17) are reduced using a one-sided method ($\mathbf{V} = \mathbf{W}$) from order $n = 2614$ to order $n = 20$ by the same projection matrices calculated from the input Krylov subspace generated in the previous step. This in turn guarantees the matching of the first 20 moments between the transfer functions of the full order models (4.10),(4.17) and their corresponding reduced order models as proven in the previous section.

We remind at this point that the common aim of model order approaches is to approximate the original state vector of a system by a linear combination of a low number of optimally chosen basis vectors, i.e. $\mathbf{a} = \mathbf{V}\mathbf{a}_r$. This means that the original distribution of the electromagnetic field in the electrical transformer can be approximated in the

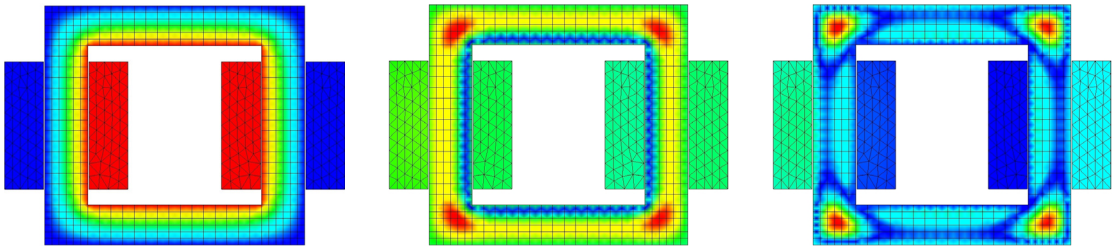

(a) First vector (b) Second vector (c) Third vector

Figure 4.3: The figures (a)-(c) illustrate the electromagnetic field distribution that corresponds to the first three vectors of the input Krylov subspace of the current driven transformer model

reduced-order models by a weighted combinations of the twenty vectors of the input Krylov subspace. Hence, it is interesting to illustrate some of those basis vectors. In Figure 4.3, the electromagnetic field distributions corresponding to the first three vectors of the involved Krylov subspace are graphically illustrated.

After generating the reduced order models, their performance is validated by comparing the corresponding simulation results to the ones obtained by the original high-order models. The first simulation run is carried out using the full order models (4.17), (4.10). At the beginning, the simulation run is started using the voltage driven model (4.17) with the input voltage signal being equal to $u_1(t) = v(t) = 100 \sin 2000t$, as shown in Fig. 4.4. During the progress of simulation, the value of the primary current starts to rise until it reaches the maximum allowed current value $i_{max} = 4\text{A}$. At this point, the current limiter is activated and starts maintaining the primary current value at its maximum allowed value $i_1 = i_{max}$. Therefore, the simulation is continued from this point on using the current-driven model (4.10) with an input signal amplitude of $i_1 = 4\text{A}$. The last value of the state vector $\mathbf{a}(t)$ is used as an initial condition for simulating the current-driven model, as both models have the same states. The simulation is switched back again to the voltage-driven model as soon as the value of the sinusoidal voltage signal $v(t)$ becomes smaller than the terminal voltage $u_1(t)$ of the primary coil. The switching cycle from voltage to current and vice versa is repeated according to the aforementioned switching algorithm until the end of the simulation as shown in Fig. (4.4). The second simulation run is performed using the generated reduced order electromagnetic field models. The

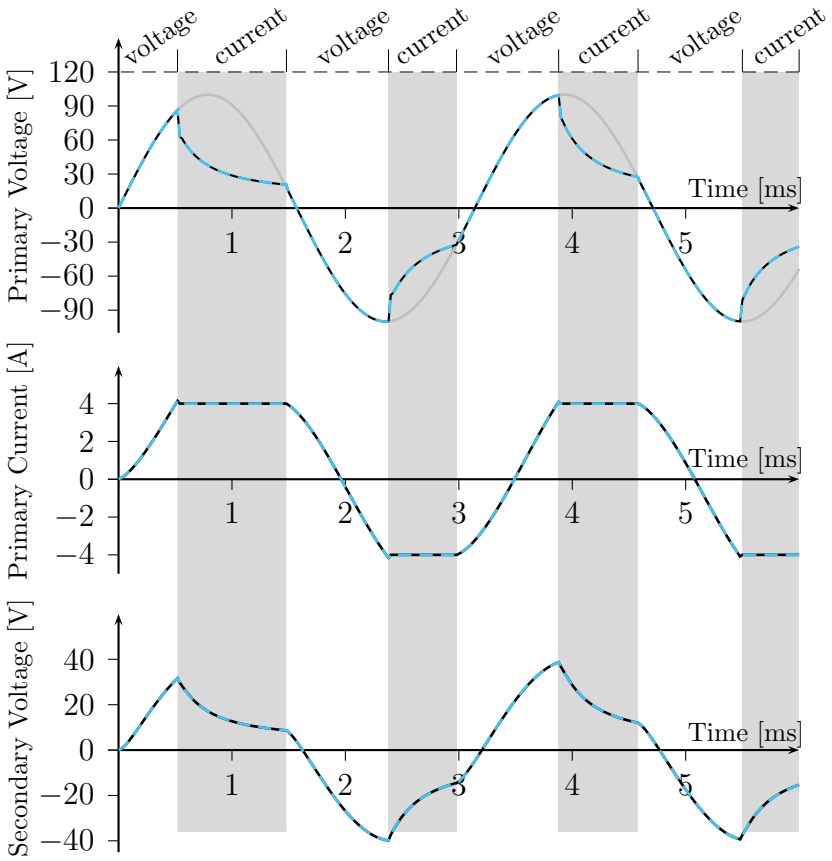

Figure 4.4: A comparison between the simulation results of the full order electromagnetic field models $n = 3186$ (solid lines) and the reduced order models $n = 20$ (dashed lines). The shaded regions represent the intervals during which the simulation is carried out using the current drive models, whereas the other regions represent the intervals during which the simulation is performed using the voltage driven model. The gray line represents the signal of the voltage source $v(t)$.

switching logic between the reduced-order voltage-driven and current-driven models is carried out according to the same switching algorithm used for the full order models. At each switching point between the voltage driven model and the current driven model, the current value of the reduced order state vector $\mathbf{a}_r(t)$ is used as an initial condition for solving the model equations in the next simulation step. No coordinate transformation is required at this point, since both the current-driven and the voltage-driven models are projected to the same subspace. This is in fact one of the major benefits of the results presented in this paper.

	Full Order Models	Reduced Order Models
order	$n = 3186$	$n = 20$
number of simulation steps	300	300
simulation step size	20 μsec	20 μsec
simulation time	127.43 sec	0.1451 sec

Table 4.1: The simulation time of the full order electromagnetic field model of an electrical transformer versus the reduced order model

Finally, the simulation results using the reduced order models that are illustrated in Fig. (4.4) show that the reduced-order model of order $n = 20$ produces an excellent approximation of the simulation results using the original high order model of order $n = 3186$, while being almost 900 times faster as listed in Table 4.1.

Chapter 5

MODEL ORDER REDUCTION OF MOVING NONLINEAR EM DEVICES

5.1 Overview

In this chapter, we present a novel approach for generating fast and accurate reduced order models of electromagnetic devices that contain moving components and magnetic materials with nonlinear properties. The approach exploits model order reduction techniques to approximate the high order nonlinear models of the electromagnetic field by reduced order ones having a much lower number of equations. The reduced order EM field models are weakly coupled to the mechanical equations in order to model the movement of the device components. The position information that are obtained from solving the mechanical equations are used in each simulation time step to update the position dependent terms in the reduced order EM field model.
In the first step in this chapter, the trajectory piecewise linear models approach TPWL [53] is exploited in approximating the nonlinearity in the EM field model that is caused by the dependency of the materials properties on the applied EM field. A novel algorithm for the optimal selection of the number and the position of the linearization points in the TPWL method is presented. The proposed selection algorithm exploits the changes in the materials properties at the different simulation points in determining both the number and the positions of the linearization points in the TPWL model.
In the second step, the work is extend to consider the nonlinearity in the high order electromagnetic field model that is caused by the movement of the device components. This kind of nonlinearity occurs in a large class of electromagnetic devices such as rotating

electrical machines and electromagnetic valves, and it poses a new challenge to model order reduction approaches as it depends on the state-variables of the weakly coupled mechanical equations. In order to tackle this challenge, a novel approach that enable updating the EM field model during the simulation according to the new components positions is introduced. The performance of the new approach is demonstrated by applying it to generate a reduced order model of an electromagnetic valve. The reduced order model is exploited later on to perform a multiobjective optimization of the design of the modeled device.

5.2 The High Order Nonlinear EM Filed Model

In chapter 2, we have reviewed the modeling of electromagnetic devices using the coupled boundary elements finite elements method BEM-FEM, and we have shown that the spatially discretized EM field model (2.13) is a large scale system of nonlinear differential algebraic equations. The algebraic variables vector $\mathbf{q}(t)$ can be eliminated from (2.13) by solving the algebraic equations according to (4.7),(4.9). We remind at this point that in this work, we consider that all sources of current density are included in the vector $\mathbf{r}(t)$. Therefore, the input vector is equal to $\mathbf{r}_\gamma(t) = 0$ in (4.7).
Under the previous assumption, the final high order model can be written as:

$$\mathbf{C}\dot{\mathbf{a}}(t) + \left[\mathbf{K}\left(\mathbf{a}\right) + \mathbf{K}^{\mathrm{BEM}}(\mathbf{x})\right]\mathbf{a}(t) = \mathbf{r}(t) \tag{5.1}$$

The dependency of the stiffness matrix term $\mathbf{K}\left(\mathbf{a}\right)$ in (5.1) on the state variables $\mathbf{a}$ of electromagnetic field can be traced back the dependency of the magnetic reluctivity ν in the modeled materials on the value of the applied electromagnetic field, as it is shown for example in Fig 2.2.(b). Additionally, the dependency of the stiffness matrix term $\mathbf{K}^{\mathrm{BEM}}(\mathbf{x})$ on the position vector $\mathbf{x}$ of the device components originates from the dependency of the boundary matrices $\mathbf{G}(\mathbf{x})$ and $\mathbf{H}(\mathbf{x})$ in (4.9) on the positions of the device components.
The computational cost of performing a simulation using the model (5.1) is in general very high, since calculating the model response to a given input signals requires solving a high order system of nonlinear equations using iterative search strategies as it has

been discussed in the chapter 2.

5.3 Model Order Reduction of Nonlinear Electromagnetic Devices

The high computational cost of simulating the behavior of electromagnetic field using the model (5.1) can be significantly decreased when approximating the high order model (5.1) by a low order one having much lower number of equations. For this purpose, this section is concentrated on developing a new scheme for generating fast and accurate reduced order models of electromagnetic devices starting from their high order nonlinear models (5.1).

Modeling of the components movement will not be considered at this step, and will be considered later on in this section. Therefore, the matrix $\mathbf{K}^{\mathrm{BEM}}$ at this step is considered to be constant.

The trajectory piecewise linear TPWL approach is a very suitable choice for approximating the nonlinearity in the EM field model (5.1) that is caused by the nonlinear behavior of magnetic materials. This is due to its numerous advantages that have been discussed in details in the paragraph 3.2.4. The main concept of the TPWL approach is based on approximating a high order nonlinear system by weighted sum of reduced order linearized models. Therefore, we start this section by performing a linearization of the EM field models (5.1) at a given linearization point.

5.3.1 Linearizing the EM field model

The nonlinear model (5.1) can be linearized at a chosen point $\mathbf{a}_i \in \mathbb{R}^n$ in the state-space by linearizing its nonlinear stiffens function $\mathbf{f}(\mathbf{a}) = \mathbf{K}(\mathbf{a})\mathbf{a}$. If we assume that the function $\mathbf{f}(\mathbf{a}) \in \mathbb{R}^n$ is infinitely differentiable in the neighborhood of $\mathbf{a}_i$, then the function can be expanded as a Taylor series:

$$\mathbf{f}(\mathbf{a}) = \mathbf{K}(\mathbf{a})\mathbf{a} = \mathbf{f}(\mathbf{a}_i) + \left.\frac{d\mathbf{f}(\mathbf{a})}{d\mathbf{a}}\right|_{\mathbf{a}_i} (\mathbf{a} - \mathbf{a}_i) + \sum_{k=2}^{\infty} \frac{\mathbf{f}^{(k)}(\mathbf{a}_i)}{k!} (\mathbf{a} - \mathbf{a}_i)^k \qquad (5.2)$$

where $\mathbf{f}^{(k)}(\mathbf{a}_i)$ denotes the kth derivative of the function $\mathbf{f}^{(k)}(\mathbf{a})$ evaluated at the point $\mathbf{a}_i$, the term $(\mathbf{a}-\mathbf{a}_i)^k$ is the Kronecker product $(\mathbf{a}-\mathbf{a}_i)^k = \overbrace{(\mathbf{a}-\mathbf{a}_i)\otimes\cdots\otimes(\mathbf{a}-\mathbf{a}_i)}^{k \text{ times}}$, and $k\,!$ is the factorial of k.

In the linearization of the function $\mathbf{f}(\mathbf{a})$, only the first two terms in the expansion series (5.2) are considered. The higher order derivatives terms are not taken into account due to their large dimensionality, which makes the computational cost of their calculation and storage very expensive.

By substituting the function $\mathbf{f}(\mathbf{a})$ by its value $\mathbf{K}(\mathbf{a})\mathbf{a}$ in the first two terms in the Taylor series we get:

$$\begin{aligned}\mathbf{f}(\mathbf{a}) = \mathbf{K}(\mathbf{a})\mathbf{a} &\approx \mathbf{K}(\mathbf{a}_i)\mathbf{a}_i + \frac{d}{d\mathbf{a}}\left[\mathbf{K}(\mathbf{a})\mathbf{a}\right]\Big|_{\mathbf{a}_i}(\mathbf{a}-\mathbf{a}_i)\\ &\approx \mathbf{K}(\mathbf{a}_i)\mathbf{a}_i + \left[\frac{d}{d\mathbf{a}}\mathbf{K}(\mathbf{a})\Big|_{\mathbf{a}_i}\mathbf{a}_i + \mathbf{K}(\mathbf{a}_i)\right](\mathbf{a}-\mathbf{a}_i)\\ &\approx \underbrace{\left[\frac{d}{d\mathbf{a}}\mathbf{K}(\mathbf{a})\Big|_{\mathbf{a}_i}\mathbf{a}_i + \mathbf{K}(\mathbf{a}_i)\right]}_{\mathbf{L}_i}\mathbf{a} + \underbrace{\left[-\frac{d}{d\mathbf{a}}\mathbf{K}(\mathbf{a})\Big|_{\mathbf{a}_i}\mathbf{a}_i\right]}_{\mathbf{g}_i}\mathbf{a}_i\end{aligned} \tag{5.3}$$

where the term $\mathbf{L}_i \in \mathbb{R}^{n\times n}$ is the Jacobian matrix of the function $\mathbf{f}(\mathbf{a}) = \mathbf{K}(\mathbf{a})\mathbf{a}$ evaluated at the expansion point $\mathbf{a}_i \in \mathbb{R}^n$:

$$\mathbf{L}_i = \left[\frac{d}{d\mathbf{a}}\mathbf{K}(\mathbf{a})\Big|_{\mathbf{a}_i}\mathbf{a}_i + \mathbf{K}(\mathbf{a}_i)\right] = \mathbf{J}(\mathbf{a}_i) + \mathbf{K}(\mathbf{a}_i) \tag{5.4}$$

and the matrix $\mathbf{J}(\mathbf{a}_i) \in \mathbb{R}^{n\times n}$ is the derivative of the matrix $\mathbf{K}(\mathbf{a})_i$ multiplied by the state-vector $\mathbf{a}_i$:

$$\mathbf{J}(\mathbf{a}_i) = \frac{d}{d\mathbf{a}}\mathbf{K}(\mathbf{a})\Big|_{\mathbf{a}_i}\mathbf{a}_i \tag{5.5}$$

and finally the term $\mathbf{g}_i \in \mathbb{R}^n$ is a vector given by:

$$\mathbf{g}_i = \mathbf{J}(\mathbf{a}_i)\mathbf{a}_i \tag{5.6}$$

After performing the linearization, the nonlinear stiffness function $\mathbf{f}(\mathbf{a})$ can be approximated *locally* in the neighborhood of a linearization point $\mathbf{a}_i$ by:

$$\mathbf{K}(\mathbf{a})\mathbf{a} \approx \mathbf{L}_i\mathbf{a} + \mathbf{g}_i \tag{5.7}$$

and the corresponding linearized electromagnetic field model at $\mathbf{a}_i$ can be written as:

$$\mathbf{C}\dot{\mathbf{a}} + \left[\mathbf{L}_i + \mathbf{K}^{\mathrm{BEM}}\right]\mathbf{a}(t) + \mathbf{g}_i = \mathbf{r}. \tag{5.8}$$

By linearizing the model (5.1) at several linearization points $\{\mathbf{a}_1, \ldots, \mathbf{a}_{s_1}\}$ in its state space, the nonlinear model (5.1) can be approximated by a weighted sum of all the linearized models:

$$\mathbf{C}\dot{\mathbf{a}} + \sum_{i=1}^{s_1} \alpha_i\left(\mathbf{a}\right)\left[\mathbf{L}_i\mathbf{a} + \mathbf{g}_i\right] + \mathbf{K}^{\mathrm{BEM}}\mathbf{a} = \mathbf{r} \tag{5.9}$$

where $\{\alpha_1, \ldots, \alpha_{s_1}\}$ are the weighting coefficients that determines the contribution of each of the linearized models to the overall model (5.9) at each simulation step. The values of the weighting coefficients are calculated in each simulation time step as a function of the distance between the current state vector $\mathbf{a}(t)$ and all the linearization points:

$$(\alpha_1, \ldots, \alpha_{s_1}) = \boldsymbol{\alpha}\big(\mathbf{a}(t), \{\mathbf{a}_1, \ldots \mathbf{a}_{s_1}\}\big) \tag{5.10}$$

The weighting function (5.10) is constructed according to the same scheme that has been presented in the paragraph 3.3.5.

5.3.2 Selecting the linearization points

The selection of the number and the positions of the linearization points has a major influence on the approximation accuracy of the TPWL model (5.9), since the latter model approximates the original nonlinear function $f(\mathbf{a}) = \mathbf{K}(\mathbf{a})\mathbf{a}$ in (5.9) by a weighted sum of the linearized models.

It is clear that increasing the number of linearization points in the TPWL model im-

proves its approximation accuracy. However, the final aim is to generate reduced order models that are as compact as possible. This in turn implies including only few linearized models in (5.9) in order to keep the computational cost that is required for both generating and simulating the TPWL model in acceptable bounds. Moreover, many linearized models (5.8) at different linearization points might be very similar, hence, including such models in the TPWL model (5.9) will only increase the computational costs of its generation without achieving any improvement in its approximation accuracy.

In chapter 3, we have reviewed several algorithms [53, 63] for selecting the linearization points in the TPWL model, and we have discussed their major advantages and limitations. In this paragraph, we present a new algorithm for selecting the number and the location of the linearization points along the simulated training trajectories, with the aim of achieving an optimal trade off between the number of linearized models in the TPWL model (5.9) and its approximation accuracy.

If we assume that the total number of simulation points that are located on the training trajectories is equal to s, the aim of the proposed selection algorithm is to find a minimal number of linearization points $s_1 < s$ in the TPWL model (5.9) while still achieving a very good approximation to the original nonlinear model (5.1).

By taking a closer look to the linearized model (5.9), it can be easily seen that the linearized models at distinguished linearization points can differ only in their corresponding stiffness matrix $\mathbf{L}_i$ (5.4) and the vector $\mathbf{g}_i$ (5.6). The difference in the value of the matrix $\mathbf{L}_i$ (5.4) at two linearization points can be directly traced back to the difference in their corresponding stiffness and Jacobian matrices $\mathbf{K}(\mathbf{a}_i)$, $\mathbf{J}(\mathbf{a}_i)$. Whereas the difference in the value of the vector $\mathbf{g}_i$ (5.6) at two different linearization points can result from a difference in the corresponding $\mathbf{J}(\mathbf{a}_i)$ matrices or due to the difference in the values of two linearization points themselves. However, any significant difference in the linearization point $\mathbf{a}_i$ causes a difference in the matrix $\mathbf{J}(\mathbf{a}_i)$. Therefore, comparing the matrices $\mathbf{K}(\mathbf{a}_i)$ $\mathbf{J}(\mathbf{a}_i)$ at the different linearization points can be used as a base for selecting the linearization points.

In the paragraph 2.7, we have shown that the value of the matrix $\mathbf{K}(\mathbf{a}_i)$ at a linearization points $\mathbf{a}_i$ is directly dependant on the value of the corresponding *magnetic reluctivity* vector $\boldsymbol{\nu}$. Similarly, the value of the $\mathbf{J}(\mathbf{a})$ at a linearization points $(\mathbf{a}_i)$ is directly de-

pendant on the corresponding vector of the *derivative of the magnetic reluctivity* with respect the amplitude of the magnetic induction field $\boldsymbol{d\nu} = \dfrac{d\nu}{d\|B\|}$.
Motivated by the aforementioned facts, it can be concluded that the difference between the linearized models at different linearization points $\mathbf{a}_i$ can be directly found by comparing their corresponding vectors $\boldsymbol{\nu}_i$, $\boldsymbol{d\nu}_i$.

Algorithm 1 Selection algorithm for the linearization points in the TPWL model

1: Given a number of s simulated state-vectors $\{\mathbf{a}_1, \mathbf{a}_2, \ldots, \mathbf{a}_s\}$, and their corresponding *magnetic reluctivity vector* $\{\boldsymbol{\nu}_1, \boldsymbol{\nu}_2, \ldots, \boldsymbol{\nu}_s\}$, and the corresponding vector of *derivative of the magnetic reluctivity* $\{\boldsymbol{d\nu}_1, \boldsymbol{d\nu}_2, \ldots, \boldsymbol{d\nu}_s\}$, assuming that the vectors are ordered according to the Euclidean norm of the magnetic reluctivity vectors i.e. $\{\|\boldsymbol{\nu}_1\| < \|\boldsymbol{\nu}_2\| < \ldots, \|\boldsymbol{\nu}_{s-1}\| < \|\boldsymbol{\nu}_s\|\}$.
2: Initialize the group of selected linearization points with the linearization point $\mathbf{a}_1$ which corresponds to the state in which the device materials have the lowest norm of the magnetic reluctivity (i.e. lowest saturation state), and the linearization point $\mathbf{a}_s$ which corresponds to the state in which the device materials have the highest norm of the magnetic reluctivity (i.e. highest saturation state).
3: **for** $j \leftarrow 2, s-1$ **do**
4: Calculate the Euclidian distances between $\boldsymbol{d\nu}_j$ and all the corresponding $\boldsymbol{d\nu}$ vectors of the selected linearization points.
5: If all the calculated distances are larger than a user defined threshold value τ_1, then add the vectors $\mathbf{a}_j$ to the group of the selected linearization points.
6: **end for**

The proposed selection algorithm selects the linearization points depending on the change in the properties of magnetic materials among the simulated state-vectors. The two vectors $\mathbf{a}_1$ and $\mathbf{a}_s$ are of a high importance for the TPWL approximation, since the first vector $\mathbf{a}_1$ corresponds to the physical state in which the modeled device has the lowest saturation values among all the simulated state-vectors, whereas the second vector $\mathbf{a}_s$ corresponds to the physical state in which the modeled device has the highest saturation values among all the simulated state-vectors.
Besides selecting the two previous vectors, the proposed algorithm selects the linearization points that are accompanied with the most distinguished vectors $\boldsymbol{d\nu}$ of the derivatives of the magnetic reluctivity.

The advantages of the presented selection algorithm are:

1. Its physical interpretability, since it exploits the changes of the material properties – the magnetic reluctivity ν and its derivative $d\nu$ – as selection criteria.

2. The proposed algorithm enables selecting the linearization points before performing model order reduction. This is a major advantage in comparison with the algorithm in [63], in which the reduced order linearized models are compared in order to determine the linearization points that will be selected. Consequently, the selected linearization points in [63] can vary depending on the applied model order reduction approach, and depending on the order of the reduced order models.

3. The algorithm presented in [63] requires performing a model linearization and order reduction of the linearized model at all simulated state-vectors. In contrast, our proposed algorithm requires performing model linearization and order reduction at only the selected linearization points. This advantage produces a significant saving in the computational cost that is required for the generating the reduced order model.

4. The proposed algorithm can be used for selecting the linearization points *on the fly* during the simulation of the full order nonlinear model. This can be done by initializing the group of selected linearization points (step 2 in the algorithm 1) with the first simulated state-vector, and applying the steps $3 \rightarrow 5$ of the algorithm 1 during the simulation.

5. The presented algorithm can be applied to other physical modeling domains by replacing the magnetic reluctivity and its derivative by other materials property vectors, such as the thermal conductivity and its derivative with respect to the temperature in the nonlinear thermal modeling field.

5.3.3 Numerical example

In order to demonstrate the performance of the presented algorithm for selecting the linearization points in the TPWL model, we apply it to a numerical modeling example.

The task in this example to generate a fast and accurate reduced order model of the electromagnetic valve shown in Fig. 5.1.

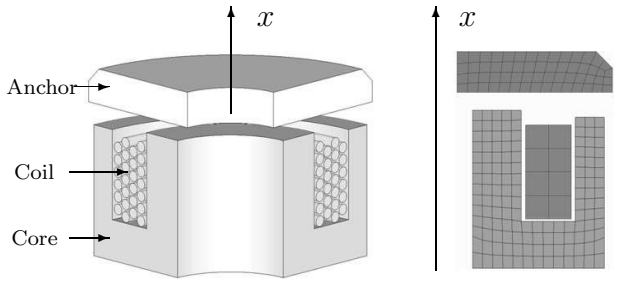

Figure 5.1: A simple electromagnetic device consisting of: a magnetic core, a moving anchor, a coil, and a mechanical spring (not shown in the figure). The 3D model (left) is shown for illustration purposes, whereas the spatially discretized 2D axis-symmetric model (right) is used for the device simulation.

The device consists mainly of a coil, a core, and an anchor. The core and the anchors are assumed to be made of materials having nonlinear magnetic properties (shown in Fig. 2.2).(b). The coil is assumed to be made of copper, which have linear magnetic properties (i.e ν is constant).

The device is modeled using a two dimensional axis-symmetric model and spatially discretized using the coupled BEM-FEM method. The spatial discretization resulted in a system of nonlinear differential algebraic equations DAEs (2.13) of order $n = 837$. The algebraic part is removed by elimination according to (4.7) producing a system of nonlinear ordinary differential equations (5.1) of order $n = 629$.

The anchor is separated from the magnetic core using a mechanical spring that tries to keep the anchor away from the core. However, at this step, the anchor is considered to be fixed at the initial position $x_0 = 0$ since the movement of the device components is not considered yet.

The vector $\mathbf{r}(t)$ in the model (5.1) contains in general the contributions of the electromagnetic field sources. In this example, we assume that the excitation coil is connected to a voltage source $u(t)$, therefore, based on (2.25), the input signal $\mathbf{r}(t)$ can be expressed

as:

$$\mathbf{r} = -\frac{\mathbf{b}\mathbf{b}^T}{R}\dot{\mathbf{a}} + \frac{\mathbf{b}}{R}u \tag{5.11}$$

where the vector $\mathbf{b} \in \mathbb{R}^n$ describes the distribution of the impressed current in the excitation coil region and R is the Ohmic resistance of the excitation coil. By replacing the value of the excitation vector $\mathbf{r}(t)$ in the model equation (5.1) we get:

$$\left[\mathbf{C} + \frac{\mathbf{b}\mathbf{b}^T}{R}\right]\dot{\mathbf{a}} + \left[\mathbf{K}(\mathbf{a}) + \mathbf{K}^{\mathrm{BEM}}\right]\mathbf{a} = \frac{\mathbf{b}}{R}u \tag{5.12}$$

The high order nonlinear model (5.12) can be approximated by a TPWL model of the same order as follows:

$$\left[\mathbf{C} + \frac{\mathbf{b}\mathbf{b}^T}{R}\right]\dot{\mathbf{a}} + \sum_{i=1}^{s_1}\alpha_i(\mathbf{a})\left[\mathbf{L}_i\mathbf{a} + \mathbf{g}_i\right] + \mathbf{K}^{\mathrm{BEM}}\mathbf{a} = \frac{\mathbf{b}}{R}u \tag{5.13}$$

The output output signal considered in this paragraph is electromagnetic force acting on the anchor (2.31).

Four simulation runs have been performed using both the high order nonlinear model (5.12) and the high order TPWL model (5.13). The order of the model (5.13) is deliberately not reduced at this step, in order to illustrate the effect of selecting the linearization points on the approximation accuracy of the TPWL model without invoking an additional approximation error due to the order reduction.

In all the four simulation runs, the simulation step size was chosen to be $\Delta t = 5\mu$s, and the number of simulation steps per run is set to 400. The aforementioned settings of the have been applied to both models (5.12) ,(5.13).

The four voltage excitation signals that have been used in the four simulation runs together with the resulting electromagnetic forces are shown in Fig. (5.2). Due to the limited editorial space, the results of the four simulation runs are shown on the same time axis.

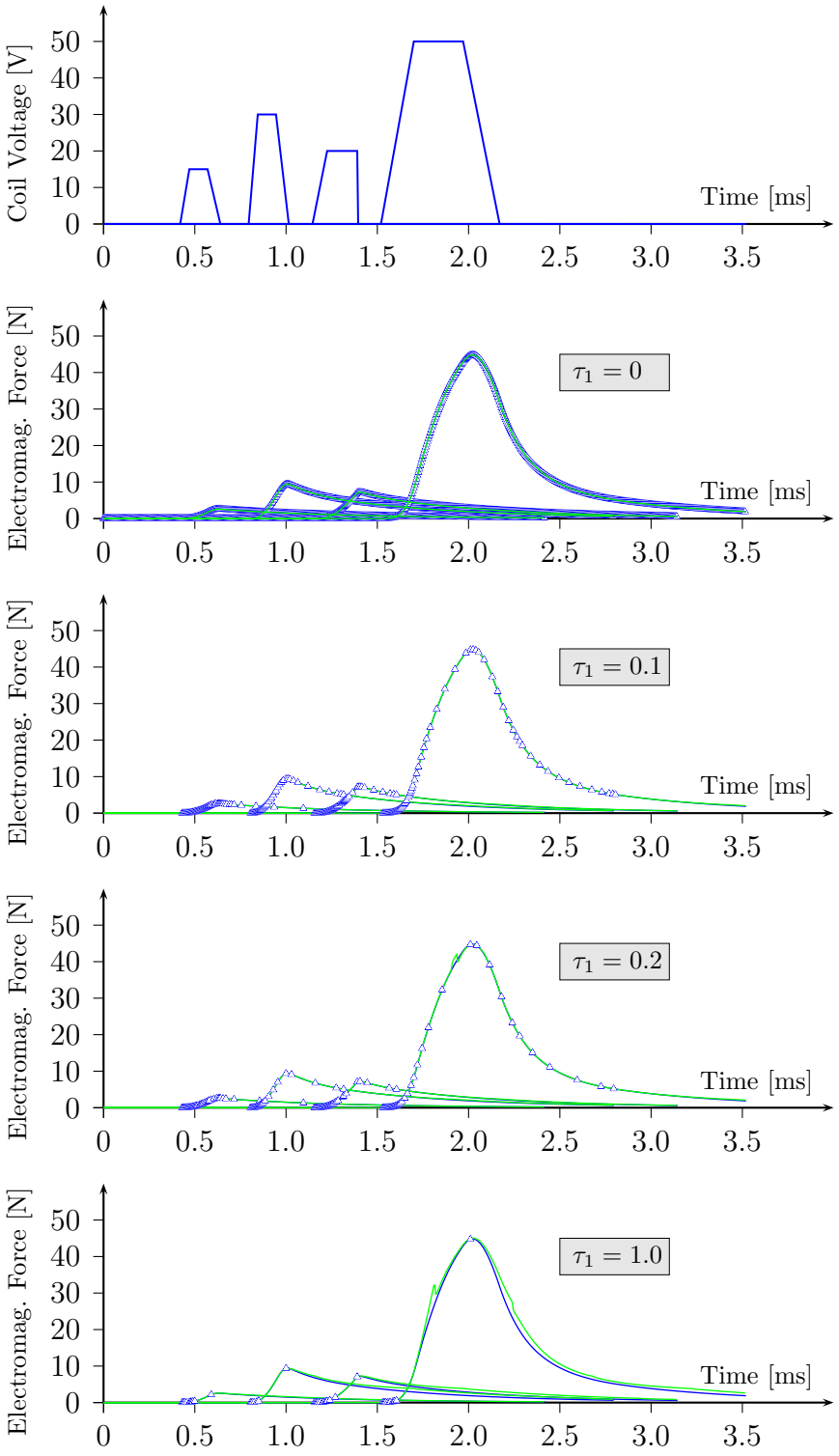

Figure 5.2: A figure illustrating the approximation accuracy of the full order TPWL model (green solid line) in comparison to the full order nonlinear model (blue solid line) using different settings of the linearization points selection parameter τ_1. The triangular markers indicates the position of the selected linearization points

The algorithm 1 is applied to select a group of linearization points in the TPWL approximation model (5.13) from the total number of 1600 simulated state-vectors. Different values of the selection parameters $\tau_1 = 0, 0.1, 0.2, 1.0$ have been applied. This resulted in a number of selected linearization points equals to 1600, 288 , 198, 90 respectively. The positions of the selected linearization points are marked with the triangular markers in Fig. 5.2.

All the simulation results shows that the full order TPWL approximation model (5.13) achieves a good approximation of the original nonlinear model (5.12). Moreover, the simulation results show that the proposed linearization points selection algorithm has succeeded in reducing the number of linearization points in the model (5.13) from 1600 possible points to $s_1 = 288$ points by setting the selection parameters $\tau_1 = 0.1$, and to reduce it further to $s_1 = 198$ with $\tau_1 = 0.2$ while maintaining a very good approximation accuracy. Increasing the selection parameter $\tau_1 = 1.0$ reduces the number of selected linearization points further $s_1 = 90$, however, the approximation accuracy starts to degrade.

For the purpose of graphical illustration, the derivative vectors of the magnetic reluctivity $\boldsymbol{d\nu}$ are shown in Fig. 5.3 at three selected linearization points.

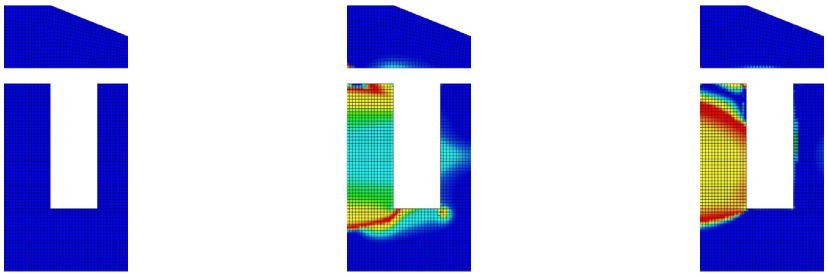

(a) (b) (c)

Figure 5.3: Figure(a) illustrates the *derivative of the magnetic reluctivity* $\boldsymbol{d\nu}$ at the physical state in which the modeled materials device have the lowest saturation values among all the simulated state-vectors. Figure (b) illustrates $\boldsymbol{d\nu}$ at the physical state in which the modeled device materials have the highest saturation values among all the simulated state-vectors. Figure (c) illustrates $\boldsymbol{d\nu}$ at one of the selected linearization points.

5.3.4 Reducing the order of the TPWL model

After selecting the linearization points in the TPWL model (5.9), the order of all the linearized models has to be reduced. For this purpose, several model order reduction approaches can be exploited as has been discussed in the paragraph 3.3.4.
In this work, the proper orthogonal decomposition POD approach, that has been reviewed in the paragraph 3.1.4, is exploited for reducing the order of all the linearized models in the TPWL model (5.9). The choice of the POD reduction approach is motivated by:

1. Its ability to reduce the order of both nonlinear dynamic systems. This feature is of a high importance to our work since the model describing the input/output behavior of the electromagnetic field remains nonlinear due to the quadratic dependency of the output signals such as electromagnetic forces (2.31) and torques (2.33) on the state-vector of the TPWL model (5.9).

2. Its cheap computational costs in comparison with the approach proposed in [53] which requires generating Krylov based subspace at each linearized model in the TPWL model (5.9).

3. Its straight forward applicability to reduce the order of parametric models of electromagnetic devices as it will be shown in chapter 6.

When applying the proper orthogonal decomposition approach to reduce the order of electromagnetic field models, it approximates the state-vector of the electromagnetic field model by a linear combination of a low number q of optimally chosen virtual state-vectors. Those vectors are assembled column-wise in the projection matrix $\mathbf{V} \in \mathbb{R}^{n \times q}$.
The procedure of generating a reduction subspace using the POD approach starts by assembling all the simulated state-vectors of the high order nonlinear EM field model (5.1) in the so called snapshots matrix $\mathbf{X} = [\mathbf{a}_1, \mathbf{a}_2, \ldots, \mathbf{a}_s] \in \mathbb{R}^{n \times s}$. Then, the POD algorithm is applied to find the best low rank approximation of all the vector in the

snapshot matrix $\mathbf{X}$ in the sense of the Frobenius error norm:

$$\min \|\mathbf{E}\|_F = \min \|\mathbf{X} - \mathbf{V}\mathbf{X}_\mathbf{r}\|_F = \left(\sum_{i=q+1}^{\text{rank X}} \sigma_i^2(\mathbf{X}) \right)^{1/2} \tag{5.14}$$

assuming that $\sigma_q > \sigma_{q+1}$

with σ_i being the i^{th} singular value of the matrix $\mathbf{X}$, and $\mathbf{X}_r = [\mathbf{a}_{r1}, \mathbf{a}_{r2}, \ldots, \mathbf{a}_{rs}] \in \mathbb{R}^{q \times s}$ is the reduced order snapshots matrix.
Now, if we consider for example the voltage driven TPWL model (5.13), the order of all the linearized models can be reduced by projecting them onto the subspace spanned by the columns of the matrix $\mathbf{V}$ according the Galerkin projection approach (reviewed in paragraph 3.1.1). Consequently, the reduced order TPWL model can be written as:

$$\left[\mathbf{C}_r + \frac{\mathbf{b}_r \mathbf{b}_r^T}{R} \right] \dot{\mathbf{a}}_r + \sum_{i=1}^{s_1} \alpha_i \left(\mathbf{a}_r \right) \left[\mathbf{L}_{ri} \mathbf{a}_r + \mathbf{g}_{ri} \right] + \mathbf{K}_r^{\text{BEM}} \mathbf{a}_r = \frac{\mathbf{b}_r}{R} u \tag{5.15}$$

and the order of the output equation (2.31) for calculating the electromagnetic force is reduced to :

$$\mathbf{f}_{\text{mag}} = \mathbf{a}_r^T \mathbf{R}_r \mathbf{a}_r \tag{5.16}$$

and the order of the equation (2.24) for calculating the current flowing in the excitation coil can be reduced to:

$$i = \frac{u}{R} - \frac{\mathbf{b}^T}{R} \dot{\mathbf{a}}_r \tag{5.17}$$

where $\mathbf{a}_r \in \mathbb{R}^q$ is the reduced order state-vector which has much lower number of variables than state-vector $\mathbf{a} \in \mathbb{R}^n$ of the original model (5.13). The reduced order matrices and vectors of the TPWL model (5.15) are given by:
$\mathbf{C}_r = \mathbf{V^T C V}$, $\mathbf{L}_{ri} = \mathbf{V^T L}_i \mathbf{V}$, $\mathbf{K}_r^{\text{BEM}} = \mathbf{V^T K}^{\text{BEM}} \mathbf{V}$, $\mathbf{g}_{ri} = \mathbf{V^T g}_i$, $\mathbf{b}_r = \mathbf{V^T b}$,
$\mathbf{R}_r = \mathbf{V^T R V}$.

5.3.5 Numerical example

In this example, a reduced order TPWL model of the electromagnetic valve that has been presented in the paragraph 5.3.3 is generated. For this purpose, four distinguished input voltage signals (solid lines in Fig. 5.5) are applied to the nonlinear EM field model (5.12) for generating the *training trajectories*. Additionally, in order to evaluate the performance of the generated reduced order EM field model away from the training trajectories, four different voltage input signals (dashed lines in Fig. 5.5) are applied to the nonlinear EM field model (5.12) for generating the *validation trajectories*. In all simulation runs, the simulation step size was chosen to be $\Delta t = 5\mu$s, and the number of simulation steps per run is set to 400. The aforementioned settings have been applied later on to the reduced order model.
The high order nonlinear EM field model (5.12) is linearized at a number $s_1 = 198$ of linearization points along the *training trajectories*. The number and the positions of the linearization points is determined using the proposed selection algorithm with $\tau_1 = 0.2$.

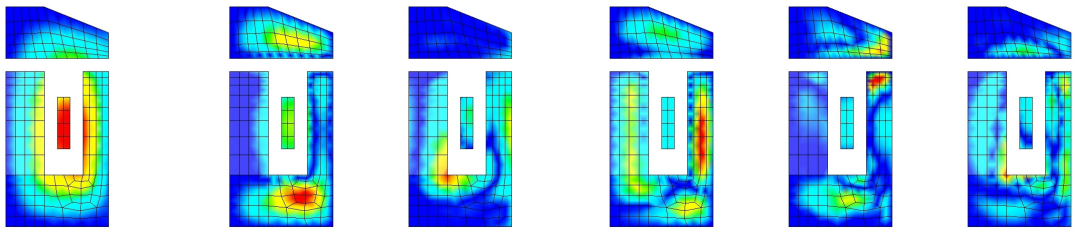

(a) (b) (c) (d) (e) (f)

Figure 5.4: The figures (a)-(f) illustrate respectively the magnetic vector potential field that correspond to the first six vectors in the projection matrix $\mathbf{V}$.

The order of the resulting TPWL model (5.13) is reduced from the order $n = 629$ to the order $n = 10$ using the POD approach. The 1600 simulated state-vectors along the four training trajectories are approximated using the POD approach by a linear combination of columns of a projection matrix containing ten vectors $\mathbf{V} \in \mathbb{R}^{629\times 10}$. The magnetic vector potential fields that corresponds to the first six vectors in the projection matrix $\mathbf{V}$ are shown in Fig. 5.4.

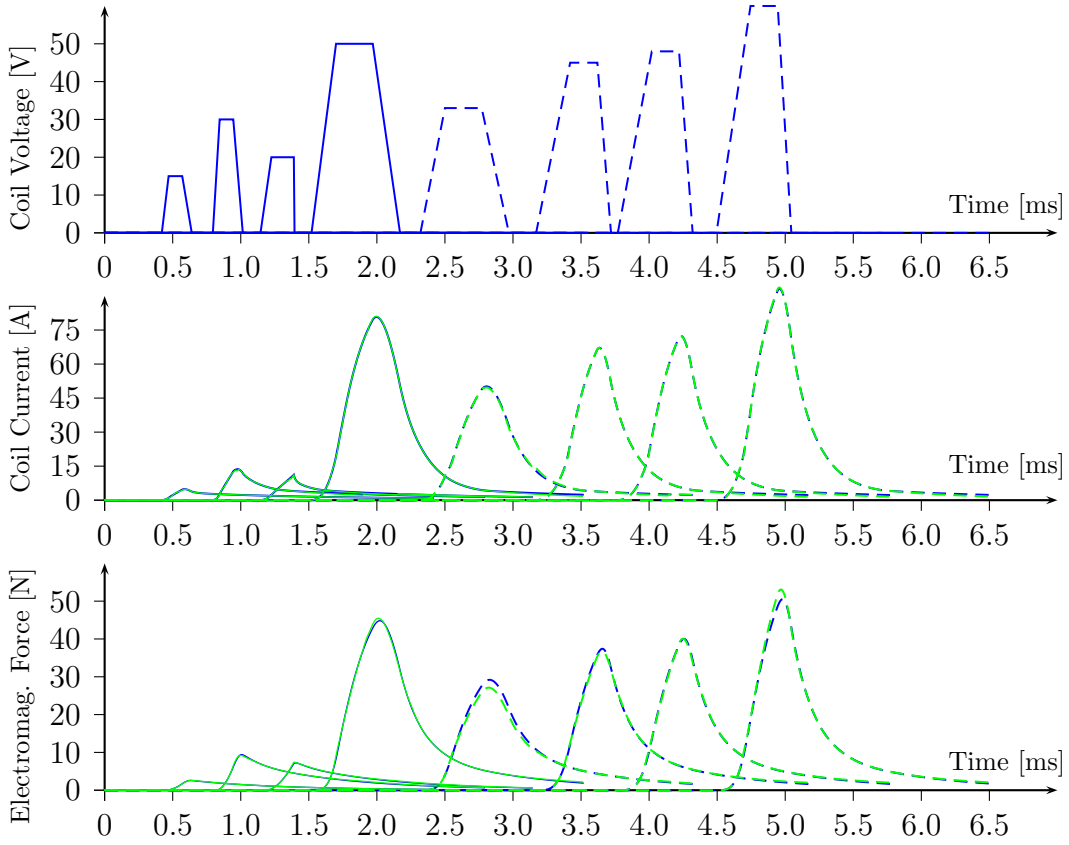

Figure 5.5: Comparing the simulation results of an electromagnetic valve using a nonlinear EM field model of order $n = 629$ (blue lines) versus a reduced order EM field model of order $n = 10$ (green lines). The solid lines represent the input/output signals of the *training trajectories*. Whereas, the dashed lines represent the input/output signals of the *validation trajectories*.

The projection matrix $\mathbf{V}$ is used to reduce the order of the high order TPWL model (5.13) and the order of the output equations that calculate the EM force on the anchor (2.31) and the current in the excitation coil (2.24).

The response of the electromagnetic valve to the eight voltage input signals in Fig. 5.5 is simulated using the reduced order TPWL model (5.15) and the reduced order output equations (5.16), (5.17). The simulation results in Fig. 5.5 show an excellent matching between the results achieved using the nonlinear EM field model $n = 629$ and the ones achieved using the reduced order TPWL model $n = 10$ at almost all the training and validation trajectories. A slight difference in the resulting electromagnetic force is noticed in some of the validation trajectories. This deviation indicates that

the original nonlinear model (5.12) shows a nonlinear behavior along the validation trajectories which can not be well approximated as a weighted sum of the reduced order linearized models in (5.15). However, this small deviation can be easily alleviated – if required – by expanding the group of s_1 linearized models in the TPWL model (5.15) with few additional linearized models (5.8) along the new validation trajectories.
It is worth mentioning that in all the eight simulation runs, the simulation using the reduced order model (5.15) was almost $40 - 50$ times faster in the required simulation time than the full order nonlinear model (5.12) as it is shown in the Table 5.1.

Excitation Signal	Simulation Time (sec)	
	Full Order Nonlinear Model $n = 629$	Reduced Order TPWL Model $n = 10$
1	40.0	1.37
2	40.3	1.36
3	48.0	1.36
4	64.6	1.35
5	62.3	1.36
6	63.5	1.35
7	64.8	1.37
8	68.9	1.37

Table 5.1: The simulation time of a full order nonlinear model $n = 629$ versus the simulation time of a reduced order model $n = 10$

5.4 Considering Components Movement

Electromagnetic devices that contain moving components are very wide spread in modern industrial applications. Such devices include among others rotating electrical machines, electromagnetic valves, electromagnetic solenoids, and electromechanical relays. Despite the importance of this class, the issue of considering the movement of the electromagnetic device components in the generation of their reduced order models has not been addressed so far according to our best knowledge. In our work [2], we presented a new approach that enables considering the effect of the components movement on the

reduced order models of electromagnetic devices. In the following paragraphs, the aforementioned approach is detailed, and its performance is analyzed using several numerical examples.

In general, the movement of EM device components can be caused by the induced electromagnetic forces, or by any other types of applied forces. When one or more of the device component moves, the corresponding EM field model has to be adapted according to the new relative positions of device components. This adaptation in BEM-FEM method implies updating the values of the boundary matrices $\mathbf{G}$ and $\mathbf{H}$ [33, 55], since both matrices describe the mutual influence among the state-variables that are located on the surfaces of the device components, which is directly affected by the components movement as it can be graphically seen in Fig. 5.6.

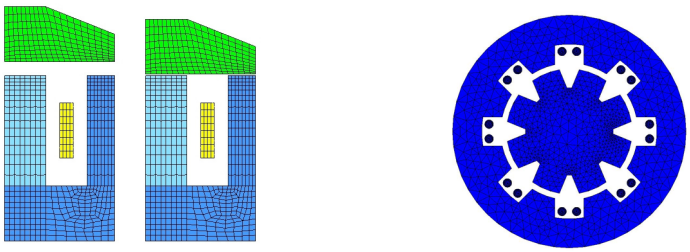

(a) (b)

Figure 5.6: The movement of the device components leads to a change in the mutual influence among the nodes that are located on the components' surfaces.

The dependency of the $\mathbf{G}$ and $\mathbf{H}$ matrices on the components positions causes a similar dependency in the matrix $\mathbf{K}^{\mathrm{BEM}}(\mathbf{x}) = \mathbf{G}^{-1}(\mathbf{x})\mathbf{H}(\mathbf{x})$ in the EM field model (5.1), and in the matrices $\mathbf{R}(\mathbf{x})$ and $\mathbf{S}(\mathbf{x})$ that are used for calculating the electromagnetic forces (2.31) and torques (2.33) respectively. The term $\mathbf{K}^{\mathrm{BEM}}(\mathbf{x})$ in the nonlinear EM field model (5.1) is considered as an additional source of nonlinearity. However, in contrast to conventional nonlinearities, the term $\mathbf{K}^{\mathrm{BEM}}$ is not dependant on the state-vector of the nonlinear model (5.1) itself, but on the state-vector $\mathbf{x}$ of the weakly coupled mechanical equations (2.8).

In most industrial applications, the movement of device components is restricted to a translation along a predefined movement trajectory as it is the case in electromagnetic

valves shown in Fig. 5.6(a), or restricted to rotation around a predefined axis as it is the case in rotating electrical machines. Therefore, if the position dependant matrices $\mathbf{K}^{\mathrm{BEM}}(\mathbf{x})$, $\mathbf{R}(\mathbf{x})$, and $\mathbf{S}(\mathbf{x})$ are sampled at several points $\{\mathbf{x}_1, \ldots, \mathbf{x}_{s_2}\}$ along the known *movement trajectories* of the design components, then the boundary matrix in the nonlinear model (5.1) can be approximated as a weighted sum of all the sampled matrices:

$$\mathbf{K}^{\mathrm{BEM}}(\mathbf{x}) = \sum_{j=1}^{s_2} \beta_j(\mathbf{x}) \mathbf{K}_j^{\mathrm{BEM}} \tag{5.18}$$

Similarly, the matrices that are used for calculating electromagnetic forces f_{mag} (2.31) and electromagnetic torques τ_{mag}(2.33) can be approximated as:

$$\mathbf{R}(\mathbf{x}) = \sum_{j=1}^{s_2} \beta_j(\mathbf{x}) \mathbf{R}_j \tag{5.19}$$

$$\mathbf{S}(\mathbf{x}) = \sum_{j=1}^{s_2} \beta_j(\mathbf{x}) \mathbf{S}_j \tag{5.20}$$

the weighting function $\boldsymbol{\beta}$ should be constructed in such a way that it gives a higher weighting value β_j for the position dependent matrices $\mathbf{K}_j^{\mathrm{BEM}}, \mathbf{R}_j, \mathbf{S}_j$ when the position vector $\mathbf{x}(t)$ approaches their corresponding sampled position point $\mathbf{x}_j$ during the simulation run.

Based on the approximations (5.18)-(5.20), the high order nonlinear electromagnetic field model (5.1) can be approximated by:

$$\mathbf{C}\dot{\mathbf{a}} + \sum_{i=1}^{s_1} \alpha_i(\mathbf{a})[\mathbf{g}_i + \mathbf{L}_i\mathbf{a}] + \sum_{j=1}^{s_2} \beta_j(\mathbf{x}) \mathbf{K}_j^{\mathrm{BEM}}\, \mathbf{a} = \mathbf{r}(t) \tag{5.21}$$

$$f_{\mathrm{mag}} = \mathbf{a}^{\mathbf{T}} \left[\sum_{j=1}^{s_2} \beta_j(\mathbf{x}) \mathbf{R}_j \right] \mathbf{a} \tag{5.22}$$

$$\tau_{\text{mag}} = \mathbf{a}^{\mathbf{T}} \left[\sum_{j=1}^{s_2} \beta_j(\mathbf{x}) \mathbf{S}_j \right] \mathbf{a} \tag{5.23}$$

$$(\alpha_1, \ldots, \alpha_{s_1}) = \boldsymbol{\alpha}\big(\mathbf{a}, \{\mathbf{a}_1, \ldots \mathbf{a}_{s_1}\}\big) \tag{5.24}$$

$$(\beta_1, \ldots, \beta_{s_2}) = \boldsymbol{\beta}\big(\mathbf{x}, \{\mathbf{x}_1, \ldots \mathbf{x}_{s_2}\}\big) \tag{5.25}$$

$$\sum_{i=1}^{s_1} \alpha_i = 1 \qquad \sum_{j=1}^{s_2} \beta_j = 1$$

The position vector $\mathbf{x}(t)$ of the device components can be calculated at each simulation time step by solving the mechanical equations (2.8).

5.4.1 Selecting the sampling points of the position dependant matrices

Selecting the number and the positions of the sampling points of the matrices $\mathbf{K}^{\text{BEM}}(\mathbf{x})$, $\mathbf{R}(\mathbf{x})$, and $\mathbf{S}(\mathbf{x})$ has a significant influence on the approximation accuracy of the model (5.21)-(5.23). Including a large number s_2 of the aforementioned sampling points in the model (5.21)-(5.23) improves its approximation accuracy, however it increases the computational cost for its generation, since creating the matrix $\mathbf{K}^{\text{BEM}}(\mathbf{x})$, $\mathbf{R}(\mathbf{x})$, and $\mathbf{S}(\mathbf{x})$ at each sampling point requires inverting the fully occupied $\mathbf{G}(\mathbf{x})$ matrix according to (4.9).

However, the *possible movement paths* of the device components are known in advance in almost all industrial EM device. Therefore, it is a suitable choice to sample the position dependant matrices uniformly along those movement paths. The choice of the number s_2 of sampling points is can be easily done by increasing it successively until the required approximation accuracy is reached. The effect of varying the parameter s_2 on the approximation accuracy of the reduced order EM device model is demonstrated on a numerical example later on in this chapter (Fig. 5.8).

One should note that electromagnetic devices that have components with complex geometrical surfaces such as electrical machines Fig. (5.6).(b) requires a higher number s_2 of sampling points in order to achieve a good approximation accuracy. In contrast,

devices with components having simple surfaces such as the EM valve in (5.6)(a) can be well approximated using a small number s_2 of sampling points.
It is worth mentioning that the suitable choice of the interpolation function $\boldsymbol{\beta}$ could theoretically help reducing the required number s_2 of sampling point. However, some weighting functions might fit some devices geometries better than others, and it is not trivial to find a universally optimal weighting function. Therefore, in this work, the same weighting function (paragraph 3.3.5) that is used for interpolating the linearized models in (5.21) is used for interpolating the position dependant matrices.

5.4.2 Model order reduction

The order of the approximation model (5.21)-(5.22) can be reduced using the proper orthogonal decomposition approach. The reduction procedure starts with filling the snapshots matrix with the simulated state-vectors of the high order nonlinear EM field model (5.1). The latter state-vectors are generated from the coupled simulation of the nonlinear EM field model (5.1) with the mechanical equations (2.8). In the next step, all the simulated state-vectors are approximated with a linear combination of the vectors of a projection matrix $\mathbf{V} \in \mathbb{R}^{n \times q}$ that is generated by the POD approach. The projection matrix $\mathbf{V}$ is used to reduce the order of all the matrices and vectors in the approximation model (5.21) using the Galerkin projection (paragraph 3.1.1). Consequently, the final reduced order electromagnetic field model can be written as:

$$\mathbf{C}_r \dot{\mathbf{a}}_r + \sum_{i=1}^{s_1} \alpha_i(\mathbf{a}_r)[\mathbf{g}_{ri} + \mathbf{L}_{ri}\mathbf{a}_r] + \sum_{j=1}^{s_2} \beta_j(\mathbf{x})\mathbf{K}_{rj}^{\mathrm{BEM}}\, \mathbf{a}_r = \mathbf{r}_r \tag{5.26}$$

$$f_{\mathrm{mag}} = \mathbf{a}_r^T \left[\sum_{j=1}^{s_2} \beta_j(\mathbf{x})\mathbf{R}_{rj} \right] \mathbf{a}_r \tag{5.27}$$

$$\tau_{\mathrm{mag}} = \mathbf{a}_r^T \left[\sum_{j=1}^{s_2} \beta_j(\mathbf{x})\mathbf{S}_{rj} \right] \mathbf{a}_r \tag{5.28}$$

where $\mathbf{a} \approx \mathbf{V}\mathbf{a}_r$, $\mathbf{a} \in \mathbb{R}^n$, $\mathbf{a}_r \in \mathbb{R}^q$, and $q \ll n$. The matrices and vectors of the reduced order model are given by:
$\mathbf{C}_r = \mathbf{V}^\mathbf{T}\mathbf{C}\mathbf{V}$, $\mathbf{L}_{ri} = \mathbf{V}^\mathbf{T}\mathbf{L}_i\mathbf{V}$, $\mathbf{K}_{rj}^{\mathrm{BEM}} = \mathbf{V}^\mathbf{T}\mathbf{K}_j^{\mathrm{BEM}}\mathbf{V}$, $\mathbf{g}_{ri} = \mathbf{V}^\mathbf{T}\mathbf{g}_i$, $\mathbf{r}_r = \mathbf{V}^\mathbf{T}\mathbf{r}$,
$\mathbf{R}_{rj} = \mathbf{V}^\mathbf{T}\mathbf{R}_j\mathbf{V}$, $\mathbf{S}_{rj} = \mathbf{V}^\mathbf{T}\mathbf{S}_j\mathbf{V}$.
The final reduced order model of the electromagnetic field (5.21), -(5.28) is of order q (i.e. having q variables in its state-vector $\mathbf{a}_r$) which is much lower than the order n of the original model (5.1),(2.31),(2.33). Therefore, it offers a significant reduction in the required simulation time and computational resources.
Separating the approximation of the position dependent terms $\mathbf{K}^{\mathrm{BEM}}$, $\mathbf{R}$, and $\mathbf{S}$ from the apprximation of the EM field dependent term $\mathbf{L}, \mathbf{g}$ in the model (5.26)-(5.28) allows the user to control the approximation accuracy of both types of nonlinearities independently. Moreover, the reduced order EM field model (5.26)-(5.28) can be coupled to any parametric mechanical model that simulates the components movement. This in turns makes the overall coupled electromagnetic-mechanical models parametric, and therefore enables exploiting it in performing a design optimization of electromechanical devices as it will be shown later on in this chapter.
The simulation cycle of the overall reduced order device model can be performed according to the following algorithm:

Algorithm 2 Simulating the reduced order models of electromagnetic devices

1: define initial conditions $\mathbf{a}_r^0 = \mathbf{V}^T\mathbf{a}^0$, $\mathbf{x}^0$, $\dot{\mathbf{x}}^0$
2: define a simulation time vector $\left[t^1, t^2, \ldots, t^N\right]$
3: set $i = 0$
4: set $\mathbf{a}_r^i = \mathbf{a}_r^0$, $\mathbf{x}^i = \mathbf{x}^0$, $\dot{\mathbf{x}}^i = \dot{\mathbf{x}}^0$
5: **for** $i \leftarrow 0, N-1$ **do**
6: Calculate the weighting coefficients $(\alpha_1, \ldots, \alpha_{s_1}) = \boldsymbol{\alpha}\big(\mathbf{a}_r^i, \{\mathbf{a}_{r1}, \ldots \mathbf{a}_{rs_1}\}\big)$ at the reduce order state-vector $\mathbf{a}_r^i$
7: Calculate the weighting coefficients $(\beta_1, \ldots, \beta_{s_2}) = \boldsymbol{\beta}\big(\mathbf{x}^i, \{\mathbf{x}_1, \ldots \mathbf{x}_{s_2}\}\big)$ at the position $\mathbf{x}^i$
8: Simulate the reduced order EM field model (5.26) in the time span $[t^i, t^{i+1}]$ to find $\mathbf{a}_r^{i+1}$
9: Calculate f_{mag}^{i+1} using (5.27) and/or $\tau_{\mathrm{mag}}^{i+1}$ using (5.28)
10: Simulate the mechanical equations in the time span $[t^i, t^{i+1}]$ to find $\mathbf{x}^{i+1}$, $\dot{\mathbf{x}}^{i+1}$
11: set $i = i + 1$, $\mathbf{a}_r^i = \mathbf{a}_r^{i+1}$, $\mathbf{x}^i = \mathbf{x}^{i+1}$, $\dot{\mathbf{x}}^i = \dot{\mathbf{x}}^{i+1}$
12: **end for**

5.4.3 Numerical example

In this paragraph, we apply the new developed method to the generation of a reduced order model of an industrial electromagnetic device with a moving component and materials with nonlinear magnetic properties. For this purpose, the electromagnetic valve which was presented in the paragraph 5.3.3 is considered. The anchor and the core of the electromagnetic valve are made of a material with nonlinear magnetic properties. The valve's anchor is able to move towards the core under the effect of the induced electromagnetic force. The latter movement is restricted to a one dimensional translation along the x-axis. The mechanical bumps at the end of both movement directions limit the anchors movement to the range $x \in [0, 400]\mu$m. The anchor is separated from the core by a mechanical spring that tries to keep the anchor away from the core. The spring is pre-tensioned, therefore, it produces a force $f_s(x_0) = 4$ N at the initial position $x_0 = 0$. The spring force is given at any position point $x \in [0, 400]\mu$m by the linear relation $f_s = f_s(x_0) + kx$, where $k = 10$ KN/m is the stiffness constant of the spring. Accordingly, the mechanical equation that describes the anchor movement can be written as:

$$m\ddot{x} + kx = f_{\text{mag}} - f(x_0) \tag{5.29}$$

where $m = 12$g is mass of the moving anchor and no damping parameter is considered in the mechanical equation .

The generation process of the reduced order electromagnetic field model starts by generating the *training trajectories*. For this purpose, four voltage excitation signals are applied to the terminals of the excitation coil in the device model. Those signals are illustrated in the blue solid lines in Fig. 5.7. Consequently, four simulation runs are performed using the high order nonlinear EM field model (5.1) coupled to the mechanical equations (5.29). The input vector $\mathbf{r}(t)$ in the EM field model (5.1) is evaluated using (2.25). The simulation step size is chosen to be $\Delta t = 5\mu$s, and the number of simulation steps per run is set to 700. The aforementioned settings of the have been applied later on to the reduced order model.

Due to the limited editorial space, the input/output signals for both the training and validation trajectories are plotted on the time axis.

The EM force acting on the moving anchor is evaluated using the quadratic function (2.31), and the coil current is calculated using the relation (2.24). The position of the moving anchor and its velocity can be calculated from the solution of the mechanical equations (5.29).

After generating the *training trajectories*, the number and the positions of the linearization points are chosen from all the simulated 2800 state-vectors along the *training trajectories* using our proposed selection algorithm with $\tau_1 = 0.02$. This has resulted in selecting a total number of $s_1 = 497$ linearization points. The high order nonlinear model (5.1) is linearized according to (5.8) at all the selected linearization points.

The position dependent matrices $\mathbf{K}^{\mathrm{BEM}}(\mathbf{x})$ and $\mathbf{R}(\mathbf{x})$ are sampled at $s_2 = 20$ uniformly distributed position points along the anchor movement path $[0 - 400\mu\mathrm{m}]$.

The 2800 simulated state-vectors along the *training trajectories* are assembled in snapshots matrix and a projection matrix $\mathbf{V} \in \mathbb{R}^{629\times 40}$ containing $q = 40$ vectors is generated using the proper orthogonal decomposition approach POD.

The matrix $\mathbf{V}$ has been used to reduce the order of all the matrices and vectors in the approximation model (5.21) and the output equations (5.22) , (2.24) resulting in the final reduced order electromagnetic field model:

$$\begin{cases} \left[\mathbf{C}_r + \dfrac{\mathbf{b}_r\mathbf{b}_r^T}{R}\right]\dot{\mathbf{a}}_r + \displaystyle\sum_{i=1}^{s_1}\alpha_i\left(\mathbf{a}_r\right)\left[\mathbf{L}_{ri}\mathbf{a}_r + \mathbf{g}_{ri}\right] + \sum_{j=1}^{s_2}\beta_j(\mathbf{x})\mathbf{K}_{rj}^{\mathrm{BEM}}\,\mathbf{a}_r = \dfrac{\mathbf{b}_r}{R}u \\ f_{\mathrm{mag}} = \mathbf{a}_r^T\left[\displaystyle\sum_{j=1}^{s_2}\beta_j(\mathbf{x})\mathbf{R}_{rj}\right]\mathbf{a}_r \\ i = \dfrac{u}{R} - \dfrac{\mathbf{b}^T}{R}\dot{\mathbf{a}}_r \end{cases} \tag{5.30}$$

The electromagnetic valve is simulated using the reduced order EM field model (5.30) coupled to the mechanical equation (5.29) by applying the same excitation signals that have been used for generating the training trajectories.

The simulation results in Fig. 5.7 show an excellent matching between the results achieved using the full order and the reduced order models considering all the four considered system outputs.

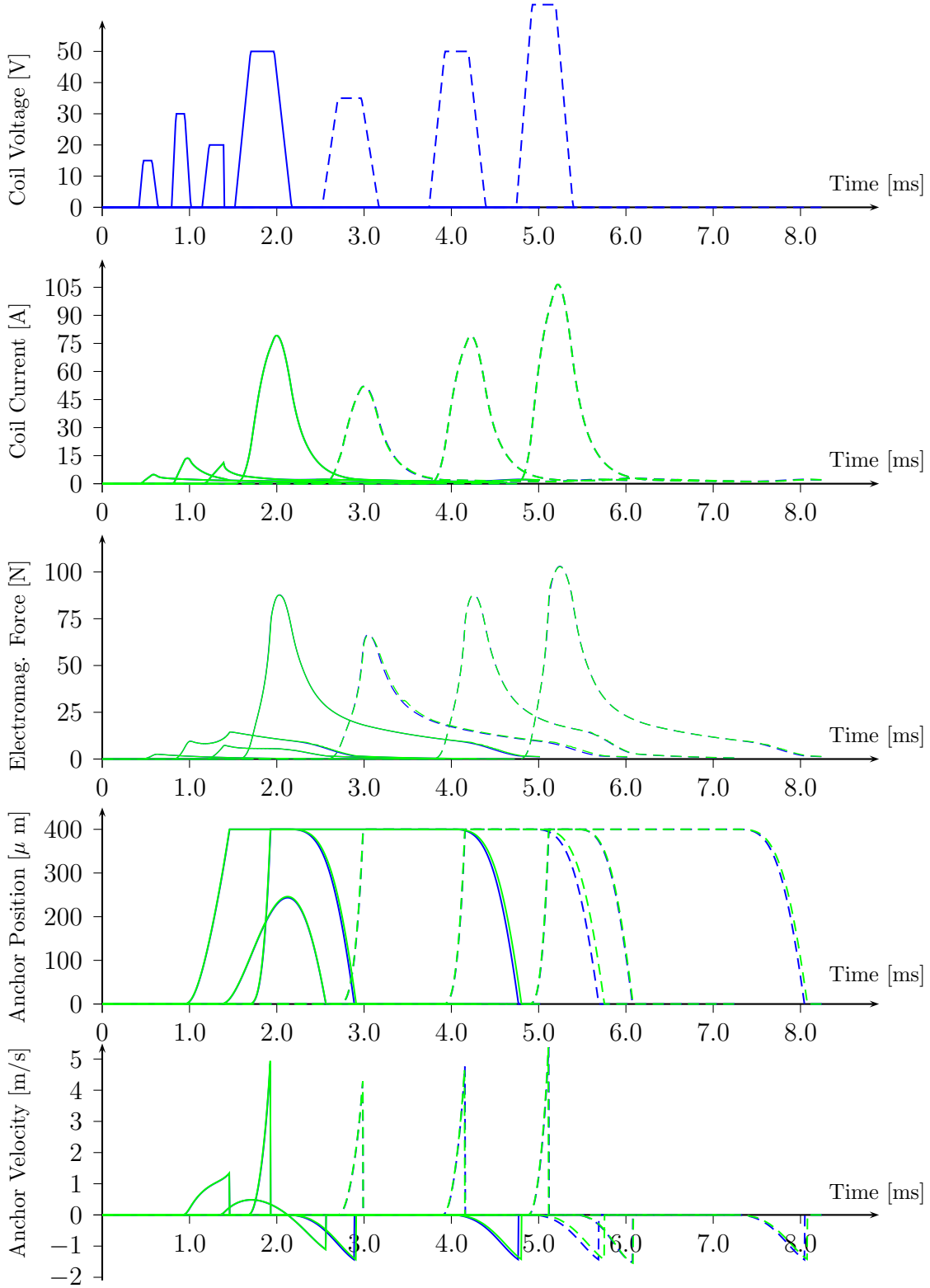

Figure 5.7: Simulation results of an electromagnetic valve with a moving anchor using a nonlinear model of order $n = 629$ (blue lines) versus a reduced order model of order $n = 40$ (green lines). The solid lines represent the input/output signals of the *training trajectories*. Whereas, the dashed lines represent the input/output signals of the *validation trajectories*.

Excitation Signal	Simulation Time (sec)	
	Full Order Nonlinear Model $n = 629$	Reduced Order TPWL Model $n = 40$
1	67.6	6.9
2	181.5	6.4
3	188.0	7.6
4	201.6	7.3
5	224.2	6.8
6	215.6	9.4
7	220.8	7.6

Table 5.2: The simulation time of the full order nonlinear model versus the simulation time of the reduced order model including motion

For the purpose of validation, three further simulation runs are carried out using both the full order model (5.1) coupled to the mechanical equation (5.29) and the generated reduced order model (5.30) coupled to same mechanical equation. In the first and third validation runs, the input voltage signals are chosen to have different amplitudes to the ones used in the model generation. Whereas in the second validation run, the same excitation signal used in the fourth training trajectory is applied, however, the stiffness constant of the mechanical spring is doubled to $k = 20$ KN/m.

The simulation results in Fig. 5.7 show a very good matching among the outputs of the full order and the reduced order device models, with the reduced order model being approximately $10 - 30$ times faster than the original model in all simulation runs as it is shown in the table 5.2.

It is should be stressed at this point that applying excitation signals that significantly differ in their shapes and amplitudes from the signals that have been used for generating the training trajectories can cause a degradation in the approximation accuracy of the reduced order model. This behavior is expected, since such input signals can drive the simulation trajectories to new regions of the state space of the original nonlinear EM field model (5.1). In those regions, the behavior of the nonlinear function $\mathbf{K}(\mathbf{a})\mathbf{a}$ is unknown to the model (5.30) and can not be well approximated as a weighted sum of the existing s_1 linearized models. However, this degradation can be easily alleviated

by linearizing the original nonlinear EM field model (5.1) at several points along the new simulation trajectories, and appending the new linearized models to the ensemble of linearized models in (5.15) after reducing their order.
This flexibility in expanding the validity regions of the generated reduced order models without the need to repeat the model generation procedure from the very beginning is considered as one of the major advantage of the proposed method.

The effect of varying the s_2 parameter

In order order to demonstrate the effect of varying the parameter s_2 on the accuracy of the generated reduced order model, three simulation runs are performed using the reduced order EM field model (5.30) coupled to the mechanical equation (5.29).

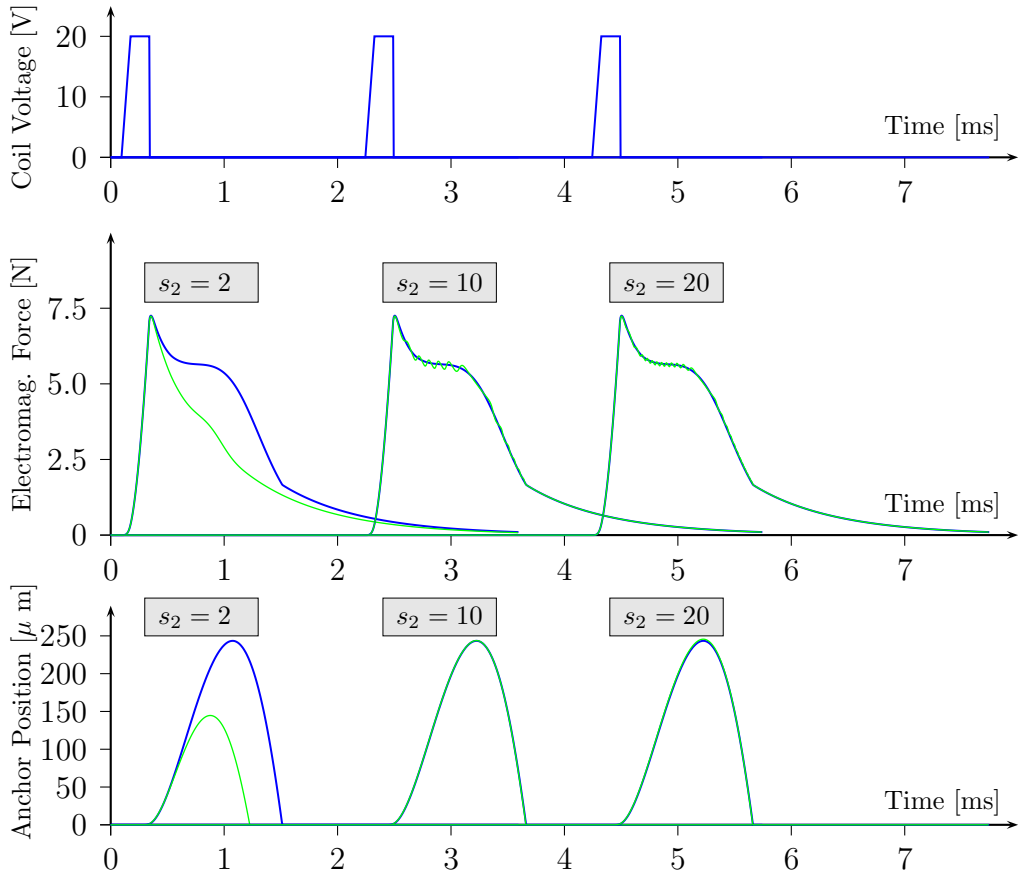

Figure 5.8: An example showing the effect of varying the number of sampling points of the position dependent matrices on the accuracy of the reduced order EM device model.

The value of the parameter s_2 has been set to $s_2 = 2$, $s_2 = 10$, and $s_2 = 20$ in the three simulations respectively. The simulation results in Fig. 5.8 show that the approximation model (5.30) with $s_2 = 2$ fails in achieving a good approximation of the original model (5.1) due to the very poor approximation of the position dependant matrices $\mathbf{K}^{\mathrm{BEM}}(\mathbf{x})$ and $\mathbf{R}(\mathbf{x})$. In contrast, the model (5.30) with $s_2 = 10$ achieves a very good accuracy regarding the simulated anchor position signal, however, the induced electromagnetic force signal is not smoothly approximated due to the interpolation error of matrices $\mathbf{K}^{\mathrm{BEM}}(\mathbf{x})$ and $\mathbf{R}(\mathbf{x})$. Finally, the best approximation results have been achieved using the setting $s_2 = 20$.

5.4.4 Multiobjective design optimization

In many industrial applications, electromagnetic devices are parts of complex systems containing for example mechanical or hydraulic components. Therefore, for a given electromagnetic device, the design of the surrounding mechanical or hydraulic components can be optimized in order to achieve an optimal performance of the whole system.
In this paragraph, the reduced order model (5.30) of the electromagnetic valve is exploited to perform a multiobjective optimization of the design of a mechanical component in the valve, namely the mechanical spring.
The spring design has a significant influence on the performance criteria of an electromagnetic valve, such as its opening and closing time. The design of the mechanical spring in this example is defined by two design parameters, namely its pre-tensioning force $p_1 = f_s(x_0)$ and its mechanical constant $p_2 = k$. The goals of the design optimization is to find a spring design that achieves a fast valve opening and closing time while generating a minimal amount of Ohmic losses in the excitation coil. Therefore, two design objectives are minimized, the total time needed for opening and closing the valve using the given excitation signal, and the total Ohmic losses in the excitation coils $J = R_{coil} \int_0^T i^2(t)dt$.
The performance of each design is evaluated using the reduced order model (5.30) coupled to the mechanical equation (5.29). The variation of the spring design parameters affects directly the mechanical equation (5.29). The optimization run is carried out using the ϵ-MOEA multiobjective optimization algorithm [18]. A total number of 20000

designs have been evaluated during the optimization run.

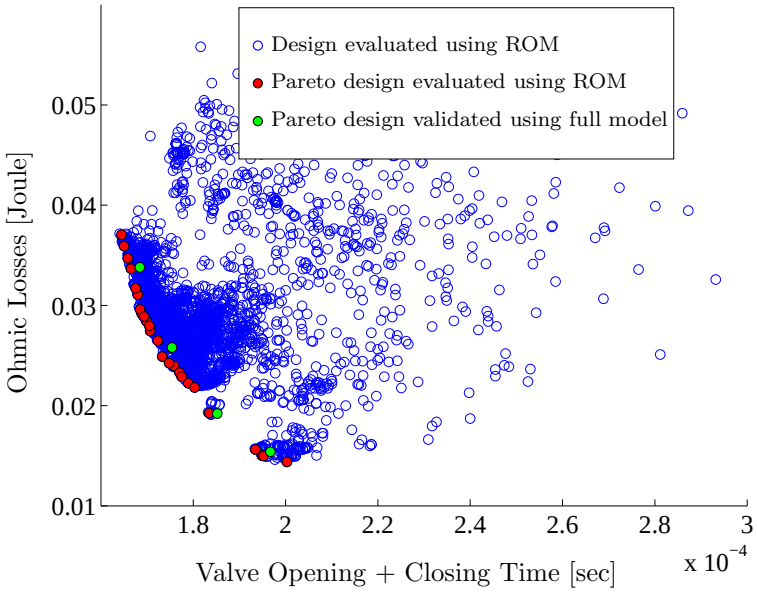

Figure 5.9: Two objectives design optimization results using a reduced order model of the electromagnetic valve.

The multiobjective optimization algorithm aims at improving both design objectives simultaneously, and to find all the Pareto optimal designs at which no improvement of one design objective is possible without worsening the second design objective. The Pareto optimal designs are marked with red circles in Fig. 5.9. Four of the Pareto designs are validated using the full order nonlinear model (5.1) coupled to (5.29). The validation results marked with green circles in Fig. 5.9 show a very good matching with the results calculated using the reduced order device model. The total time required for performing the optimization was almost 55 hours using one CPU. The evaluation of the same number of design variants using the full order nonlinear model would have taken approximately 2500 hours (104 days) using one CPU. This remarkable speed up factor shows the benefit of integrating the use of the proposed reduced order models in the design process of electromagnetic devices.

5.5 Switching the Excitation Signal Type Between Voltage & Current

In many industrial applications, electromagnetic devices are excited using a mixture of voltage signals and current signals following sophisticated control strategies. For example, some electromagnetic valves are driven using a constant voltage signal until the maximum allowed current is reached, then the controller regulates the coil current at its maximum allowed value. In order to simulate such a case, it is necessary to switch the excitation signal type from voltage to current and vice versa during the simulation run.

The electromagnetic field model that is excited using a current signal is given by:

$$\mathbf{C}\dot{\mathbf{a}} + \left[\mathbf{K}\left(\mathbf{a}\right) + \mathbf{K}^{\mathrm{BEM}}(\mathbf{x})\right]\mathbf{a} = \mathbf{b}i \tag{5.31}$$

whereas, the electromagnetic field model that is excited using a voltage signal is given by:

$$\left[\mathbf{C} + \frac{\mathbf{b}\mathbf{b}^T}{R}\right]\dot{\mathbf{a}} + \left[\mathbf{K}\left(\mathbf{a}\right) + \mathbf{K}^{\mathrm{BEM}}(\mathbf{x})\right]\mathbf{a} = \frac{\mathbf{b}}{R}u \tag{5.32}$$

It is clear that the current driven EM field model (5.31) and voltage driven EM field model (5.32) have different input/output behavior, and consequently they require, theoretically, different projection matrices for reducing their order. However, if we succeed in finding an optimal projection matrix for both models, then their corresponding reduced order models will share the same state-vector. This in turn significantly eases the process of switching the excitation signal type from current to voltage and vice versa during the device simulation using the reduced order models, as it will be shown in the following example.

We assume that the electromagnetic valve is simulated starting from the time step $t = 0$ using the voltage driven EM field model (5.32). The applied excitation signal is a constant voltage signal of amplitude $u = 45$ volts, as it is shown in Fig. 5.10. During the progress of the simulation, the coil current value increases until it reaches the maximum allowed current value $I_{max} = 10$ Amperes. At this moment the controller regulates the

current at its maximum allowed value $I_{max} = 10$ Amperes, therefore the valve is simulated starting from the time step t_{s_1} using the current driven EM field model (5.31) with a constant current excitation signal I_{max}. The value of the state-vector $\mathbf{a}(t_{s_1})$ can be used as an initial conditions for the current driven model (5.31) since both models (5.31), (5.32) share the same physical state-vector (i.e. the magnetic vector potential field). At a certain moment $t_{s_2} = 0.7$ms, the excitation signal is switched back again to a voltage signal of amplitude $u = 0$, therefore, the value of the state-vector $\mathbf{a}(t_{s_2})$ is used as an initial conditions for the voltage driven model (5.32), and the simulation is continued till reaching the time point t_{end}.
Now, if all the state-vectors that are simulated using both models (5.31), (5.32) are assembled in the snapshots matrix:

$$\mathbf{X} = \left[\overbrace{\mathbf{a}_0, \ldots, \mathbf{a}_{s1}}^{\text{voltage driven}}, \ \overbrace{\mathbf{a}_{s1+\Delta t}, \ldots, \mathbf{a}_{s2}}^{\text{current driven}}, \ \overbrace{\mathbf{a}_{s2+\Delta t}, \ldots, \mathbf{a}_{end}}^{\text{voltage driven}} \right] \tag{5.33}$$

then the proper orthogonal decomposition approach POD, can be exploited to generate a projection matrix $\mathbf{V}$ that provides an optimal low rank approximation of all the simulated state-vectors along the whole simulation trajectory $\mathbf{a}(t_0) \rightarrow \mathbf{a}(t_{s_1}) \rightarrow \mathbf{a}(t_{s_2}) \rightarrow \mathbf{a}(t_{end})$. The generated projection matrix $\mathbf{V}$ can be used to generate a current driven reduced order EM field model:

$$\mathbf{C}_r \dot{\mathbf{a}}_r + \sum_{i=1}^{s_1} \alpha_i \left(\mathbf{a}_r\right) \left[\mathbf{L}_{ri} \mathbf{a}_r + \mathbf{g}_{ri}\right] + \sum_{j=1}^{s_2} \beta_j(\mathbf{x}) \mathbf{K}_{rj}^{\mathrm{BEM}} \, \mathbf{a}_r = \mathbf{b}_r \mathbf{i} \tag{5.34}$$

and a voltage driven reduced order EM field model:

$$\left[\mathbf{C}_r + \frac{\mathbf{b}_r \mathbf{b}_r^T}{R}\right] \dot{\mathbf{a}}_r + \sum_{i=1}^{s_1} \alpha_i \left(\mathbf{a}_r\right) \left[\mathbf{L}_{ri} \mathbf{a}_r + \mathbf{g}_{ri}\right] + \sum_{j=1}^{s_2} \beta_j(\mathbf{x}) \mathbf{K}_{rj}^{\mathrm{BEM}} \, \mathbf{a}_r = \frac{\mathbf{b}_r}{R} u \tag{5.35}$$

Now, both reduced order models (5.35), (5.34) share the same state-vector. Therefore, when switching the excitation signal type from current to voltage and vice versa during the simulation, the last simulated state-vector using one of the models can be used as an initial values vector for the simulation using the other model, without the need of performing any subspace transformation.

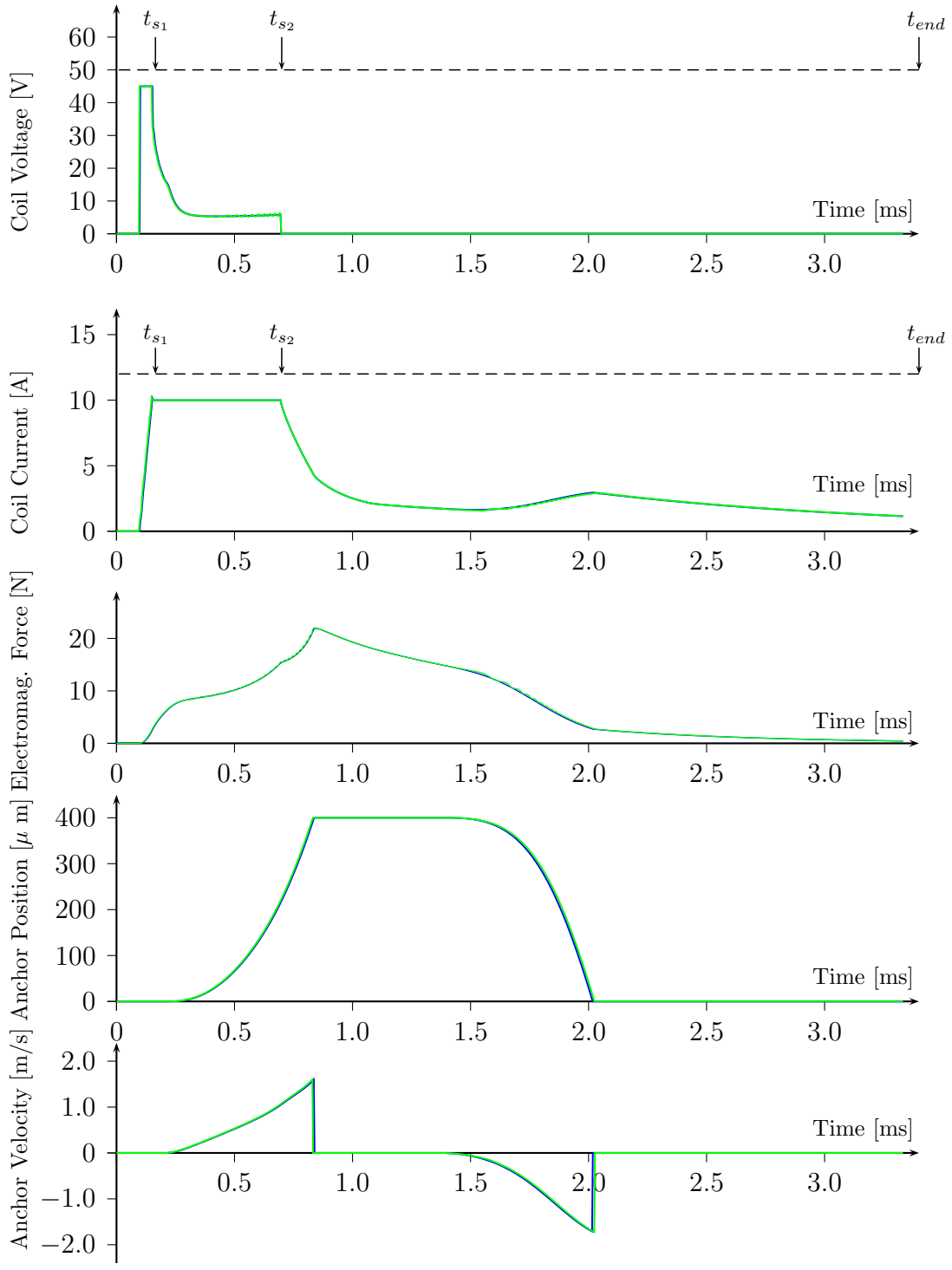

Figure 5.10: Simulation results of an EM valve using a reduced order model $n = 40$ coupled to the mechanical equation (green line) versus the results generated using the high order nonlinear model $n = 629$ coupled to the mechanical equation (blue line). The excitation signal type is switched from voltage to current and vice versa during the simulation run.

Finally, it is worth mentioning that the device simulation using the using the high order nonlinear models (5.31), (5.32) coupled to the mechanical equation required a total simulation time of 321 seconds. Whereas the same simulation using the reduced order ($n = 40$) EM field models (5.35), (5.34) coupled to the mechanical equation has required a total time of 9.89 seconds.

Chapter 6

PARAMETRIC MOR OF MOVING NONLINEAR ELECTROMAGNETIC DEVICES

6.1 Overview

In this chapter, we extend our work to generate fast and accurate *parametric reduced order models* of moving nonlinear electromagnetic devices. Such models are able to approximate the high order models of electromagnetic devices and their variations under materials nonlinearity, components movement, and the change of design parameters of the modeled device.

Additionally, we address the issue generating an optimal reduction subspace for the high order parametric models. For this purpose, three different algorithms based on the proper orthogonal decomposition POD are presented, and their performance is compared by applying them to the order reduction of a parametric model of an electromagnetic device.

Finally, a new approach for selecting the positions of the training points of the parametric reduced order model in the design parameters space is introduced.

It is worth mentioning that the presented results in this chapter have been partially published in our work [3]

6.2 The High Order Parametric Approximation Model

Let $\mathbf{p} \in \mathbb{R}^m$ be a vector containing a number of m design parameters of an EM device. When applying the BEM-FEM method, the parametric spatially discretized EM field model can be written as:

$$\begin{cases} \mathbf{C}(\mathbf{p})\dot{\mathbf{a}} + \left[\mathbf{K}(\mathbf{a},\mathbf{p}) + \mathbf{K}^{\mathrm{BEM}}(\mathbf{x},\mathbf{p})\right]\mathbf{a} = \mathbf{r}(\mathbf{p}) \\ f_{\mathrm{mag}} = \mathbf{a}^{\mathbf{T}}\,\mathbf{R}(\mathbf{x},\mathbf{p})\,\mathbf{a} \end{cases} \tag{6.1}$$

where the vector $\mathbf{r}(\mathbf{p})$ contains the contributions of all sources of current densities in the modeled device, such as the contributions of electrical excitation coils that are connected to current/voltage sources, in addition to the contribution of permanent magnets, as has been discussed in paragraph 2.8.

For the sake of notation clarity, the electromagnetic force is assumed to be calculated for one moving device component. The extension for the case of multiple components is straight forward. Under this assumption, the mechanical equations describing the movement of one rigid device components is give by:

$$m(\mathbf{p})\ddot{x} + d(\mathbf{p})\dot{x} + k_m(\mathbf{p})x = f_{\mathrm{mag}} \tag{6.2}$$

where m, d, k_m are respectively the mass, the damping, and the stiffness constants of the mechanical equations, and x is the state variable describing the position of the moving device component. The dependency of the matrices $\mathbf{C}, \mathbf{K}, \mathbf{K}^{\mathrm{BEM}}, \mathbf{R}$ and the vector $\mathbf{r}$ in (6.1) on the vector $\mathbf{p}$ of design parameters is ,in general, very complex, and their derivatives with respect to the vector $\mathbf{p}$ are typically not available.

However, at a given point in the design parameter space $\mathbf{p} \in \mathbb{R}^m$, the high order nonlinear electromagnetic field model (6.1) can be accurately approximated in the neighboring regions of some training trajectories by reduced order approximation model (5.26)-(5.27) according to the approach presented in the previous chapter. Now, when applying the aforementioned scheme to generate reduced order EM field models at s_3 different points $\{\mathbf{p}_1, \ldots \mathbf{p}_{s_3}\}$ in the design parameters spaces, then the high order parametric model (6.1)

can be approximated by:

$$\sum_{k=1}^{s_3} \gamma_k(\mathbf{p})\mathbf{C}_k\dot{\mathbf{a}} + \sum_{k=1}^{s_3} \gamma_k(\mathbf{p}) \sum_{i=1}^{s_1} \alpha_i(\mathbf{a})[\mathbf{g}_{k,i} + \mathbf{L}_{k,i}\mathbf{a}] + \sum_{k=1}^{s_3} \gamma_k(\mathbf{p}) \sum_{j=1}^{s_2} \beta_j(\mathbf{x})\mathbf{K}_{k,j}^{\mathrm{BEM}}\,\mathbf{a} = \sum_{k=1}^{s_3} \gamma_k(\mathbf{p})\mathbf{r}_k \tag{6.3}$$

$$f_{\mathrm{mag}} = \mathbf{a}^T \left[\sum_{k=1}^{s_3} \gamma_k(\mathbf{p}) \sum_{j=1}^{s_2} \beta_j(\mathbf{x})\mathbf{R}_{k,j} \right] \mathbf{a} \tag{6.4}$$

such that $\sum_{i=1}^{s_1} \alpha_i = 1, \quad \sum_{j=1}^{s_2} \beta_j = 1, \quad \sum_{k=1}^{s_3} \gamma_k = 1.$

6.3 The Weighting Function

The weighting function $\boldsymbol{\gamma}$ has a very important influence on the approximation accuracy of the model (6.3) (6.4). This importance increases even more if a low number of model training points s_3 in the design parameters space $\mathbf{p} \in \mathbb{R}^m$ is selected. In contrast, if a large number s_3 of sampling points is chosen, then good approximation results can be achieved using simple weighting functions.

In general, the weighting function $\boldsymbol{\gamma}$ should be constructed in such a way that it gives higher weighting value γ_k for the matrices and vectors in (6.3) (6.4) that are sampled at design points in the design parameters space that are near to the currently simulated design point $\mathbf{p}$.

In this work, we have chosen the special weighting chosen $\zeta(\mathbf{p}, \mathbf{a}) = \gamma(\mathbf{p})\alpha(\mathbf{a})$, $\eta(\mathbf{p}, \mathbf{x}) = \gamma(\mathbf{p})\beta(\mathbf{x})$ in approximating the dependency of the matrices and vectors of the original model (6.1) on the design parameters vector $\mathbf{p}$. This selection is not unique, and different weighting schemes $\zeta(\mathbf{p}, \mathbf{a})$, $\eta(\mathbf{p}, \mathbf{x})$ can be exploited. However, the optimal choice of weighting functions is out of the scope of this work. Nevertheless, it would be an interesting field to be investigated in future research works.

In the presented numerical example in this chapter, the weighting function $\boldsymbol{\gamma}$ is chosen

to be *linearly dependent* on the Euclidian distance between the current design parameter point and all the s_3 design points at which the model (6.3) (6.4) is trained. The choice of a linear weighting function is made due to its simplicity. However, this would be an additional field where further research efforts are required.

6.4 Building the Global Projection Subspace

In the previous chapter, we have shown that the proper orthogonal decomposition approach can be efficiently applied to reduce the order of the high order nonlinear models of electromagnetic field. The application of the POD approach can be directly extended to the case of order reduction of the parametric model (6.3), (6.4). This is due to the ability of the POD approach to approximate all the simulated state-vectors of the parametric model (6.1) at different points in the design parameters space by a linear combination of the vectors of an optimal projection matrix.
In this paragraph, we present three different algorithms for finding the optimal orthogonal vectors of the projection matrix using the POD approach, and we analyze their advantages and limitations. Thereafter, the performance of the three algorithms is compared by applying them to reduce the order of a parametric approximation model (6.3), (6.4) for an electromagnetic valve.

Algorithm 3 Generating the global projection subspace

1: Initialize the snapshots matrix with an empty matrix $\mathbf{X} = [\,]$.
2: **for** $i \leftarrow 1, s_3$ **do**
3: Add all the simulated state-vectors of the i^{th} design to the snapshots matrix $\mathbf{X} = [\mathbf{X}, \mathbf{a}_1^i, \ldots, \mathbf{a}_s^i]$,
4: **end for**
5: Apply the POD approach to approximate all the state vectors in the snapshots matrix by a linear combination of a low number q of orthogonal vectors. The orthogonal vectors are the columns of the projection matrix $\mathbf{V} \in \mathbb{R}^{n \times q}$.

$$\mathbf{X} \approx \overbrace{\left[\mathbf{v}_1, \mathbf{v}_2, \ldots, \mathbf{v}_q\right]}^{\mathbf{V}} \left[\overbrace{\mathbf{a}_{r1}, \ldots, \mathbf{a}_{rs}}^{\text{design 1}}, \overbrace{\mathbf{a}_{r1}, \ldots, \mathbf{a}_{rs}}^{\text{design 2}}, \ldots, \overbrace{\mathbf{a}_{r1}, \ldots, \mathbf{a}_{rs}}^{\text{design } s_3}\right].$$

The algorithm 3 is based on using the POD approach in building a reduction subspace that utilizes an optimal low rank approximation of all the simulated state vectors at the s_3 points in the design parameters space.
However, if the order n of the original parametric model (6.1) is very high and the overall number of simulated state-vectors in the snapshots matrix $\mathbf{X}$ is high as well, then the dimensions of the snapshots matrix $\mathbf{X}$ become very large. Consequently, applying the POD approach for generating the projection matrix $\mathbf{V}$ that provides the best low rank approximation of all the state-vectors in the snapshots matrix $\mathbf{X}$ becomes very computationally expensive and possibly not doable.
The algorithm 4 presents a solution for the aforementioned problem by utilizing a two steps strategy. In the first step, the POD approach is applied individually at each of the s_3 design points to find a projection matrix that provides an optimal low rank approximation of the simulated state-vectors of (6.1) at the considered point. Then in the second step, the POD approach is applied to find the final projection that provides an optimal low rank approximation of the vectors of all the calculated projection matrices from the first step.

Algorithm 4 Generating the global projection subspace

1: Initialize the group of all projection matrices with an empty matrix $\mathbf{V}_{all} = [\,]$.
2: **for** $i \leftarrow 1, s_3$ **do**
3: Apply the POD approach to find a projection matrix $\mathbf{V}_i$ that provides an optimal low rank approximation of all the simulated state-vectors of the model (6.1) at the i^{th} design point.

$$\overbrace{\left[\mathbf{a}_1, \ldots, \mathbf{a}_s\right]}^{\text{design i}} \approx \overbrace{\left[\mathbf{v}_1, \mathbf{v}_2, \ldots, \mathbf{v}_{q_i}\right]}^{\mathbf{V}_i} \overbrace{\left[\mathbf{a}_{r1}, \ldots, \mathbf{a}_{rs}\right]}^{\text{design i}}.$$

4: Add the vectors of the projection matrix $\mathbf{V}_i$ to the group of all projection matrices $\mathbf{V}_{all} = [\mathbf{V}_{all}, \mathbf{V}_i]$,
5: **end for**
6: Apply the POD approach to find the final projection matrix $\mathbf{V} \in \mathbb{R}^{n \times q}$ that provides an optimal low rank approximation of all the vectors in the group $\mathbf{V}_{all}$.

The computational cost of the algorithms 4 is much lower than the one of the algorithm 3 in the cases where the parametric model (6.1) has a very large order n and the overall

number of the simulated state-vectors is very large. However, its major disadvantage is the very slow decay rate of the singular values when applying the POD to the matrix $\mathbf{V}_{all}$. This can be traced back to the fact that all the vectors that are contained in the group $\mathbf{V}_{all} = \Big[\mathbf{V}_1, \mathbf{V}_2, \ldots, V_{s_3}\Big]$ have a norm equal to one, since they result from applying a singular values decomposition to their corresponding state-vectors. Therefore, when applying the second POD step to the matrix $\mathbf{V}_{all}$, then all the vectors in $\mathbf{V}_{all}$ are almost equally important. This makes the decay rate of the singular values very slow.
A solution to this problem is presented in the algorithm 5, in which each vector in the local projection matrices $\mathbf{V}_i$ is scaled by its corresponding singular value before adding it to the matrix $\mathbf{V}_{all}$. Therefore, the importance of each vector in $\mathbf{V}_{all}$ with respect to the approximation of its corresponding group of simulated state-vectors is preserved. Now, when applying the second POD step to the matrix $\mathbf{V}_{all}$, the singular values decay much faster than the case of the algorithm 4. Moreover, the vectors of the final projection matrix V generated using this algorithm are very similar results to the that are generated using the algorithm 3, as it will be shown in the following numerical example.

Algorithm 5 Generating the global projection subspace

1: Initialize the group of all projection matrices with an empty matrix $\mathbf{V}_{all} = [\,]$.
2: **for** $i \leftarrow 1, s_3$ **do**
3: Apply the POD approach to find a projection matrix $\mathbf{V}_i$ that provides an optimal low rank approximation of all the simulated state-vectors of the model (6.1) at the i^{th} design point.

$$\overbrace{\Big[\mathbf{a}_1, \ldots, \mathbf{a}_s\Big]}^{\text{design i}} \approx \overbrace{\Big[\mathbf{v}_1, \mathbf{v}_2, \ldots, \mathbf{v}_{q_i}\Big]}^{\mathbf{V}_i} \overbrace{\Big[\mathbf{a}_{r1}, \ldots, \mathbf{a}_{rs}\Big]}^{\text{design i}}.$$

4: Scale each vector $\mathbf{v}_j$ in the generated projection matrix $\mathbf{V}_i$ with its corresponding singular value σ_j that results from the proper orthogonal decomposition.
5: Add the vectors of the matrix $\mathbf{V}_i$ after scaling them with their corresponding singular values to the group of all projection matrices

$$\mathbf{V}_{all} = \Big[\mathbf{V}_{all}, \overbrace{\big[\sigma_1\mathbf{v}_1, \ldots, \sigma_{q_i}\mathbf{v}_{q_1}\big]}^{\tilde{\mathbf{V}}_i}\Big]$$

6: **end for**
7: Apply the POD approach to find the final projection matrix $\mathbf{V} \in \mathbb{R}^{n\times q}$that provides an optimal low rank approximation of all the vectors in the group $\mathbf{V}_{all}$.

Finally, the matrix $\mathbf{V}$ that has been generated using one of the three presented algorithms can be used to reduce the order of the sampled matrices and vectors in (6.3)(6.4) from the order n to the order $q \ll n$, by projecting them onto the subspace spanned by its columns according to the Galerkin projection that has been discussed in the paragraph 3.1.1.

$$\sum_{k=1}^{s_3} \gamma_k(\mathbf{p}) \mathbf{C}_{rk} \dot{\mathbf{a}}_r + \sum_{k=1}^{s_3} \gamma_k(\mathbf{p}) \sum_{i=1}^{s_1} \alpha_i(\mathbf{a}_r)[\mathbf{g}_{r_{k,i}} + \mathbf{L}_{r_{k,i}} \mathbf{a}_r] + \sum_{k=1}^{s_3} \gamma_k(\mathbf{p}) \sum_{j=1}^{s_2} \beta_j(\mathbf{x}) \mathbf{K}^{\mathrm{BEM}}_{r_{k,j}} \mathbf{a}_r = \sum_{k=1}^{s_3} \gamma_k(\mathbf{p}) \mathbf{r}_{r_k} i \tag{6.5}$$

$$f_{\mathrm{mag}} = \mathbf{a}_r^T \left[\sum_{k=1}^{s_3} \gamma_k(\mathbf{p}) \sum_{j=1}^{s_2} \beta_j(\mathbf{x}) \mathbf{R}_{r_{k,j}} \right] \mathbf{a}_r \tag{6.6}$$

6.5 Numerical Example

In this paragraph, a parametric reduced order model of the electromagnetic valve presented in the paragraph 5.3.3 is generated. Three geometrical design parameters are varied in the full order nonlinear model (6.1), namely the radius of the moving anchor p_1 , its thickness p_2, and the position of the coil along the x-axis p_3.

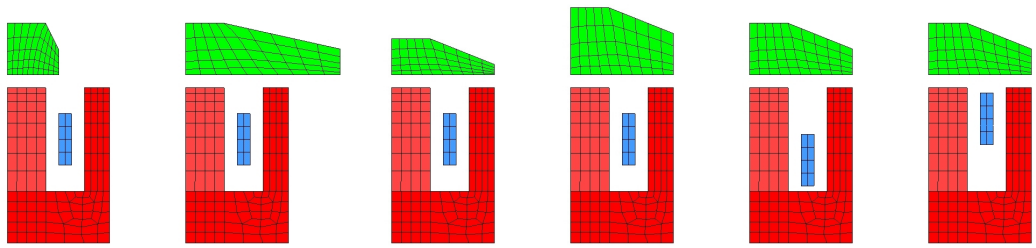

(a) $p_{1_{min}}$ (b) $p_{1_{max}}$ (c) $p_{2_{min}}$ (d) $p_{2_{max}}$ (e) $p_{3_{min}}$ (f) $p_{3_{max}}$

Figure 6.1: The figures (a)-(f) illustrate six different geometries of the electromagnetic valve. The geometries are generated by setting one of the three design parameter to its minimum or maximum value.

The two parameters p_1, p_2 have a direct influence on the anchor mass in the equation (6.2) as it can be clearly seen in Fig. 6.1. The dependency of the anchor's mass on its radius and thickness in (6.2) is calculated in this example using simple geometrical relations.

In the three dimensional design parameter space $\mathbf{p} \in \mathbb{R}^3$, a total number of $s_3 = 125$ sampling points are chosen as training points for the model (6.3) (6.4). The training points are uniformly distributed in the parameter space $\mathbf{p} \in \mathbb{R}^3$ using a five-levels full factorial design of experiment DoE scheme [17]. All the s_3 sampled designs were simulated using the same excitation signal, the same size of the simulation time step $\Delta t = 5\mu$s, and the same number of simulation steps $s = 700$. The aforementioned settings have been used later on for simulating the reduced order models as well.

At each of the $s_3 = 125$ designs, the nonlinear model (6.1) is linearized at a number of linearization points that are determined using the selection algorithm 1 with $\tau_1 = 0.02$. The number of required linearization points was between 55-75 points per design point. The position dependent matrices $\mathbf{K}^{\mathrm{BEM}}(\mathbf{x})$, $\mathbf{R}(\mathbf{x})$ were extracted at $s_2 = 20$ uniformly distributed positions within the movement range $[0, 400]\mu$m. This has resulted in a total number of $20 \times 125 = 2500$ distinguished position dependant matrices $\mathbf{K}^{\mathrm{BEM}}(\mathbf{x})$, $\mathbf{R}(\mathbf{x})$. Finally, three different projection matrices $\mathbf{V}_1, \mathbf{V}_2, \mathbf{V}_3$ are are generated using the algorithms 3, 5, and 5 respectively. Each of the three matrices is theoretically expected to provide an optimal low rank approximation of all the $125 \times 700 = 87500$ simulated state-vectors. We remind at this point that the order of the nonlinear model (6.1) in this example is $n = 629$.

Three distinguished parametric reduced order models (6.5)(6.6) of order $n = 50$ are generated by projecting the parametric high order approximation model (6.3), (6.4) of order $n = 629$ on the subspaces spanned by the columns of the matrices $\mathbf{V}_1, \mathbf{V}_2, \mathbf{V}_3$ respectively.

In the next step, the three reduced three reduced order models coupled weakly to the mechanical equation (6.2) are used to perform a device simulation. The simulations are carried out at the same $s_3 = 125$ design points at which the three parametric models (6.5)(6.6) were generated, and using the same voltage excitation signal that was used for the model training. The simulation results in Fig. 6.3 have shown that the first and the third parametric reduced order models whose order was reduced using the reduction

algorithms 3 and 5 respectively produce an excellent matching to the results of the original high order nonlinear model (6.1). Moreover, it can be clearly seen in the Fig. 6.2 that the magnetic vector potential field that corresponds to vectors of the matrices $\mathbf{V}_1$ and $\mathbf{V}_3$ are almost identical. This indicates that the algorithm 3 and algorithm 5 build almost identical projection matrices. However, the algorithm 5 has a major advantage in comparison to the algorithm 3 in its required computational effort when both the order of the parametric model and the number of simulated state-vector are very large.

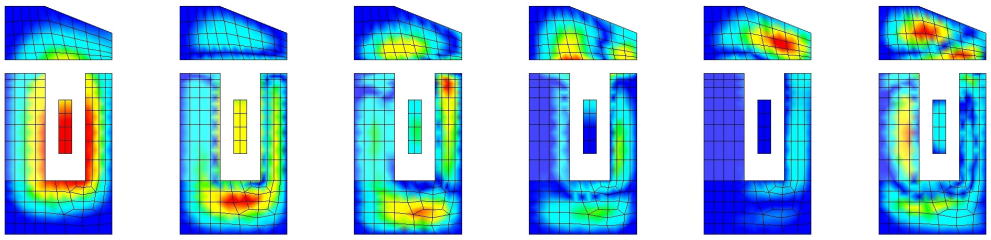

(a) First six vectors of the projection matrix $\mathbf{V}$ generated using the algorithm 3

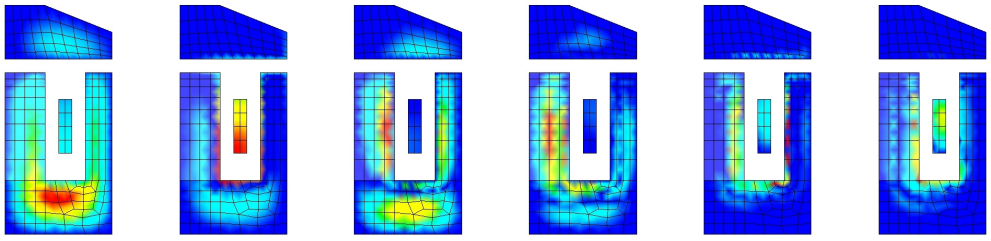

(b) First six vectors of the projection matrix $\mathbf{V}$ generated using the algorithm 4

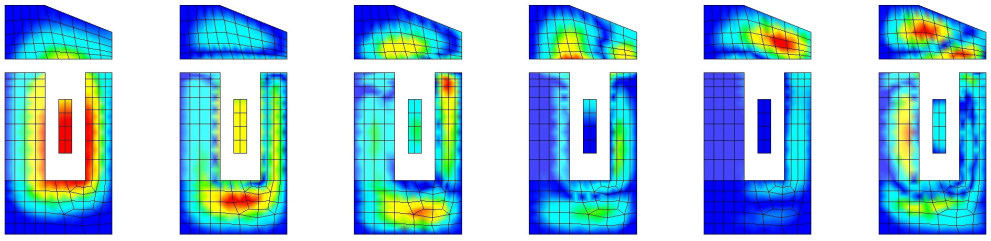

(c) First six vectors of the projection matrix $\mathbf{V}$ generated using the algorithm 5

Figure 6.2: The figures (a), (b), and (c) illustrate the magnetic vector potential field that correspond to the first six vectors in the projection matrix $\mathbf{V}$. The projection matrix $\mathbf{V}$ is generated in the figures (a),(b),(c) according to the algorithms 3, 4, and 5 respectively.

In contrast, the parametric reduced order model whose order was reduced using the reduction algorithms 4 fails in approximating the behavior of the original high order nonlinear model (6.1) as it is shown in Fig. 6.4. This indicate that its corresponding projection matrix $\mathbf{V}_2$ does not produce an optimal approximation of the state-vectors of the original high order parametric model (6.1). Moreover, the magnetic vector potential field that corresponds to the vectors of the projection matrix $\mathbf{V}_2$ are very different to their corresponding vectors of the matrices $\mathbf{V}_1$ and $\mathbf{V}_3$ in Fig.6.2. This proves that when applying a two steps POD approach, it is essential to scale the generated vectors of the local projection matrices with their corresponding singular values before applying the second POD step, as we have proposed in the algorithm 5.

It is worth mentioning that in all the simulation runs, the simulation using the generated parametric reduced order model (6.5), (6.6) took 30-40 times less simulation time than the high order nonlinear model (6.1).

In the next step, the parametric reduced order model that is generated using the projection matrices $\mathbf{V}_1$ is simulated at several points in the design parameters space $\mathbf{p} \in \mathbb{R}^3$ that are different from the $s_3 = 125$ training points. The simulation results in Fig. 6.5 show that the approximation accuracy of the reduced order model varies from a validation point to another. This is can be interpreted by the fact that in some regions of the parameters space, the behavior of the modeled device is very sensitive to the change in the values of design parameters. This implies that those critical regions have to be sampled with a higher density of training points during the model generation. Moreover, the device behavior can be more sensitive to the change in a certain design parameter than others. This imposes again sampling such a parameter in finer steps during the model generation.

It is clear that increasing the number of design points s_3 in the parametric reduced order model (6.5),(6.6) improves its approximation accuracy. However, doing this leads to a significant increase in the required computational effort for the model generation process. Therefore, a compromise has to be made between the desired model accuracy and the corresponding computational costs for its generation.

Additionally, in most industrial applications, the regions of the design parameters space in which the modeled electromagnetic device shows an optimal behavior – i.e. achieves the expected design goals – are much more important to be accurately approximated

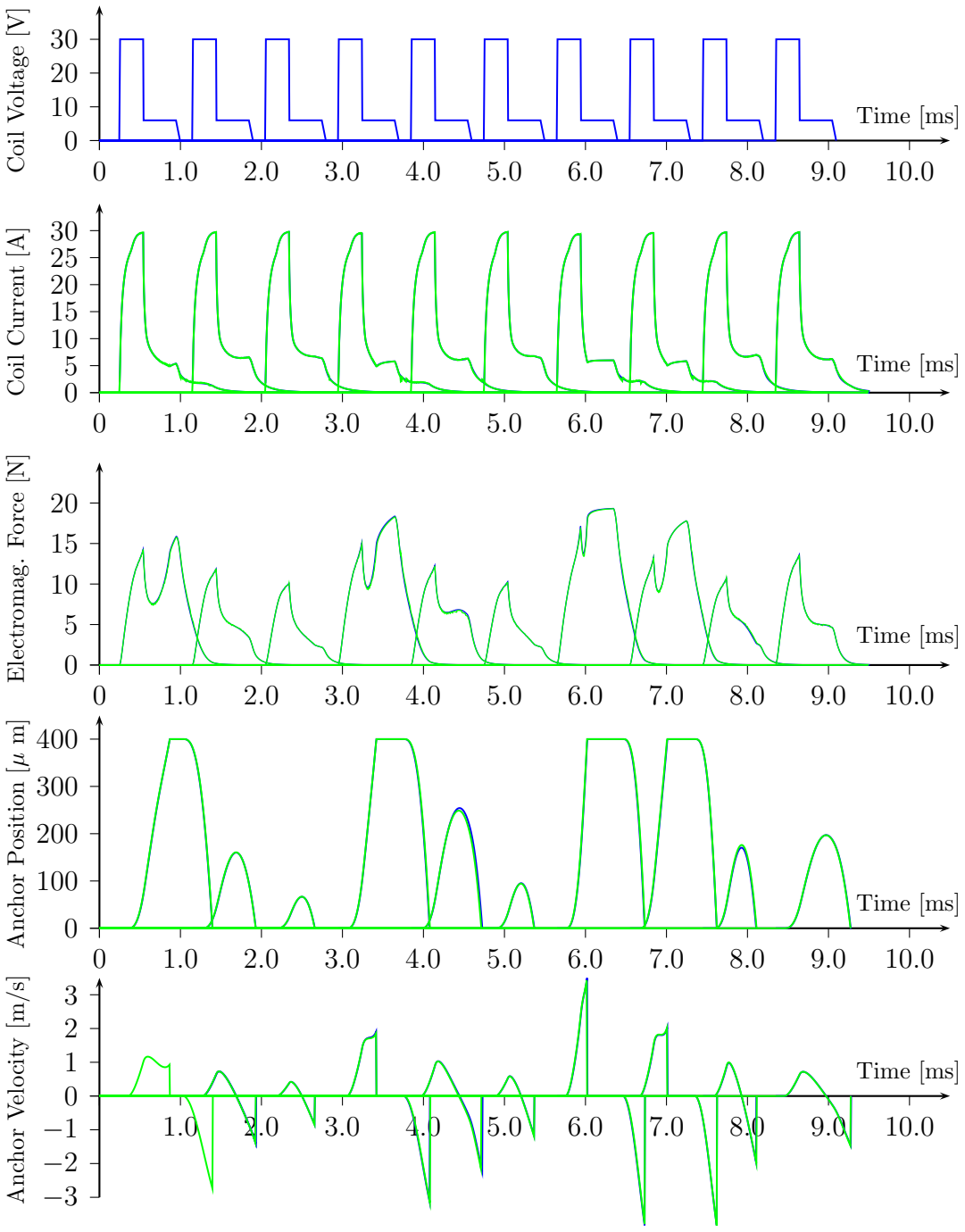

Figure 6.3: Simulation results of the full order nonlinear model $n = 629$ coupled to the mechanical equation (blue solid line) versus the ones of the parametric reduced order model $n = 50$ coupled to the mechanical equation (green solid line) at different *training points* in the parameters space. The result achieved using the algorithms 3 and 5 are almost identical, therefore, only the results achieved using the algorithm 3 are illustrated.

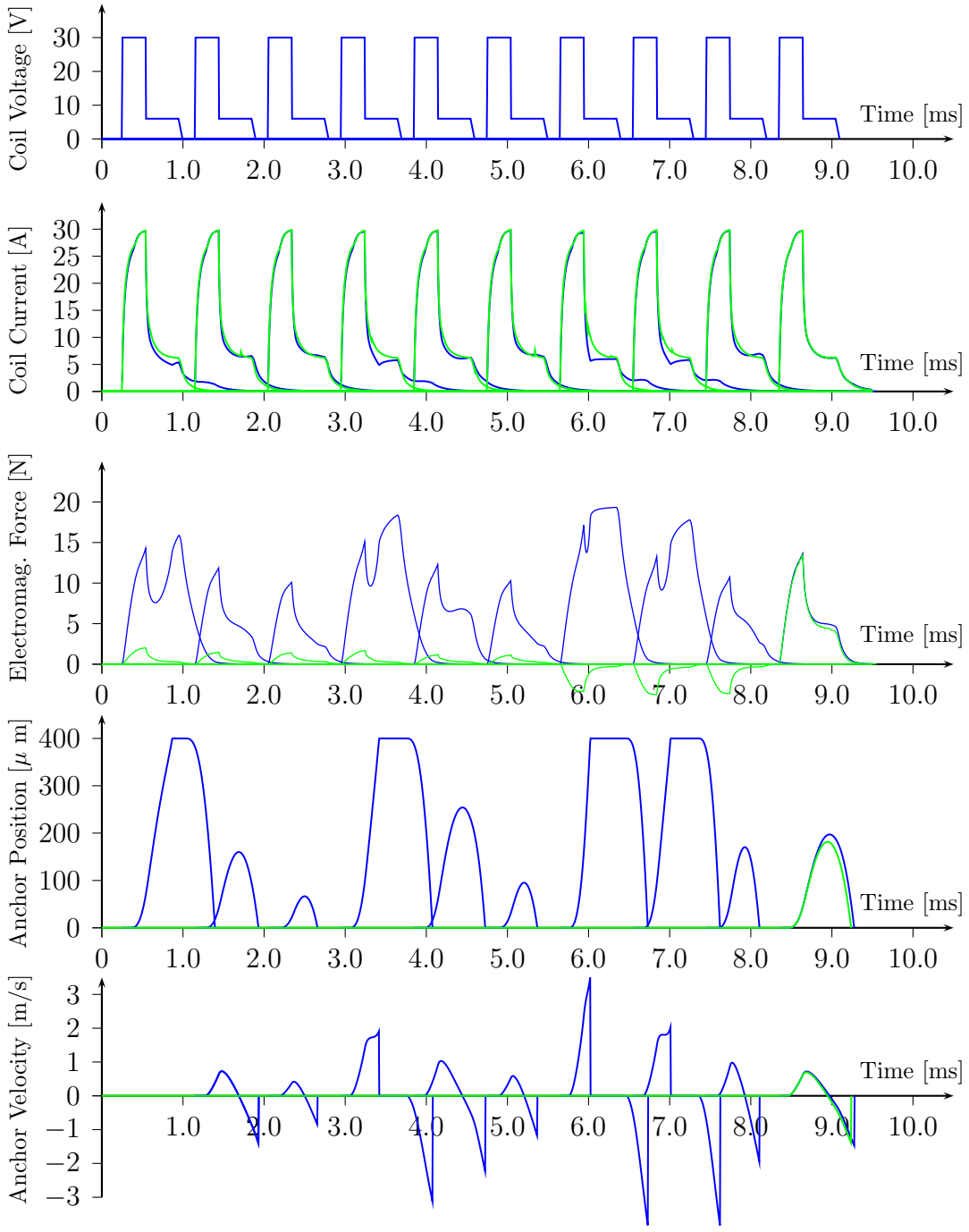

Figure 6.4: Simulation results of the full order nonlinear model $n = 629$ coupled to the mechanical equation (blue solid line) versus the ones of the parametric reduced order model $n = 50$ coupled to the mechanical equation (green solid line) at different *training points* in the parameters space. The projection matrix that is used for reducing the order of the parametric model is generated using the reduction algorithm 4.

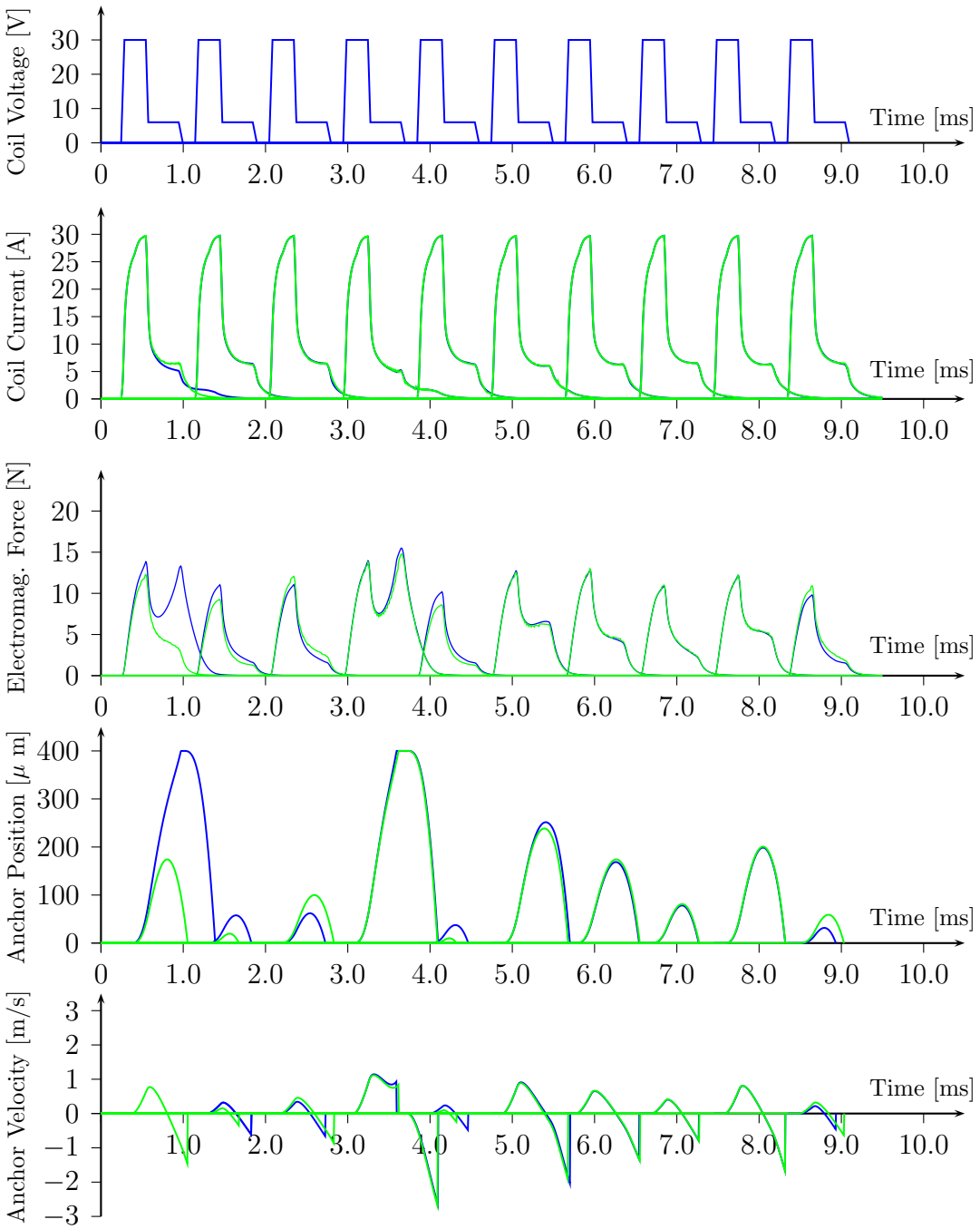

Figure 6.5: Simulation results of the full order nonlinear model coupled to the mechanical equation $n = 629$ (blue solid line) versus the ones of the parametric reduced order model $n = 50$ coupled to the mechanical equation (green solid line). The simulation are carried out at design points in the parameters space that are different from the $s_3 = 125$ training points.

using parametric reduced order models. Therefore, in the next paragraph, we propose a new strategy for generating fast parametric reduced order models of electromagnetic devices with a main focus on increasing the approximation accuracy of in the optimal regions of the design parameters space.

6.6 Controlling the Generation of Parametric Reduced Order Models Using Multiobjective Design Optimization Strategy

In this section, we propose a new strategy for controlling the generation of parametric reduced order models using a multiobjective design optimization strategy. The aim of the proposed strategy is to guarantee generating parametric reduced order models that have high approximation accuracy in the regions of design parameters space in which the modeled electromagnetic device achieves the best performance.

The proposed scheme starts with generating a parametric reduced order model (6.5),(6.6) of the modeled device at a relatively low number s_3 of training points in the design parameters space. The latter model coupled to the mechanical equation (6.2) is used for evaluating the design objective functions during the optimization process run. The full order nonlinear EM field model coupled to the mechanical equation (6.2) is used periodically for validating the best designs that have been found by the optimization algorithm. If the validation shows a large deviation between the results of the full order and the reduced order models, then the number s_3 of training points in the parametric reduced order model (6.5),(6.6) is expanded by the new design points at which large deviations are detected.

In this way, the accuracy of the parametric reduced order model (6.5),(6.6) is increased successively in the optimal regions of the design parameters space in which the modeled design shows the best performance.

The aforementioned approach is summarized in the following algorithm:

Algorithm 6 A strategy for controlling the generation of parametric reduced order models using a multiobjective design optimization strategy

1: Sample the design parameters space $\mathbf{p}$ with an initial number s_3 of design points using one of the well known design of experiment DoE schemes [17].
2: Build a parametric reduced order model (6.5), (6.6) at the s_3 sampled designs points.
3: **for** $i \leftarrow 1, N$ **do**
4: Run the multiobjective optimization algorithm to optimize the $\mathbf{p}$ design parameters, and evaluate the objective functions using the parametric reduced order EM field model coupled to the mechanical equations (6.2).
5: After τ number of optimization iterations, use the original high order nonlinear model (6.1) coupled to (6.2) to validate the best designs found by the optimization algorithm.
6: In case of large deviation between the high order and reduced order models, expand the parametric reduced order EM field model by adding new design points $\mathbf{p}$ at which the validation error is found to be larger than the user defined error bound.
7: **end for**

6.7 Numerical Example

In this section, the strategy for generating parametric reduced order models using a multiobjective design optimization is applied to the example of an electromagnetic valve.

Five parameters where varied during the optimization process, namely the thickness of the anchor p_1, the position of the coil along the x-axis p_2, the number of windings in the excitation coil p_3, the stiffness of the mechanical spring p_4, and the pre-tension force of the mechanical spring p_5. The resistance of the excitation coil R_{coil} is dependent on the number of windings p_3.

Two objective functions were to be minimized, the total time needed for opening and closing the valve using a given voltage excitation signal, and the total Ohmic losses in the excitation coil during an opening-closing cycle $J = R_{coil}(\mathbf{p}) \int_0^T i^2(t)dt$.

All the simulation runs in this example are carried out using the same voltage excitation signal, the same size of the simulation time step $\Delta t = 5\mu$s, and the same number of simulation steps 450.

Two design optimization runs were carried out using the ϵ-MOEA multiobjective optimization algorithm [18]. In the first run, the design objective functions were evaluated using the full order nonlinear EM field model (6.1) coupled to the mechanical equation

(6.2). After 8 hours run time, during which 350 designs were evaluated, the optimization algorithm succeeded in finding 5 designs near to the Pareto optimal front, however the latter designs did not cover more than 25% of the length of the Pareto optimal front. It took almost 34 hours and 2250 design evaluations to detect the whole Pareto optimal front that is shown in Fig. 6.6.

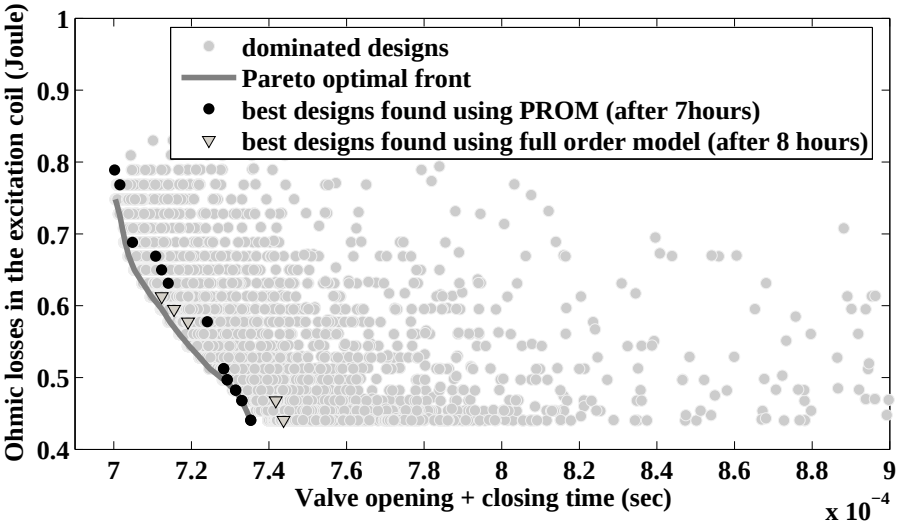

Figure 6.6: Optimization results using the full order nonlinear model coupled to the mechanical equation versus the results found using the proposed optimization strategy.

Alternatively in the second run, 3 hours were required for generating the parametric reduced order model (6.3),(6.4) of order $n = 50$ at $s_3 = 27$ design points. The generated reduced order model coupled to the mechanical equation (6.2) was used for evaluating the design objective functions. It took 4 hours to: evaluate 650 designs, validate 29 designs using the full order model (6.1) coupled to the mechanical equation, and to append all the 29 validated designs to the model (6.5),(6.6) according to the algorithm 6. The number of iterations at which the optimization results were validated using the full order model coupled to the mechanical equation is set to $\tau = 100$.

It can be clearly seen in Fig. 6.6 that the proposed optimization strategy succeeded in detecting 12 designs that cover almost 70% of the regions near to the true Pareto optimal front. This was achieved in a shorter time (7 hours in total), and using far less

number of design evaluations of the full order model (46 evaluations) compared to the first optimization run.

It should be stressed at this point that the main aim of the proposed strategy to generate fast parametric reduced order models that are specially accurate in the optimal regions of the design parameters space. Such models can be efficiently used for simulating and optimizing the design of the overlying complex systems. However, if the aim is only to perform a design optimization of the modeled device, and not to generate a parametric reduced order device model, then this strategy is not necessarily faster than performing a design optimization using the original model (6.1) coupled to the mechanical equation (6.2). This is due to the fact that generating parametric reduced order models of electromagnetic devices can be, in some cases, very computationally expensive.

Chapter 7

COUPLING THE REDUCED ORDER MODELS TO EXTERNAL NONLINEAR CIRCUITS

7.1 Overview

Power electronics circuits are widely used in many industrial applications to drive and control electromagnetic devices. The computer based simulation of such devices requires modeling the behavior of electromagnetic field in the considered devices, together with the behavior of their corresponding power electronic driving circuits. The coupling between the electric equations describing power electronic circuits and the equations of the electromagnetic field model increases the computational costs of the overall circuit-device simulation. This increase becomes more significant in the cases where power electronic circuits contain components having nonlinear characteristics such as diodes, transistors, etc.

In this chapter, we extend our proposed method to generate reduced order models of moving nonlinear electromagnetic devices including their driving power electronic circuits. The accuracy of the generated reduced order *device-circuit* models is demonstrated using an example of a rotating electrical machine coupled to a power electronics circuit.

7.2 The Coupled Electric Machine-Rectifier System

In this section, we address the modeling of an electromagnetic device including its driving power electronic circuit. For this purpose, we consider the example of an automotive alternator, which consists of a rotating electrical machine coupled to a power electronics rectifier. Alternators exist almost in all conventional vehicles, they are mainly used to charge the vehicle's battery. An alternator can be divided in two main subsystems: the electrical machine, and the power electronics rectifier circuit. The rotor of the electrical machine is mechanically coupled to the rotating shaft of the main combustion engine. Therefore, the rotation engine shaft causes the rotation of the rotor of the electrical machine. The power electronics rectifier circuit converts the three phases alternating current at the terminals of the machine to a direct current. The latter current is used to charge the car battery as it is shown in Fig. 7.1.

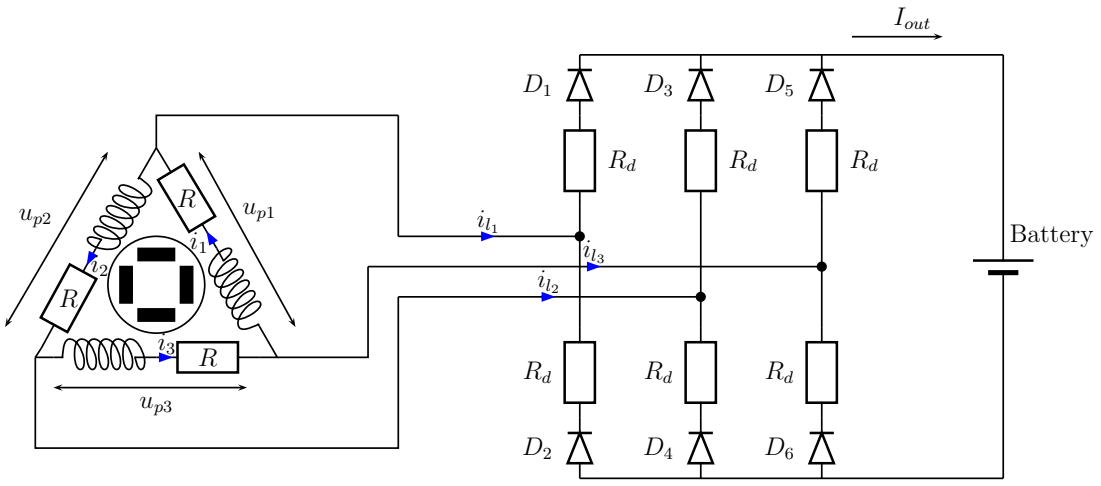

Figure 7.1: An electric diagram showing a three phases electric machine coupled to a three phases rectifier circuit.

7.3 The Rectifier Circuit Model

The rectifier circuit can be modeled using different approaches having different accuracy-complexity levels. However, the detailed modeling of the rectifier is out of the scope of this work, since the presented method can be applied any rectifier model. A simple approach for modeling the electric behavior of the rectifier is to switch between several simple analytical models that are derived at the different operation states of the rectifier. Each operation state is identified by a unique combination of diodes that are in conduction state.
In most of automotive alternators, the six distinguished operational states shown in the Table 7.1 can be identified:

Rectifier Operation State	Conducting diodes	Condition
1	D_1, D_3, D_6	$i_{l_1} > 0$, $i_{l_2} > 0$, $i_{l_3} < 0$
2	D_1, D_4, D_6	$i_{l_1} > 0$, $i_{l_2} < 0$, $i_{l_3} < 0$
3	D_1, D_4, D_5	$i_{l_1} > 0$, $i_{l_2} < 0$, $i_{l_3} > 0$
4	D_2, D_4, D_5	$i_{l_1} < 0$, $i_{l_2} < 0$, $i_{l_3} > 0$
5	D_2, D_3, D_5	$i_{l_1} < 0$, $i_{l_2} > 0$, $i_{l_3} > 0$
6	D_2, D_3, D_6	$i_{l_1} < 0$, $i_{l_2} > 0$, $i_{l_3} < 0$

Table 7.1: A table illustrating the six distinguished operation states of a three phase full bridge rectifier connected to an automotive alternator

where the currents i_{l_1}, i_{l_2}, i_{l_3} are called the line currents and are calculated directly from the currents i_1, i_2, i_3 that are flowing the in the stator coils of the E-machine by $i_{l_1} = i_1 - i_2$, $i_{l_1} = i_2 - i_3$, $i_{l_1} = i_3 - i_1$ as it is shown in the circuit in Fig. 7.1.
In each of the six operation states in the Table 7.1, the rectifier can be modeled by applying Kirchhoff's second law (*loops rule*) to the electric machine-rectifier circuit in Fig. 7.1. This results in the following equation systems in each of the six operation state:

Rectifier model at the operation state 1:

$$\begin{bmatrix} u_{1p} \\ u_{2p} \\ u_{3p} \end{bmatrix} = \begin{bmatrix} -2R_d & R_d & R_d \\ R_d & -2R_d & R_d \\ R_d & R_d & -2R_d \end{bmatrix} \begin{bmatrix} i_1 \\ i_2 \\ i_3 \end{bmatrix} + \begin{bmatrix} -u_d(i_1 - i_2) - u_d(i_3 - i_1) \\ +u_d(i_1 - i_2) - u_d(i_2 - i_3) \\ +u_d(i_2 - i_3) + u_d(i_3 - i_1) \end{bmatrix} \begin{bmatrix} -u_b \\ 0 \\ +u_b \end{bmatrix} \tag{7.1}$$

Rectifier model at the operation state 2:

$$\begin{bmatrix} u_{1p} \\ u_{2p} \\ u_{3p} \end{bmatrix} = \begin{bmatrix} -2R_d & R_d & R_d \\ R_d & -2R_d & R_d \\ R_d & R_d & -2R_d \end{bmatrix} \begin{bmatrix} i_1 \\ i_2 \\ i_3 \end{bmatrix} + \begin{bmatrix} -u_d(i_1 - i_2) - u_d(i_3 - i_1) \\ +u_d(i_1 - i_2) + u_d(i_2 - i_3) \\ -u_d(i_2 - i_3) + u_d(i_3 - i_1) \end{bmatrix} \begin{bmatrix} -u_b \\ +u_b \\ 0 \end{bmatrix} \tag{7.2}$$

Rectifier model at the operation state 3:

$$\begin{bmatrix} u_{1p} \\ u_{2p} \\ u_{3p} \end{bmatrix} = \begin{bmatrix} -2R_d & R_d & R_d \\ R_d & -2R_d & R_d \\ R_d & R_d & -2R_d \end{bmatrix} \begin{bmatrix} i_1 \\ i_2 \\ i_3 \end{bmatrix} + \begin{bmatrix} -u_d(i_1 - i_2) + u_d(i_3 - i_1) \\ +u_d(i_1 - i_2) + u_d(i_2 - i_3) \\ -u_d(i_2 - i_3) - u_d(i_3 - i_1) \end{bmatrix} \begin{bmatrix} 0 \\ +u_b \\ -u_b \end{bmatrix} \tag{7.3}$$

Rectifier model at the operation state 4:

$$\begin{bmatrix} u_{1p} \\ u_{2p} \\ u_{3p} \end{bmatrix} = \begin{bmatrix} -2R_d & R_d & R_d \\ R_d & -2R_d & R_d \\ R_d & R_d & -2R_d \end{bmatrix} \begin{bmatrix} i_1 \\ i_2 \\ i_3 \end{bmatrix} + \begin{bmatrix} +u_d(i_1 - i_2) + u_d(i_3 - i_1) \\ -u_d(i_1 - i_2) + u_d(i_2 - i_3) \\ -u_d(i_2 - i_3) - u_d(i_3 - i_1) \end{bmatrix} \begin{bmatrix} +u_b \\ 0 \\ -u_b \end{bmatrix} \tag{7.4}$$

Rectifier model at the operation state 5:

$$\begin{bmatrix} u_{1p} \\ u_{2p} \\ u_{3p} \end{bmatrix} = \begin{bmatrix} -2R_d & R_d & R_d \\ R_d & -2R_d & R_d \\ R_d & R_d & -2R_d \end{bmatrix} \begin{bmatrix} i_1 \\ i_2 \\ i_3 \end{bmatrix} + \begin{bmatrix} +u_d(i_1 - i_2) + u_d(i_3 - i_1) \\ -u_d(i_1 - i_2) - u_d(i_2 - i_3) \\ +u_d(i_2 - i_3) - u_d(i_3 - i_1) \end{bmatrix} \begin{bmatrix} +u_b \\ -u_b \\ 0 \end{bmatrix} \tag{7.5}$$

Rectifier model at the operation state 6:

$$\begin{bmatrix} u_{1p} \\ u_{2p} \\ u_{3p} \end{bmatrix} = \begin{bmatrix} -2R_d & R_d & R_d \\ R_d & -2R_d & R_d \\ R_d & R_d & -2R_d \end{bmatrix} \begin{bmatrix} i_1 \\ i_2 \\ i_3 \end{bmatrix} + \begin{bmatrix} +u_d(i_1 - i_2) - u_d(i_3 - i_1) \\ -u_d(i_1 - i_2) - u_d(i_2 - i_3) \\ +u_d(i_2 - i_3) + u_d(i_3 - i_1) \end{bmatrix} \begin{bmatrix} 0 \\ -u_b \\ +u_b \end{bmatrix} \tag{7.6}$$

where u_b is the voltage of the car battery. The voltage drop across a conducting diode is divided into a linear part represented by the resistance R_d and a nonlinear part represented by the nonlinear relation (7.7) which is graphically illustrated in the Fig. 7.2:

$$u_d(i_d) = nu_t \log\left(\frac{i_d}{i_s} + 1\right) \tag{7.7}$$

The parameters n, u_t, i_s are the characteristic parameter of a diode, with n being the emission coefficient, u_t the thermal voltage, and i_s the reverse bias saturation current of the considered diode.

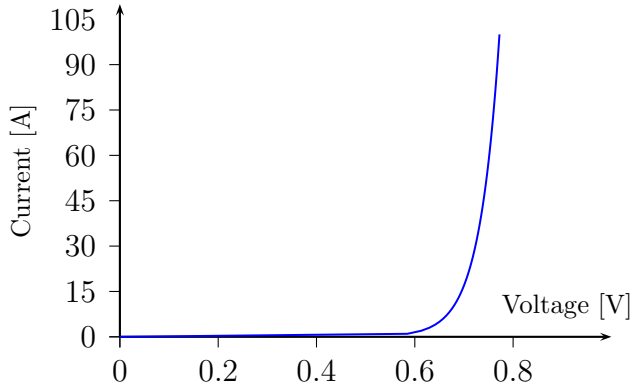

Figure 7.2: A typical nonlinear characteristic curve of a diode.

After deriving the rectifier models in its six operational states, the rectifier can be molded in its overall operation range by switching among the six models (7.1)-(7.6) during the simulation run. The switching criteria are the values of the line currents i_{l_1}, i_{l_2}, i_{l_3} as it

is shown in the Table 7.1.
It is clear in Fig. 7.1 that the voltages u_{p_1}, u_{p_2}, u_{p_3} at the terminals of the stator coils do not depend only on the state of the rectifier, but they depend as well on the state of electromagnetic field in the E-machine. Therefore, the voltages u_{p_1}, u_{p_2}, u_{p_3} couple the electromagnetic field model of the E-machine to the electric model of the three phase rectifier.

7.4 Electromagnetic Field Model in the E-Machine

Several types of electrical machines can be used in automotive alternators, such as the electrically excited machines, or the permanent magnets excited machines, etc. In this example, the permanent magnets excited synchronous machine (PSM) is chosen. However, the approach presented in here can be applied straight forward to other types of electrical machine .
The geometry of the chosen machine is shown in Fig. 7.3.(a). The rotor of the machine contains 12 engraved permanent magnets that serves as a source of electromagnetic field excitation. The rotor is mechanically coupled to the shaft of the combustion engine, therefore, its rotates during the vehicle run and produces a time varying electromagnetic field. The latter field induces an electric voltage in the three coils in the stator. The value of the induced voltages and currents in the stator coils depends on the state of magnetic field in the machine and on the state of the rectifier as has been discussed in the previous chapter.
The behavior of electromagnetic field in the PSM machine is modeled using the BEM-FEM method. This produced a nonlinear system of differential algebraic equations (2.13). By eliminating the algebraic equations form the model (2.13) according to (2.30), the machine model has become a large scale system of nonlinear differential equations of the form (7.8):

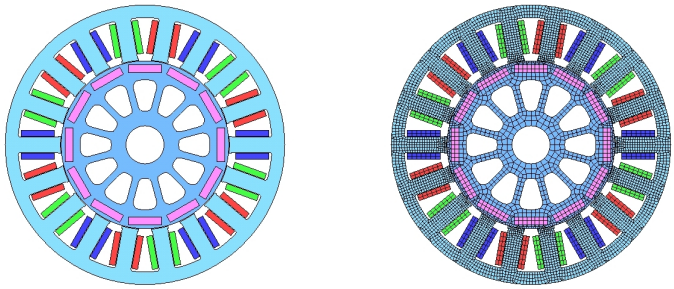

(a) (b)

Figure 7.3: A 2D model of a permanent magnets excited synchronous machine.

$$\mathbf{C}\dot{\mathbf{a}} + \Big[\mathbf{K}(\mathbf{a}) + \mathbf{K}^{\mathrm{BEM}}(\phi)\Big]\mathbf{a} = \mathbf{b}_1 i_1 + \mathbf{b}_2 i_2 + \mathbf{b}_3 i_3 + \mathbf{p}_{pm} \tag{7.8}$$

where $\phi \in [0 - 360]$ is the angular position of the rotor. The vectors $\mathbf{b}_1, \mathbf{b}_3, \mathbf{b}_3$ describe respectively the distribution of current density in the three stator coils. The term $\mathbf{p}_{pm}$ is a constant vector describing the contribution of the permanent magnets to the electromagnetic field excitation.

The induced voltages at the terminals of the stator coils u_{p_1}, u_{p_2} , u_{p_3} can be calculated according to (2.24) as:

$$\begin{cases} u_{p_1} = Ri_1 + \mathbf{b}_1^T \dot{\mathbf{a}} \\ u_{p_2} = Ri_2 + \mathbf{b}_2^T \dot{\mathbf{a}} \\ u_{p_3} = Ri_3 + \mathbf{b}_3^T \dot{\mathbf{a}} \end{cases} \tag{7.9}$$

where R is the Ohmic resistance of a stator coil.

Finally the induced electromagnetic torque on the surface of the rotor τ_{mag} can be calculated by:

$$\tau_{\mathrm{mag}} = \mathbf{a}^{\mathbf{T}}\mathbf{S}(\phi)\mathbf{a} \tag{7.10}$$

7.5 Solving the Coupled Electromagnetic Field- Electric Circuit Model

In the electromagnetic field model (7.8), the unknown variables are the state variables of electromagnetic field $\mathbf{a} \in \mathbb{R}^n$ and the values of the three excitation current signals i_1, i_2, i_3 that are flowing in the stator coils. The values of currents i_1, i_2, i_3 can be only determined when solving the equations of the electromagnetic field model (7.8) simultaneously with the corresponding equations of the rectifier model (7.1)-(7.6) in each simulation time step. However, both of the aforementioned equation systems are nonlinear with respect to their unknown variables, therefore, their simultaneous solution imposes using iterative solving strategies. Such strategies update the values of the state-vector of electromagnetic field $\mathbf{a} \in \mathbb{R}^n$ and the values of the currents i_1, i_2, i_3 iteratively, until the values of the voltages u_{p_1}, u_{p_2}, u_{p_3} that results from the rectifier equation (7.1)-(7.6) and the EM filed equations (7.9) become equal in each simulation time step.
The aforementioned iterative strategies imposes solving the equations of the high order EM field model (7.8) for each updated values of the currents i_1, i_2, i_3, which increases the computational cost of simulating the machine-rectifier system significantly in comparison to simulating the machine alone.

7.6 Generating a Reduced Order Model for the Coupled E-machine-Rectifier System

The high computational cost of solving the equations of the EM field model (7.8) simultaneously with the rectifier equations (7.1)-(7.6) can be remarkably reduced. This can be done by approximating the high order nonlinear electromagnetic field model (7.8) by a fast reduced order model, while guaranteeing that the reduced order model is still able to approximate the high order model (7.8) accurately in the relevant regions of the state-space.
The reduced order model of the electromagnetic field in the E-machine can be generated using the scheme presented in the chapter 5. The resulting model of order $q \ll n$ is

given by:

$$\mathbf{C}_r\dot{\mathbf{a}}_r + \sum_{i=1}^{s_1}\alpha_i(\mathbf{a}_r)[\mathbf{g}_{ri} + \mathbf{L}_{ri}\mathbf{a}_r] + \sum_{j=1}^{s_2}\beta_j(\phi)\mathbf{K}_{rj}^{\text{BEM}}\,\mathbf{a}_r = \mathbf{b}_{r1}i_1 + \mathbf{b}_{r2}i_2 + \mathbf{b}_{r3}i_3 + \mathbf{p}_{r_{pm}} \tag{7.11}$$

$$\begin{cases} u_{p_1} = Ri_1 + \mathbf{b}_{r1}^T\dot{\mathbf{a}}_r \\ u_{p_2} = Ri_2 + \mathbf{b}_{r2}^T\dot{\mathbf{a}}_r \\ u_{p_3} = Ri_3 + \mathbf{b}_{r3}^T\dot{\mathbf{a}}_r \end{cases} \tag{7.12}$$

$$\tau_{\text{mag}} = \mathbf{a}_r^T\left[\sum_{j=1}^{s_2}\beta_j(\phi)\mathbf{S}_{rj}\right]\mathbf{a}_r \tag{7.13}$$

such that the weighting coefficients are calculated from the following weighting functions:

$$(\alpha_1,\ldots,\alpha_{s_1}) = \boldsymbol{\alpha}\big(\mathbf{a}_r, \{\mathbf{a}_{r1},\ldots\mathbf{a}_{rs_1}\}\big) \tag{7.14}$$

$$(\beta_1,\ldots,\beta_{s_2}) = \boldsymbol{\beta}\big(\phi, \{\phi_1,\ldots\phi_{s_2}\}\big) \tag{7.15}$$

$$\sum_{i=1}^{s_1}\alpha_i = 1 \qquad \sum_{j=1}^{s_2}\beta_j = 1$$

where $\mathbf{a} = \mathbf{V}\mathbf{a}_r$, $\mathbf{a}\in\mathbb{R}^n$, $\mathbf{a}_r\in\mathbb{R}^q$, and $q \ll n$.

The matrices and vectors of the reduced order model are given by:

$\mathbf{C}_r = \mathbf{V}^\mathbf{T}\mathbf{C}\mathbf{V}$, $\mathbf{L}_{ri} = \mathbf{V}^\mathbf{T}\mathbf{L}_i\mathbf{V}$, $\mathbf{K}_{rj}^{\text{BEM}} = \mathbf{V}^\mathbf{T}\mathbf{K}_j^{\text{BEM}}\mathbf{V}$, $\mathbf{g}_{ri} = \mathbf{V}^\mathbf{T}\mathbf{g}_i$, $\mathbf{b}_{r1} = \mathbf{V}^\mathbf{T}\mathbf{b}_1$, $\mathbf{b}_{r2} = \mathbf{V}^\mathbf{T}\mathbf{b}_2$, $\mathbf{b}_{r3} = \mathbf{V}^\mathbf{T}\mathbf{b}_3$, $\mathbf{R}_{rj} = \mathbf{V}^\mathbf{T}\mathbf{R}_j\mathbf{V}$.

The generated reduced order model (7.11) is able to approximate the original model along and in the neighboring regions of the training trajectories. Therefore, the latter trajectories should be generated using coupled machine-rectifier simulation runs.

The projection matrix $\mathbf{V}\in\mathbb{R}^{n\times q}$ is generated using the proper orthogonal decomposition POD. The snapshots matrix of the POD approach is generated by assembling all the state-vectors of the high order nonlinear model (7.8) that have resulted from the coupled machine-rectifier simulation.

The reduced order model (7.11),(7.12) enables solving the EM field equations coupled to the rectifier equations (7.1)-(7.1) within a significantly shorter time than the case of using the original high order model.

7.7 Numerical Example

This example addresses the issue of generating a fast and accurate reduced order model of an automotive alternator, with a special focus on considering the strong coupling between the E-machine model and the rectifier circuit model.
In the first step, the electrical machine shown in Fig. 7.3 is modeled using the BEM-FEM method. This produced a nonlinear system of differential algebraic equations (2.13) of order $n = 22548$. By eliminating the algebraic equations form the model (2.13) according to (2.30), the machine model becomes a large scale system of nonlinear differential equations of order $n = 19716$ of the form (7.8).
The high order EM field model (7.8) coupled to the rectifier model (7.1)-(7.6) is used for generating three distinguished *training trajectories*. Those trajectories were generated at three distinguished angular velocities w of the rotor, namely $w = 1200$ revolutions per minute (rpm) , $w = 1800$ rpm, $w = 3000$ rpm respectively. The angular velocity of the rotor is assumed, without the loss of generality, to be constant during each simulation run. Under this assumption, the angular position of the rotor is given by:

$$\phi = \left(\frac{360}{60}\right) wt + \phi_0 \tag{7.16}$$

where ϕ_0 is the initial position of the rotor at the beginning of the simulation, its value is set in this example to zero $\phi_0 = 0$.
The simulation time step is chosen in all the performed simulation runs to be equal to $\Delta t = 0.5/w$, in such a way that rotor rotates 0.5 degrees in each simulation step.
The position dependant matrices $\mathbf{K}^{\mathrm{BEM}}(\phi)$, $\mathbf{S}(\phi)$ are extracted at $s_2 = 720$ angular positions that are uniformly distributed in the range $\phi \in [0, 360[$.
Our proposed selection algorithm 1 has been applied for the selection of linearization points along the training trajectories. The algorithm 1 has selected a number of 180 linearization points in the range $\phi \in [0, 90[$ along each training trajectory. The latter

selection was unchanged even upon varying the value of the selection parameter τ_1 in the rage $[0.1, 1]$. This can be traced back to the symmetry in the geometry of the electrical machine. This symmetry causes the repetition of same electromagnetic field distribution after a period of 90 degrees if the angular velocity remains constant. This shows that the algorithm 1 selects only distinguished linearized models.
The nonlinear term $\mathbf{K}(\mathbf{a})\mathbf{a}$ in (7.8) is linearized at the $s_1 = 3 \times 180 = 540$ selected linearization points along the three training trajectories.
All the simulated state-vectors of the high order electromagnetic field model (7.8) on the training trajectories are assembled in the snapshots matrix. Then, the proper orthogonal decomposition POD approach is applied to find a projection matrix $\mathbf{V} \in \mathbb{R}^{19716\times 70}$ which provides the best low rank approximation of all the state-vectors that are contained in the snapshots matrix. The magnetic vector potential field that corresponds to the first ten vectors in the projection matrix $V \in \mathbb{R}^{19716\times 70}$ are shown in Fig. 7.4.

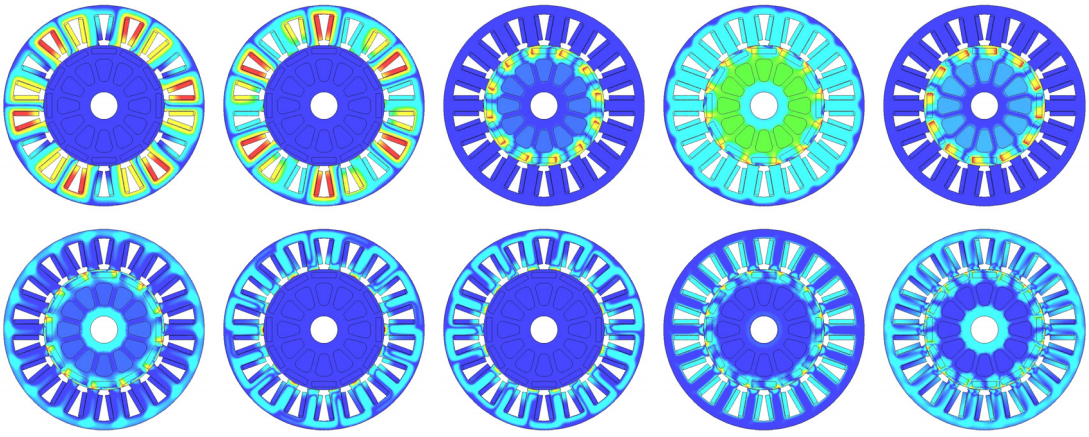

Figure 7.4: The ten figures illustrate respectively the magnetic vector potential field that correspond to the first ten vectors in the projection matrix $\mathbf{V}$.

A reduced order model of the electric machine (7.11), (7.12), (7.13) of order $q = 70$ is generated. The reduction is carried out by projecting all the extracted matrices and vectors onto the subspace spanned by the columns of the matrix $\mathbf{V}$, as has been shown in the previous paragraphs.

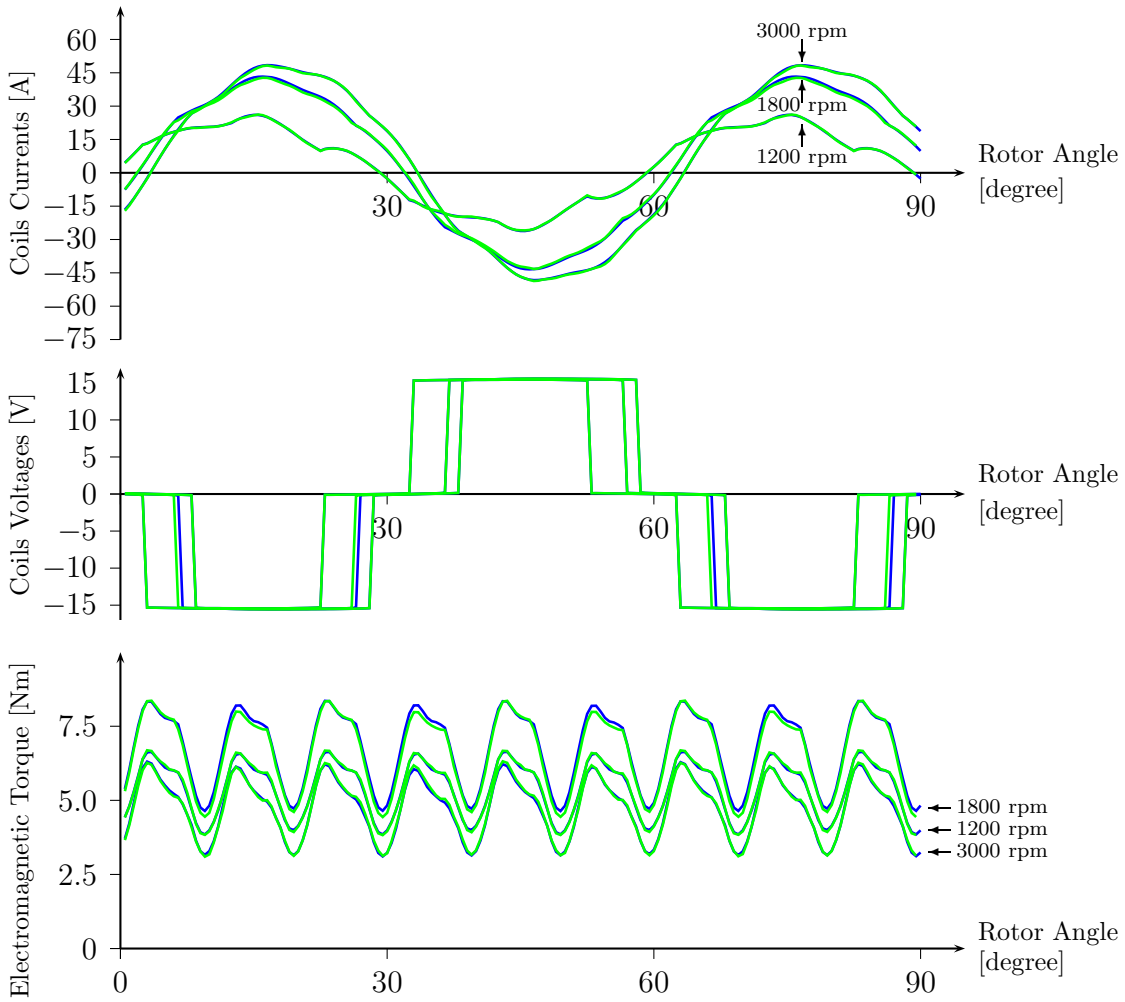

Figure 7.5: Simulating an automotive alternator using a high order nonlinear machine model $n = 19716$ coupled to the rectifier circuit model (blue lines) vs. using a reduced order machine model $n = 70$ coupled to the rectifier circuit model (green lines).

The simulation results in Fig. 7.5 shows that the reduced order model (7.11)-(7.13) of order $n = 70$ coupled to the rectifier model (7.1)-(7.6) produces an excellent approximation of the results of the original nonlinear model (7.8)-(7.10) of order $n = 19716$ coupled to the same rectifier model (7.1)-(7.6).

The same comparison is carried out at two further angular velocities $w = 10000$ rpm, 2500 rpm whose trajectories were not included in the training trajectories of the reduced order EM field model (7.11). The simulation results shown in Fig. 7.6 show a very good

matching between the results achieved using the full order model (7.8) and the ones achieved using the reduced order model (7.11) for the angular velocity $w = 2500$ rpm.

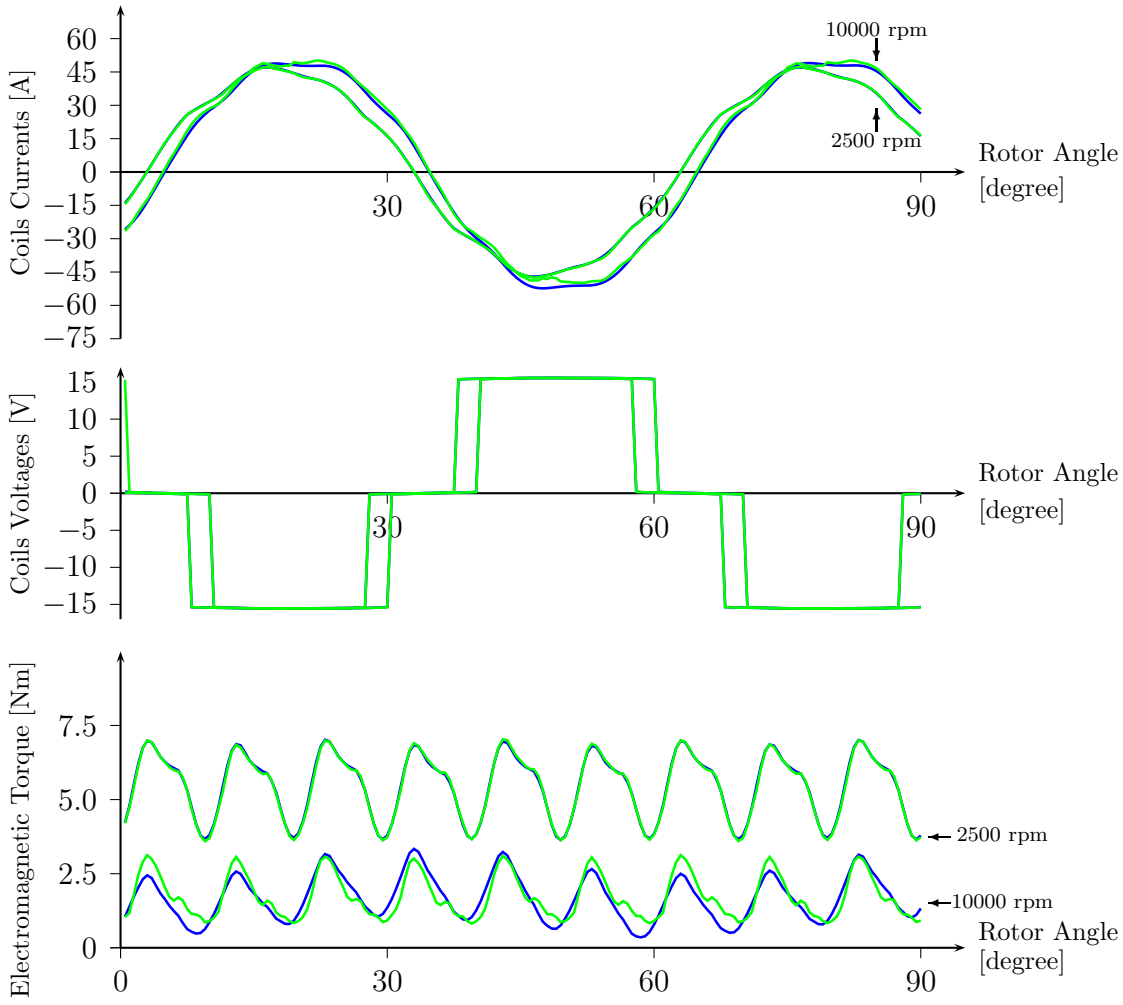

Figure 7.6: Simulating an automotive alternator using a high order nonlinear machine model $n = 19716$ coupled to the rectifier circuit model (blue lines) vs. using a reduced order machine model $n = 70$ coupled to the rectifier circuit model (green lines).

A larger approximation error can be noticed for the simulation at $w = 10000$ rpm. This is due to the fact that the nonlinear behavior of electromagnetic field in the electrical machine at this angular velocity is unknown to the reduced order model (7.11). However, this approximation error can be easily alleviated by linearizing the nonlinear term $\mathbf{K}(\mathbf{a})\mathbf{a}$

at new linearization points along the simulation trajectory $w = 10000$ rpm, and adding the new linearized models after reducing their order to the reduced order EM field model (7.11).

The CPU time required for solving the electromagnetic field equation coupled to the rectifier equations using both the full order EM field model and the reduced order one are illustrated in Table 7.2. The results show that the reduced order E-machine-rectifier model is almost 1000 times faster than the full order coupled model.

Angular Velocity (rpm)	Simulation Time (sec)	
	Full Order EM Field Model Coupled to the Rectifier Model $n = 19716$	Reduced Order EM Field Model Coupled to the Rectifier Model $n = 70$
1200	4140	4.75
1800	4015	4.43
3000	4072	4.48
10000	4201	4.67
2500	4101	4.53

Table 7.2: Simulation time: full order nonlinear EM field model coupled to the rectifier model versus the reduced order EM field model coupled to the rectifier model

The simulation results presented in this chapter show that the proposed reduced order model of electromagnetic field can be efficiently applied in the reduced order modeling of electromagnetic devices including their power electronics driving circuits.

Chapter 8

CONCLUSIONS AND FUTURE WORK

In this work, a new method for generating reduced order models of electromagnetic devices that contain moving components and materials with nonlinear magnetic properties is presented. The new method enables applying model order reduction techniques to generate fast and accurate reduced order models of a large class of electromagnetic devices. Such devices include among others rotating electrical machines, electromagnetic valves, and electromechanical relays.

The nonlinearity in the high order electromagnetic field model that is caused by the nonlinear properties of magnetic materials is approximated using the trajectory piecewise linear TPWL approach. The movement of the device components is modeled using a novel approach that couples the reduced order electromagnetic field model to the mechanical equations, in such a way that the reduced order EM field model is adapted in each simulation time step according to the new components positions. The order reduction is carried out by approximating the original electromagnetic field distributions by a linear combination of few virtual EM field distributions, which are found using the proper orthogonal decomposition POD.

Then, the challenge of determining the number and the positions of the linearization points in the TPWL model is tackled. This is done by introducing a new selection algorithm that observes the changes in the device materials properties during the simulation, and accepts a new linearization point only if the magnetic properties of materials at this point is distinguished from all the other linearization points.

The presented method is extended to generate parametric reduced order models of moving nonlinear EM devices. Moreover, several algorithms for generating the reduction

subspace for the parametric models are introduced and compared. The issue of selecting the positions of the training points of the parametric reduced order model in the design parameters space is addressed, and a novel scheme based on a multiobjective optimization strategy is proposed.

Finally, an approach for generating reduced order models of electromagnetic devices including their power electronics driving circuits is presented. The performance of this approach is demonstrated on the example of a rotating electrical machine coupled to a rectifier circuit.

In the future research, it would be of high interest to develop computationally efficient methods for reducing the order of large scale systems of differential algebraic equations, since eliminating the algebraic variables from the system model, which is the approach followed in this work, can be very computationally expensive if the number of the algebraic equations is large.

Moreover, the choice of weighting functions in the TPWL models and in the parametric reduced order models would be a very interesting research field. Since developing optimal weighting functions could enable reducing the number of required linearization points in the TPWL models, or reducing the number of required training points in the design parameters space for the parametric reduced order models.

Apart from that, it would be interesting to extend the application of the proposed algorithm for selecting the linearization points in the TPWL model from electromagnetic modeling domain to other physical modeling domains, such as thermodynamics and fluid dynamics. In this case, the change in the relevant material properties, such as the thermal conductivity in thermodynamics or viscosity in fluid dynamics, can be observed and exploited as a base for selecting the linearization points.

BIBLIOGRAPHY

[1] M. N. Albunni, R. Eid, and B. Lohmann. Model order reduction of linear electromagnetic devices with a mixed voltage-current excitation. *Proc. of the 6th Vienna International Conference on Mathematical Modelling MATHMOD*, February 2009.

[2] M. N. Albunni, V. Rischmuller, T. Fritzsche, and B. Lohmann. Model order reduction of moving nonlinear electromagnetic devices. *IEEE Transactions on Magnetics*, 44(7):1822–1829, July 2008.

[3] M. N. Albunni, V. Rischmuller, T. Fritzsche, and B. Lohmann. Multiobjective optimization of the design of nonlinear electromagnetic systems using parametric reduced order models. *IEEE Transactions on Magnetics*, 45(3):1474–1477, March 2009.

[4] V. Algazi and D. Sakrison. On the optimality of the karhunen-love expansion (corresp.). *IEEE Transactions on Information Theory*, 15(2):319–321, March 1969.

[5] Juan J. Alonso and Patrick A. LeGresley. Investigation of non-linear projection for POD based reduced order models for aerodynamics. *American Institute of Aeronautics and Astronautics*, 2001.

[6] Athanasios C. Antoulas. *Approximation of Large scale Dynamical Systems*. Society for Industrial and Applied Mathematics, 2006.

[7] P. Astrid. *Reduction of Process Simulation Models: a proper orthogonal decomposition approach*. PhD thesis, Technische Universiteit Eindhoven, 2004.

[8] P. Astrid and S. Weiland. On the construction of POD models from partial observations. In *Proceedings of the 44th IEEE Conference on Decision and Control, and the European Control Conference*, December 2005.

[9] Z. Bai and D. Skoogh. A projection method for model reduction of bilinear dynamical systems. *Linear Algebra and its Applications, Special Issue on Order Reduction of Large-Scale Systems*, 415(2-3):406–425, June 2006.

[10] P. Benner and V. Sokolov. Partial realization of descriptor systems. *System & Control Letters*, 55(11):929–938, November 2006.

[11] G. Berkooz, P. Holmes, and J. L. Lumley. The proper orthogonal decomposition in the analysis of turbulent flows. *Annual Review of Fluid Mechanics*, 25:539–575, January 1993.

[12] A. Bossavit. *Computational Electromagnetism*. Academic Press Inc., 1998.

[13] Benali Boualem and Francis Piriou. Numerical models for rotor cage induction machines using finite element method. *IEEE Transactions on Magnetics*, 34(5):3202–3205, Sep 1998.

[14] A. C. Cangellaris, M. Celik, S. Pasha, and L. Zhao. Electromagnetic model order reduction for system level modeling. *IEEE Transactions on Microwave Theory and Techniques*, 47(6):840–850, June 1999.

[15] M. Clemens, M. Wilke, R. Schuhmann, and T. Weiland. Subspace projection extrapolation scheme for transient field simulations. *IEEE Transactions on Magnetics*, 40:934–937, March 2004.

[16] M. Costabel and M. Dauge. Singularities of electromagnetic fields in polyhedral domains. *Archive for Rational Mechanics and Analysis*, 151(3):221–276, 2000.

[17] K. Deb. *Multi-Objective Optimization using Evolutionary Algorithms*. Wiley-Interscience Series in Systems and Optimization. John Wiley & Sons, Chichester, 2001.

[18] K. Deb, M. Mohan, and S. Mishra. A fast multi-objective evolutionary algorithm for finding well-spread Pareto-optimal solutions. *Technical Report 2003002*, 2003.

[19] N. Dong and J. Roychowdhury. General-purpose nonlinear model-order reduction using piecewise-polynomial representations. *IEEE Transactions on Computer-Aided Design of Integrated Circuits and Systems*, 27(3):249–264, February 2008.

[20] Robert S. Elliott. *Electromagnetics: History, Theory and Applications*. IEEE/OUP Series on Electromagnetic Wave Theory. Wiley-IEEE Press, 1999.

[21] B. I. Epureanu, K. C. Hall, and E. H. Dowell. Reduced-order models of unsteady viscous flows in turbomachinery using viscous-inviscid coupling. *Journal of Fluids and Structures*, 15(2):255–273, 2001.

[22] O. Farle, V. Hill, P. Ingelstroem, and R. Dyczij-Edlinger. Ordnungsreduktion linearer zeitinvarianter finite- elemente-modelle mit multivariater polynomieller parametrisierung (model order reduction of linear finite element models parameterized by polynomials in several variables). *at - Automatisierungstechnik*, 54:161–169, 2006.

[23] R. W. Freund. Model reduction methods based on Krylov subspaces. *Acta Numerica*, 12:267–319, 2003.

[24] F.R. Gantmacher. *Theory of Matrices*. Chelsea, New York, 1959.

[25] C. W. Gear. *Numerical Initial Value Problems in Ordinary Differential Equations*. Series in Automatic Computation. Prentice-Hall, Englewood Cliffs, New Jersey, 1971.

[26] K. Glover. All optimal hankel-norm approximations of linear multivariable systems and their L_∞ error. *International Journal of Control*, 39(6):1115–1193, June 1984.

[27] D. Gratton and K. E. Wilcox. Reduced-order, trajectory piecewise-linear models for nonlinear computational fluid dynamics. Master's thesis, Massachusetts Institute of Technology. Dept. of Aeronautics and Astronautics, 2004.

[28] E. J. Grimme. *Krylov Projection Methods for Model Reduction*. PhD thesis, University of Illinois, Urbana-Champaign, 1997.

[29] S. Gugercin, D. C. Sorensen, and A. C. Antoulas. A modified low-rank smith method for large-scale Lyapunov equations. *Numerical Algorithms*, 32(1):27–55, 2003.

[30] F. Henrotte, A. Nicolet, H. Hdia, A. Genon, and W. Legros. Modeling of electromechanical relays taking into account movement and electric circuits. *IEEE Transactions on Magnetics*, 30(5):3236–3239, Sep 1994.

[31] E. S. Hung and S. D. Senturia. Generating efficient dynamical models for microelectromechanical systems from a few finite-element simulation runs. *IEEE Journal of Microelectromechanical Systems*, 8(3):280–289, September 1999.

[32] M. E. Kowalski and J.-M. Jin. Karhunen-loeve based model order reduction of nonlinear systems. In *IEEE Antennas and Propagation Society International Symposium*, volume 1, pages 552–555, 2002.

[33] S. Kurz. *Die numerische Behandlung elektromagnetischer Systeme mit Hilfe der Kopplung der Methode der finite Elemente und der Rand Elemente.* PhD thesis, Universität Stuttgart, 1998.

[34] S. Kurz, U. Becker, and H. Maisch. Dynamic simulation of electromechanical systems: from maxwell's theory to common-rail diesel injection. *Naturwissenschaften*, 88(5):183–192, May 2001.

[35] S. Kurz, J. Fetzer, and G. Lehner. Three dimensional transient BEM-FEM coupled analysis of electrodynamic levitation problems. *IEEE Transactions on Magnetics*, 32(3), May 1996.

[36] V. Leconte, V. Mazauric, G. Meunier, and Y. Marchal. Remeshing procedures compared to FEM-BEM coupling to simulate the transients of electromechanical devices. In *in Proceedings of CEFC*, page 227, 2000.

[37] T. Leen, M. Rudnick, and D. Hammerstrom. Hebbian feature discovery improves classifier efficiency. In *IJCNN International Joint Conference on Neural Networks*, volume 1, pages 51–56, June 1990.

[38] D. Lefebvre and F. Rotella. A note on the determination of the Weierstrass form for generalized state-space systems. *Proceedings of the 34th IEEE Conference on Decision and Control*, 1995.

[39] J. R. Li. *Model Reduction of Large Linear Systems via Low Rank System Gramians*. PhD thesis, Massachusetts Institute of Technology, 2000.

[40] Y. C. Liang, H. P. Lee, S. P. Lim, W. Z. Lin, K. H. Lee, and C. G. Wu. Proper orthogonal decomposition and its applications, part I: Theory. *Journal of Sound and Vibration*, 252(3):527–544, May 2002.

[41] W.Q. Liu and V. Sreeram. Model reduction of singular systems. *Proceedings of the 39th IEEE Conference on Decision and Control*, December 2000.

[42] X. Ma and J.A. De Abreu-Garcia. On the computation of reduced order models of nonlinear systems using balancing technique. In *Proceedings of the 27th IEEE Conference on Decision and Control*, pages 1165–1166, December 1998.

[43] S. Mijalkovic. Truly nonlinear model-order reduction techniques. In *In proceedings of the IEEE 7th. Int. Conf. on Thermal, Mechanical and Multiphysics Simulation and Experiments in Micro-Electronics and Micro-Systems, EuroSimE*, pages 1–5, 2006.

[44] B. Moore. Principal component analysis in linear systems: Controllability, observability, and model reduction. *IEEE Transactions on Automatic Control*, 26(1):17–32, February 1981.

[45] C. T. Mullis and R. A. Roberts. Synthesis of minimum roundoff noise fixed point digital filters. *IEEE Transactions On Circuits and Systems*, 23(9):551562, September 1976.

[46] R. Niu and M. Skliar. Image-based identification of low-dimensional POD models of noninvasive thermal therapies. In *American Control Conference*, June 2006.

[47] T. Penzl. A cyclic low rank smith method for large sparse Lyapunov equations with applications in model reduction and optimal control. *SIAM J. Sci. Comput*, 21:1401–1418, 1998.

[48] J. Philips. A statistical perspective on nonlinear model reduction. In *Proceedings of the IEEE International Workshop on Behavioral Modeling and Simulation BMAS*, pages 41–46, 2003.

[49] J. Phillips. Projection-based approaches for model reduction of weakly nonlinear, time-varying systems. *IEEE Transactions on Computer-Aided Design of Integrated Circuits and Systems*, 22(2):171–187, February 2003.

[50] W. H. Press, B. P. Flannery, S. A. Teukolsky, and W. T. Vetterling. *Numerical Recipes in C: The Art of Scientific Computing*. Cambridge University Press, 2007.

[51] L. Qu and P. L. Chapman. Extraction of low-order non-linear inductor models from a high-order physics-based representation. *IEEE Transactions on Power Electronics*, 21(3):813–817, May 2006.

[52] O. Rain, B. Auchmann, S. Kurz, V. Rischmuller, and S. Rjasanow. Edge-based BE-FE coupling for electromagnetics. *IEEE Transactions on Magnetics*, 24(4):679–682, 2006.

[53] M. Rewienski. *A Trajectory Piecewise-Linear Approach to Model Order Reduction of Nonlinear Dynamical Systems*. PhD thesis, Massachusetts Institute of Technology, June 2003.

[54] M. Rewienski and J. White. A trajectory piecewise-linear approach to model order reduction and fast simulation of nonlinear circuits and micromachined devices. *IEEE Transactions on Computer-Aided Design of Integrated Circuits and Systems*, 22:155–170, Feb 2003.

[55] V. Rischmuller. *Eine Parallelisierung der Kopplung der Methode der finiten Elemente und der Randelementmethode*. PhD thesis, Universität Stuttgart, 2005.

[56] V. Rischmuller, J. Fetzer, M. Haas, S. Kurz, , and W.M. Rucker. Computational efficient BEM-FEM coupled analysis of 3d nonlinear eddy current problems using domain decomposition. *Proceedings of the 8th International IGTE Symposium on Numerical Field Calculation*, 1998.

[57] W. J. Rugh. *Nonlinear System Theory: The Volterra/Wiener Approach*. The Johns Hopkins University Press, Baltimore, 1981.

[58] B. Salimbahrami. *Structure Preserving Order Reduction of Large Scale Second Order Models*. Phd thesis, Institute of Automatic Control, Technische Universitaet Muenchen, 2006.

[59] J. M. A. Scherpen. Balancing for nonlinear systems. *Systems and Control Letters*, 21:143–153, 1993.

[60] M. Simeoni, G. A. E. Vandenbosch, and I. E. Lager. Model order reduction techniques for linear electromagnetic problems - an overview. *European Microwave Conference*, 2, 2005.

[61] L. Sirovich. Turbulence and the dynamics of coherent structures. *Quarterly of Applied Mathematics*, 45:561–571, October 1987.

[62] T. Stykel. On some norms for descriptor systems. *IEEE Transactions on Automatic Control*, 51(5):842–847, May 2006.

[63] S.K. Tiwary and R.A. Rutenbar. Scalable trajectory methods for on-demand analog macromodel extraction. *Proceeding of the 42nd Design Automation Conference DAC*, pages 403 – 408, June 2005.

[64] D. Vasilyev, M. Rewienski, and J. White. Perturbation analysis of TBR model reduction in application to trajectory-piecewise linear algorithm for MEMS structures. In *Proceedings of the NSTI Nanotechnology Conference and Trade Show*, volume 2, pages 434 – 437. Nano Science and Technology Institute, 2004.

[65] Christian Voigt and Jürgen Adamy. *Formelsammlung der Matrizenrechnung*. Oldenbourg Wissenschaftsverlag GmbH, 2007.

[66] M. Wax and T. Kailath. Detection of signals by information theoretic criteria. *IEEE Transactions on Acoustics, Speech and Signal Processing*, 33(2):387–392, April 1985.

[67] T. Wittig, I. Munteanu, R. Schuhmann, and T. Weiland. Two-step lanczos algorithm for model order reduction. *IEEE Trans. on Magnetics*, 38:673–676, March 2002.

[68] H. Wu and A. C. Cangellaris. Model-order reduction of finite-element approximations of passive electromagnetic devices including lumped electrical-circuit models. *IEEE Transactions on Microwave Theory and Techniques*, 52:2305–2313, Sep 2004.